

---

Theses and Dissertations

---

Spring 2017

# Electrical resistance based damage modeling of multifunctional carbon fiber reinforced polymer matrix composites

Robert James Hart  
*University of Iowa*

Copyright © 2017 Robert James Hart

This dissertation is available at Iowa Research Online: <http://ir.uiowa.edu/etd/5493>

---

## Recommended Citation

Hart, Robert James. "Electrical resistance based damage modeling of multifunctional carbon fiber reinforced polymer matrix composites." PhD (Doctor of Philosophy) thesis, University of Iowa, 2017.  
<http://ir.uiowa.edu/etd/5493>.

---

Follow this and additional works at: <http://ir.uiowa.edu/etd>



Part of the [Mechanical Engineering Commons](#)

ELECTRICAL RESISTANCE BASED DAMAGE MODELING OF  
MULTIFUNCTIONAL CARBON FIBER REINFORCED POLYMER MATRIX  
COMPOSITES

by

Robert James Hart

A thesis submitted in partial fulfillment  
of the requirements for the Doctor of Philosophy  
degree in Mechanical Engineering in the  
Graduate College of  
The University of Iowa

May 2017

Thesis Supervisor: Professor Olesya I. Zhupanska

Professor Jia Lu

Graduate College  
The University of Iowa  
Iowa City, Iowa

CERTIFICATE OF APPROVAL

---

PH.D. THESIS

---

This is to certify that the Ph.D. thesis of

Robert James Hart

has been approved by the Examining Committee for  
the thesis requirement for the Doctor of Philosophy degree  
in Mechanical Engineering at the May 2017 graduation.

Thesis Committee:

---

Olesya I. Zhupanska, Thesis Supervisor

---

Jia Lu, Thesis Supervisor

---

Shaoping Xiao

---

M. Asghar Bhatti

---

Hongtao Ding

To my family: Amy and Landon

## ACKNOWLEDGEMENTS

I would like to express my sincere appreciation to Professor Olesya I. Zhupanska for her encouragement and guidance throughout this research process and throughout my education at The University of Iowa. In addition I would like to thank my thesis committee members: Jia Lu, Shaoping Xiao, M. Asghar Bhatti, and Hongtao Ding for their thoughtful consideration and support. Finally, I would like to thank my family and friends for their support during my studies at The University of Iowa.

## ABSTRACT

In the current thesis, the 4-probe electrical resistance of carbon fiber-reinforced polymer (CFRP) composites is utilized as a metric for sensing low-velocity impact damage. A robust method has been developed for recovering the directionally dependent electrical resistivities using an experimental line-type 4-probe resistance method. Next, the concept of effective conducting thickness was uniquely applied in the development of a brand new point-type 4-probe method for applications with electrically anisotropic materials. An extensive experimental study was completed to characterize the 4-probe electrical resistance of CFRP specimens using both the traditional line-type and new point-type methods. Leveraging the concept of effective conducting thickness, a novel method was developed for building 4-probe electrical finite element (FE) models in COMSOL. The electrical models were validated against experimental resistance measurements and the FE models demonstrated predictive capabilities when applied to CFRP specimens with varying thickness and layup. These new models demonstrated a significant improvement in accuracy compared to previous literature and could provide a framework for future advancements in FE modeling of electrically anisotropic materials. FE models were then developed in ABAQUS for evaluating the influence of prescribed localized damage on the 4-probe resistance. Experimental data was compiled on the impact response of various CFRP laminates, and was used in the development of quasi-static FE models for predicting presence of impact-induced delamination.

The simulation-based delamination predictions were then integrated into the electrical FE models for the purpose of studying the influence of realistic damage patterns on

electrical resistance. When the size of the delamination damage was moderate compared to the electrode spacing, the electrical resistance increased by less than 1% due to the delamination damage. However, for a specimen with large delamination extending beyond the electrode locations, the oblique resistance increased by 30%. This result suggests that for damage sensing applications, the spacing of electrodes relative to the size of the delamination is important. Finally CT image data was used to model 3-D void distributions and the electrical response of such specimens were compared to models with no voids. As the void content increased, the electrical resistance increased non-linearly. The relationship between void content and electrical resistance was attributed to a combination of three factors: (i) size and shape, (ii) orientation, and (iii) distribution of voids. As a whole, the current thesis provides a comprehensive framework for developing predictive, resistance-based damage sensing models for CFRP laminates of various layup and thickness.

## PUBLIC ABSTRACT

In this thesis, the electrical properties of carbon fiber composites are used as a tool for detecting physical damage inside the material. The carbon fiber composites consisted of an epoxy plastic base with carbon fiber reinforcements. The electrical and mechanical properties of these two constituents are quite dissimilar, therefore when combining these constituents into one single composite material; it is often difficult to characterize the properties of this new material. In this work, a robust method has been developed for determining these complex electrical properties using an experimental line-type 4-probe resistance method. Next, the concept of effective conducting thickness was uniquely applied in the development of a brand new point-type 4-probe method, which until now had never been applied to carbon fiber composites. An extensive experimental study was completed to characterize the electrical resistance of these carbon fiber specimens using both the traditional line-type and new point-type methods.

Next, computer models were developed in order to simulate the experiments. These computer simulation models demonstrated predictive capabilities when applied to carbon fiber specimens with varying thickness and fiber orientations. These new models demonstrated a significant improvement in accuracy compared to previous literature and could provide a framework for future advancements in computational modeling of such materials. Additional computer models were created in order to predict damage in carbon fiber specimens subjected to mechanical impact. The impact damage models and electrical models were then combined together to create a model which can detect the presence of mechanical damage using electrical resistance measurements. The computer



simulation results showed that as the severity of the damage increased, the electrical resistance of the carbon fiber specimen increased as well. Moreover, as the size of the damage grew vary large, the resistance increased as a non-linear rate. As a whole, the current thesis provides a comprehensive framework for developing predictive, resistance-based damage sensing models for carbon fiber materials with various fiber orientations and thicknesses.

## TABLE OF CONTENTS

LIST OF TABLES .....	xi
LIST OF FIGURES .....	xiii
CHAPTER 1: INTRODUCTION.....	1
1.1 Background Information and Motivation.....	1
1.2 Thesis Objectives .....	2
CHAPTER 2: LITERATURE REVIEW.....	4
2.1 Low-Velocity Impact Characterization of Carbon Fiber-Reinforced Polymer Composites .....	4
2.2 Electrical Characterization of Carbon Fiber-Reinforced Polymer Composites .....	10
2.3 Resistance-Based Damage Sensing.....	17
2.4 Multiphysics Interactions in Composites .....	23
2.5 Computerized Tomography Imaging of Composites .....	26
2.6 Literature Review: Summary .....	29
CHAPTER 3: EXPERIMENTAL METHODS.....	30
3.1 Description of Specimens.....	31
3.2 Impact Characterization .....	34
3.3 Electrical Characterization .....	37
3.3.1 Line-Type 4-Probe Method: Experimental Methods .....	39
3.3.2 Recovery of Experimental Electrical Resistivity .....	43
3.3.3 Point-Type 4-Probe Method: Experimental Methods.....	45
3.3.4 2-Probe High Intensity Current Pulse: Experimental Methods.....	48
3.4 Coordinated Electrified-Impact Testing.....	50
3.5 Computerized Tomography Imaging .....	52
3.6 Experimental Methods: Summary.....	53
CHAPTER 4: EXPERIMENTAL AND ANALYTICAL CHARACTERIZATION OF ELECTRICAL & IMPACT RESPONSE .....	55
4.1 Mathematical Electrical Models.....	55
4.2 Development of Finite Element Electrical Models .....	60
4.2.1 Significance of Effective Thickness in FE Models.....	62
4.2.2 FE Models: Line-Type 4-Probe Method with Line of Electrodes Aligned with Fiber Direction .....	63
4.2.3 FE Models: Line-Type 4-Probe Method with Line of Electrodes Transverse to Fiber Direction.....	64
4.2.4 FE Models: Oblique Measurement Plane Using Line-Type 4- Probe Method .....	66
4.2.5 FE Models: Point-Type 4-Probe Method.....	70
4.2.6 FE Models: Summary of Methods .....	71
4.3 Line-Type 4-Probe Method: Results .....	72
4.4 Point-Type 4-Probe Modified JIS Method: Results .....	80
4.5 Comparison of Line-Type and Point-Type 4-Probe Methods.....	84
4.6 Optimization of Electrical Properties Based on Material Thickness .....	87

4.7 2-Probe High Intensity Current Pulse: Results.....	89
4.8 Impact Characterization and Coordinated Electrified-Impact Testing: Results .....	94
4.9 Electrical and Impact Response: Summary .....	102
CHAPTER 5: DAMAGE SENSING FEASIBILITY MODELS .....	104
5.1 Development of Damage Sensing Feasibility Models.....	104
5.1.1 FE Models: Prescribed Fiber Breakage and Matrix Cracks .....	104
5.1.2 FE Models: Prescribed Delamination.....	108
5.2 Influence of Prescribed Damage to Various CFRP Layups: FE Results.....	110
5.2.1 FE Results: Prescribed Fiber Breakage and Matrix Cracking.....	110
5.2.2 FE Results: Prescribed Delamination.....	118
5.3 Optimization of Electrical Properties Based on Material Thickness: FE Results.....	122
5.4 Damage Sensing Feasibility Study: Summary .....	125
CHAPTER 6: QUASI-STATIC MODELING OF LOW-VELOCITY IMPACT- INDUCED DELAMINATION .....	126
6.1 Development of Quasi-Static Models for Low-Velocity Impact- Induced Delamination of CFRP laminates .....	127
6.1.1 Prediction of Delamination Using Quasi-Static Impact Modeling: Theory.....	127
6.1.2 Prediction of Delamination Using Quasi-Static Impact Modeling: Development of FE Models.....	130
6.2 Quasi-Static Models for Low-Velocity Impact-Induced Delamination of CFRP laminates: Results .....	136
6.2.1 Results: Validation of FE Models Versus Literature .....	136
6.2.2 Results: Prediction of Delamination for 16-X, 32-X, 16-Q, and 32-Q Specimens.....	139
6.3 Quasi-Static Impact Modeling: Summary .....	143
CHAPTER 7: INFLUENCE OF SIMULATION-BASED DELAMINATION AND VOIDS ON ELECTRICAL RESISTANCE.....	144
7.1 Correlation Between Simulation-Based Delamination and Resistance .....	145
7.1.1 Integration of Simulation-Based Delamination into FE Models: Methods.....	145
7.1.2 Integration of Simulation-Based Delamination into FE Models: Results .....	148
7.2 Correlation Between Voids and Resistance using CT Images .....	152
7.2.1 Calculation of Void Content Using CT Images .....	152
7.2.2 Integration of CT Image-Based Voids into FE Models: Methods .....	157
7.2.3 Integration of CT Image-Based Voids into FE Models: Results .....	164
7.3 Influence of Delamination and Voids on Electrical Resistance: Summary.....	168
CHAPTER 8: CONCLUSIONS, RECOMMENDATIONS, AND FUTURE WORK.....	170
8.1 Conclusions.....	170
8.2 Recommendations and Lessons Learned.....	172
8.2.1 Recommendations and Lessons Learned: Experimental Work....	172

8.2.2 Recommendations and Lessons Learned: Recovery of Electrical Properties.....	173
8.2.3 Recommendations and Lessons Learned: FE Modeling.....	174
8.3 Future Work.....	175
APPENDIX A: ELECTRICAL .....	177
APPENDIX B: DELAMINATION PLOTS.....	182
REFERENCES .....	192

## LIST OF TABLES

Table 3. 1. List of Layup Sequences, Specimen Labels, Final Dimensions, and Cutting Method for all Impact Characterization Specimens.....	37
Table 3. 2. List of Layup Sequences, Specimen Labels, Final Dimensions, and Cutting Method for all Electrical Characterization Specimens .....	38
Table 3. 3. Electrical Properties Recovered from Experimental Line-Type and Point-Type 4-Probe Techniques .....	45
Table 3. 4. Current Source Magnitude vs. Resistance (per JIS K7194) .....	47
Table 3. 5. List of Layup Sequences, Specimen Labels, Final Dimensions, and Cutting Method for all Electrified-Impact Characterization Specimens .....	51
Table 3. 6. List of Layup Sequences, Specimen Labels, Final Dimensions, and Cutting Method for all CT Imaging Specimens.....	53
Table 4. 1. FE Model Parameters and Effective Dimensions .....	61
Table 4. 2. Material Properties Used in FE Models.....	61
Table 4. 3. Electrical Conductivity by Fiber Angle for 16-Q and 32-Q Specimens.....	69
Table 4. 4. Experimental and FE Results Using Line-Type 4-Probe Method .....	73
Table 4. 5. Experimental and FE Results For Quasi-Isotropic Specimens Using Line-Type 4-Probe Method .....	77
Table 4. 6. Experimental and FEM Results Using Point-Type 4-Probe Method .....	82
Table 4. 7. Optimized CFRP Material Properties to Achieve Ohmic Response Through the Full Material Thickness .....	89
Table 4. 8. Impact Data for Impact Characterization Tests and Coordinated Electrified-Impact Tests.....	96
Table 5. 1. Locations of damage modeled in finite element simulations. <sup>1</sup> For unidirectional specimens area is total cross sectional area. For cross-ply specimens area is percentage of individual layer cross sectional area.....	108
Table 5. 2. Specification of Delamination Damage for Damage Sensing Feasibility Study .....	110
Table 5. 3. Finite Element Results for Electrical Resistance for Fiber Breakage and Matrix Cracking Using 4-probe Method.....	112

Table 5. 4. Finite Element Results for Electrical Resistance Due to Delamination Using 4-probe Method.....	119
Table 5. 5. Finite Element Results for Electrical Resistance using Optimized Electrical Properties.....	123
Table 6. 1. Quasi-Static Impact Modeling Parameters (Note: Impact Energy And Velocity Are For Reference Only And Not Used In Quasi-Static Models).....	130
Table 6. 2. Quasi-Static Impact Modeling Parameters (Note: Impact Energy And Velocity Are For Reference Only And Not Used In Quasi-Static Models).....	134
Table 6. 3. Comparison of Delamination Major Axis Length in the Direct of Carbon Fibers for Validation of Quasi-Static FE Models.....	137
Table 6. 4. Delamination Major Axis Length Comparison .....	141
Table 7. 1. Experimental and FE Simulation Results for Top and Oblique Resistance for 16-Q and 32-Q Specimens.....	149
Table 7. 2. FE Simulation Results for Top and Oblique Resistance for 32-X and 16-X Specimens.....	150
Table 7. 3. Color Summary and Void Content of Specimens with 0, 4, and 7 Layers of BP .....	155
Table 7. 4. FE Simulation Results for Resistance in Fiber-, Transverse-, and Through Thickness-Directions for Specimens With and Without Voids .....	164
Table A. 1. 2-Probe High-Intensity Current Pulse Electrical Results .....	178

## LIST OF FIGURES

Figure 2. 1. Fiber breakage and matrix cracking of CFRP laminate using SEM [5].....	5
Figure 2. 2. Exploded view of CFRP laminate with fiber agglomeration at microscale. .	11
Figure 2. 3. Diagram of line-type 4 probe experimental method for (a) line of electrodes transverse to direction of electric current flow (b) line of electrodes oriented with fiber-direction (c) side view showing all 6 electrodes attached to top and bottom surface.....	12
Figure 2. 4. Electrode configuration for determining resistivity transverse to fiber direction [12].....	17
Figure 2. 5. Model of (a) microdefect and (b) macrodefect in electrical FE model of CFRP specimen [26].....	21
Figure 2. 6. Current constricted through contact of rough surfaces [47].....	26
Figure 2. 7. (a) Ultrasonic C-scan and (b) thermography images showing presence of voids in glass fiber-PEEK composites [48]. (c) SEM morphology of cross-sectional fracture in CNT BP composite [49] and (d) CT image slice showing delamination (yellow) in cross-ply CFRP laminate [50].....	27
Figure 3. 1. Rotary cutting tool and reinforced cutting wheel utilized for cutting specimens from larger panels.....	33
Figure 3. 2. Experimental setup for the application of coordinated pulsed electric current and low-velocity impact to CFRP composites [46].....	35
Figure 3. 3. Line-type 4-probe specimen with masking tape.....	40
Figure 3. 4. Experimental setup for electrical resistance testing using the line-type 4-probe method. ....	43
Figure 3. 5. (a) JIS K7194 4-point probe schematic. (b) Handheld measurement device for point-type 4-probe resistivity testing of CFRP laminates. ....	46
Figure 3. 6. Diagram of 4-point probe specimen and measurement locations based on JIS K7194.....	46
Figure 3. 7. Exploded view of fixture utilized for holding CFRP composites during electrical characterization, impact characterization, and coordinated electrical-impact testing [46]. ....	49
Figure 4. 1. Current source and sensing locations for oblique measurement plane.....	70

Figure 4. 2. Box plots of top resistance measurement for line-type 4-probe specimens with electrodes aligned with fiber direction of top ply.....	75
Figure 4. 3. Experimental resistance box plots [17]and FE simulation results for 16-ply and 32-ply quasi-isotropic specimens in top and oblique measurement planes. .	77
Figure 4. 4. Line-type 4-probe FE simulation plots of current density magnitude in $x - z$ plane for (a) 16-U specimens with line of electrodes aligned with fiber direction and (b) 16-X specimens with line of electrodes transverse to direction of fibers in top ply. ....	79
Figure 4. 5. Line-type 4-probe FE simulation plots of voltage distribution in $x - z$ plane for (a) 16-U specimens with line of electrodes aligned with fiber direction and (b) 16-X specimens with line of electrodes transverse to direction of fibers in top ply. ....	79
Figure 4. 6. Box plots of top resistance measurement for point-type 4-probe specimens with electrodes aligned with fiber direction of top ply. ....	83
Figure 4. 7. Box-plot for fiber direction resistivity of 16-U specimens, using line-type 4-probe method and point-type 4-probe methods. ....	85
Figure 4. 8. Electric current vs. time comparing specimens with 0, 4, and 7 layers of buckypaper at analog voltages of 50, 100, and 140V.....	92
Figure 4. 9. Average electrical resistance vs. current comparing specimens with 0, 4, and 7 layers of buckypaper.....	93
Figure 4. 10. Impact damage in the form of (a) line crack on unidirectional specimen and (b) delamination and fiber breakage on cross-ply specimen [45].....	97
Figure 4. 11. Average peak impact load for 32-U and 16-X impacted specimens. Error bars show highest and lowest values for individual specimens. ....	98
Figure 4. 12. Average absorbed energy for 32-U and 16-X impacted specimens. Error bars show highest and lowest values for individual specimens. ....	98
Figure 4. 13. Force versus deflection curves for specimen 16-X-11 with no current pulse and specimen 16-X-14 with high-intensity current pulse. ....	100
Figure 5. 1. Current load applied as current flux per unit area on the source electrodes in top resistance test.....	106
Figure 5. 2. Zones of damage located at center of specimen in finite element models...	107
Figure 5. 3. Locations of delamination damage for damage sensing feasibility study. ...	110



Figure 5. 4. Bar-plot for 4-probe top resistance for finite element simulations. Note: legend description “Top” refers to “Top Matrix Crack” and “Center-Top” refers to “Center-Top Fiber Breakage” in Tables III – IV.....	113
Figure 5. 5. Finite element plots of current density magnitude for 16-U-T specimens with (a) no damage and (b) a side matrix crack. ....	115
Figure 5. 6. Finite element plots of voltage potential for 16-U-F specimens with (a) no damage and (b) center-thru fiber breakage.....	116
Figure 5. 7. Finite element simulation results of (a) top resistance and (b) oblique resistance for specimens with none, small, moderate, and large delamination. ....	120
Figure 5. 8. Finite element simulation results of (a) top resistance on top surface, (b) oblique resistance on top surface, and (c) oblique resistance on bottom surface for 32-Q-T specimen type. ....	121
Figure 5. 9. Finite element plot of current density magnitude for 16-U-F-Opt specimen with no damage. ....	124
Figure 6. 1. Mesh for quasi-static impact model by (a) Moura et. al [3] and (b) current study. ....	127
Figure 6. 2. Boundary conditions and loads for quasi-static impact model. ....	128
Figure 6. 3. (a) Low-velocity impact test fixture and (b) FE boundary conditions and loads for quasi-static impact models. ....	131
Figure 6. 4. Mesh for quasi-static impact models. ....	131
Figure 6. 5. Location of static impact load for 12.7 mm radius (a) Delrin ® flat-ended and (b) steel hemispherical striker.....	133
Figure 6. 6. Delamination plots for interfaces in $[0_2/+45_2/-45_2/90_2]_S$ laminate by (a) DeMoura [3] and (b) current thesis. Delamination at each ply is oriented with fiber direction of lower adjacent ply (top to bottom: 45,-45,90,-45,45,0). ....	138
Figure 6. 7. Delamination plots at interface furthest from impact striker for (a) 16-X, (b) 16-Q-Low, (c) 16-Q-Int, (d) 16-Q-High, (e) 32-Q-Low, (f) 32-Q-Int, (g) 32-Q-High, (h) 32-X-Low, (i) 32-X-Int. Fiber direction of the lower-adjacent plies coincide with x-direction. ....	140
Figure 6. 8. Comparison of (a) FE delamination prediction and (b) CT image [50] at interface 27 for 32-X-Low specimen. (Note: FE plot in part (a) is full 152.4mm x 152.4mm specimen, whereas the CT image in part (b) is cropped to show detail in only a 45 mm x 45 mm section). ....	142

Figure 6. 9. Comparison of (a) FE delamination prediction and (b) CT image [50] at interface 26 for 32-X-Int specimen. (Note: FE plot in part (a) is full 152.4mm x 152.4mm specimen, whereas the CT image in part (b) is cropped to show detail in only a 45 mm x 45 mm section). .....	142
Figure 7. 1. 4-step procedure for incorporating simulation-based impact damage into electrical FE models.....	146
Figure 7. 2. (a) Matlab plot with delaminated area colored yellow and (b) ABAQUS Electrical FE Model with delaminated elements outlined in red for interface 1 for specimen 32-X-Low. Fiber direction of lower adjacent ply corresponds with x-axis.....	146
Figure 7. 3. Image stack of 30 interfaces for specimen 32-X-Low from (a) CT Scan, (b) Matlab damage prediction, and (c) ABAQUS electrical FE model.....	147
Figure 7. 4. Delamination plots of interface 1 with electrode locations shown for (a) specimen 32-X-High and (b) specimen 16-X. Fiber direction of lower adjacent ply corresponds with x-axis.....	151
Figure 7. 5. CT images of specimens with (a) 0, (b) 4, (c) 7 layers of BP with voids colored black, and (d) elliptical voids (yellow/black) running the length of the fibers. ....	153
Figure 7. 6 CT image stacks of specimens with (a) 0, (b) 4, (c) 7 layers of BP. Voids are colored black and yellow. Fiber direction corresponds to 1-direction.....	156
Figure 7. 7. 4-step procedure for incorporating CT image-based impact damage into electrical FE models.....	157
Figure 7. 8. 3-D model of CT image specimen 16-U-0BP with 16 datum planes shown in green. ....	159
Figure 7. 9. Example of CT image slice overlaid onto the 3-D model using the appearance gallery feature in Creo. ....	159
Figure 7. 10. 2-D sketch of rectangular needle-like voids running in the direction of the carbon fibers.....	160
Figure 7. 11. 3-D removal of void material using the extrude function in Creo. ....	160
Figure 7. 12. (a) Section view of voids from one image slice and (b) a rendering of a complete 3-D model with voids outlined in green.....	160
Figure 7. 13. ABAQUS mesh for void models of specimens (a) 16-U-0BP, (b) 16-U-4BP, and (c) 16-U-7BP. ....	162

Figure 7. 14. (a) Fiber bending/waviness around voids in a realistic composite versus (b) interpretation of voids in fiber-direction for a homogenized orthotropic material.....	163
Figure 7. 15. Locations of electrodes and current source for resistance measurement (a) transverse to fiber direction and (b) through-thickness. ....	163
Figure 7. 16. Side view showing distribution of voids for transverse resistance measurement for (a) 16-U-0BP, (b) 16-U-4BP, and (c) 16-U-7BP. Voids are outlined in green. ....	166
Figure 7. 17. Top view showing distribution of voids for through-thickness resistance measurement for (a) 16-U-0BP, (b) 16-U-4BP, and (c) 16-U-7BP. Voids are outlined in green. ....	167
Figure B. 1. Plot of simulation-based delamination predictions for [0/90] <sub>4S</sub> specimen 16-X for all 14 interfaces between plies with different fiber orientations. (Peak Impact Load = 9831 N, Striker type = 12.7mm flat). Interfaces numbered 1-14 from closest to impacted surface down. Yellow areas are predicted delamination.....	182
Figure B. 2. Plot of simulation-based delamination predictions for [0/45/-45/90] <sub>2S</sub> specimen 16-Q-Int for all 14 interfaces between plies with different fiber orientations. (Peak Impact Load = 3320 N, Striker type = 12.7mm round). Interfaces numbered 1-14 from closest to impacted surface down. Yellow areas are predicted delamination. ....	183
Figure B. 3. Plot of simulation-based delamination predictions for [0/45/-45/90] <sub>4S</sub> specimen 32-Q-Int for all interfaces between plies with different fiber orientations. (Peak Impact Load = 9020 N, Striker type = 12.7mm round). Interfaces numbered 1-30 from closest to impacted surface down. Yellow areas are predicted delamination.....	184
Figure B. 4. Plot of simulation-based delamination predictions for [0/90] <sub>8S</sub> specimen 32-X-Low for all interfaces between plies with different fiber orientations. (Peak Impact Load = 7786 N, Striker type = 12.7mm round). Interfaces numbered 1-30 from closest to impacted surface down. Yellow areas are predicted delamination.....	186
Figure B. 5. Plot of simulation-based delamination predictions for [0/90] <sub>8S</sub> specimen 32-X-Int for all interfaces between plies with different fiber orientations. (Peak Impact Load = 9253 N, Striker type = 12.7mm round). Interfaces numbered 1-30 from closest to impacted surface down. Yellow areas are predicted delamination.....	188

Figure B. 6. Plot of simulation-based delamination predictions for  $[0/90]_{8S}$  specimen 32-X-High for all interfaces between plies with different fiber orientations. (Peak Impact Load = 11748 N, Striker type = 12.7mm flat). Interfaces numbered 1-30 from closest to impacted surface down. Yellow areas are predicted delamination..... 190

## CHAPTER 1: INTRODUCTION

### 1.1 Background Information and Motivation

In the current engineering climate, engineers are tasked with designing next generation systems that achieve extraordinary performance. An optimized system is often one with: low energy consumption, minimal size, and high-efficiency. In order to achieve next level performance, traditional material options such as metals and plastics are often not sufficient. Composite materials consist of one or more reinforcement materials surrounded by a support material. The constituents of composite materials are inherently tailorable, which makes composite materials ideal in such highly specialized systems. For example, carbon fiber-reinforced polymer (CFRP) composites are known for having an excellent strength-to-weight ratio, which is highly desirable in the aerospace industry where weight management is critical. For example, the cost to launch the Space X Dragon cargo spacecraft was estimated in 2016 to range between \$9,100 to \$27,000 per pound [1], thus even highly expensive materials can provide significant cost savings. Conversely, in military ground vehicles, light-weighting initiatives often represent an increase in cost, but the benefits include improved mobility, transportability, and fuel-efficiency. Simply replacing metals with composites can provide modest improvements in performance, but in order to push beyond modest gains, more revolutionary approaches are needed. One such approach is the concept of multifunctional materials.

Multifunctional materials are material systems with a primary function (such as structural load-bearing) as well as one or more secondary functions (such as ballistic protection, energy storage, thermal shielding, etc.) For example, Volvo has developed a

composite vehicle with a structural battery built directly into to the body panels [2]. Therefore, in addition to the studies related to the mechanical behavior of composites, these recent advancements have motivated investigations concerned with the electrical and thermal performance. In the current study, the concept of multifunctionality is examined in CFRP composite laminates subjected to electromagnetic and mechanical fields. In particular, the study focuses on using electrical resistance of CFRP laminates as a metric for evaluating low-velocity impact damage.

## 1.2 Thesis Objectives

In the current thesis, electrical and impact damage models of multifunctional carbon fiber reinforced polymer matrix composites will be developed for the purpose of predicting and sensing low-velocity impact damage. The current study aims to provide a holistic approach to electrical resistance-based damage sensing. First, experimental methods will be used to characterize material response and recover material properties. Next, predictive models will be developed and validated versus the experimental data. Finally, the predictive models are to be used to elucidate new understanding on the material response. The four primary objectives of the current study include:

1. To conduct experimental testing to characterize the responses of CFRP composites of varying layup and thickness subjected to low-velocity impact, electrical current, and simultaneous electrical and impact loads.
2. To develop predictive 4-probe electrical models for resistance-based damage sensing applications of CFRP materials.

3. To evaluate the feasibility of the electrical models to sense localized damage of prescribed shape and location. The electrical models will also be used for evaluating the influence of voids on the electrical resistance, using data gathered from CT images.
4. To obtain realistic damage patterns from simulation and/or CT imaging data and determine the influence of the mechanical damage on 4-probe electrical response using finite element methods.

## CHAPTER 2: LITERATURE REVIEW

### 2.1 Low-Velocity Impact Characterization of Carbon Fiber-Reinforced Polymer

#### Composites

In the defense industry, significant attention and resources are focused on protecting composite vehicle structures from ballistic projectiles ( $>1,500$  ft/s). Although ballistic performance is undoubtedly critical in combat situations, low-velocity impact ( $<200$  ft/s) can silently degrade composite material performance during routine use. In ground vehicle applications, common low-velocity impact events include: road debris (rocks, etc.), maintenance (dropping tools, hitting components with wrenches, etc.), dropping loads (loading/unloading vehicle), and more. In aerospace applications, low-velocity impact threats comprise: flying objects (birds, hail, etc.), runway debris during takeoff/landing (rocks, etc.), dropping loads (loading/unloading aircraft), maintenance (dropping tools, hitting components with wrenches, etc.), and more. These common low-velocity impact events can have detrimental effects on structural performance of CFRP composites, and in some instances, the damage is not visible to the human eye. This type of damage is often referred to as Barely Visible Impact Damage (BVID). For instance, compressive strength of a CFRP laminate is reduced dramatically from delamination caused by low-velocity impact [3]. Moreover, when examining the interior microstructure of the composite via cross-section, it becomes clear that the majority of impact-induced delamination occurs in the lower plies of the laminate, which are furthest from the exterior (incident surface) [4]. This is in stark contrast to metals where the majority of impact damage occurs in the exterior surface. In response to the critical nature of impact



damage, a plethora of research studies have focused on characterizing and identifying low-velocity impact damage in CFRP composite laminates.

For CFRP laminated composites, impact damage is generally characterized as: fiber breakage, matrix cracking, fiber-matrix debonding/fiber pullout, and delamination. Several techniques are available for identifying each type of impact damage such as scanning electron microscopy (SEM), infrared thermography, radiographic inspection technique (RT), and acoustic emission. SEM and RT are valuable tools for visually identifying microscopic internal damage. Figure 2. 1. shows an example of internal impact damage of a CFRP composite with matrix cracking and fiber breakage. Pulse infrared thermography is another excellent technique for identifying very tiny internal damage based on characteristic thermal maps.

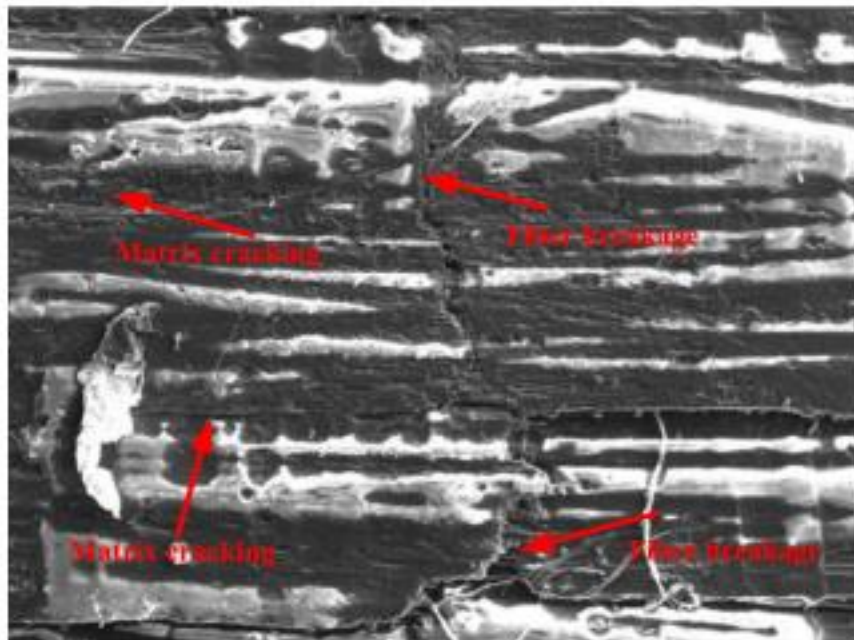


Figure 2. 1. Fiber breakage and matrix cracking of CFRP laminate using SEM [5].

Joint delamination, matrix cracking, and fiber breakage are readily identified with this technique by their characteristic block-shape, line-shape, and “I”-shape hot spots [5]. Additional studies have shown that the laminate stacking sequence has a significant influence on which damage modes occur in a specific CFRP specimen.

Unidirectional  $[0]_{12}$ ,  $[90]_{12}$ ,  $[45]_{12}$  and multidirectional  $[0/90]_{3s}$ ,  $[+45/-45]_{3s}$ ,  $[0/90/(+45/-45)_2]_s$  laminates were subjected to low-velocity impact using the Charpy impact method in order to determine the influence of stacking sequence on impact response [6]. The study demonstrated that the unidirectional  $[0]_{12}$  laminates exhibited relatively high absorbed energy from Charpy impact and damage was dominated by fiber breakage and delamination. The unidirectional laminates, however, had high local anisotropy in mechanical properties, which resulted in premature failure due to shear and local effects. The unidirectional  $[90]_{12}$  and  $[45]_{12}$  specimens showed very brittle behavior with significant matrix cracking and low absorbed energy. These findings confirmed the well-known trend that unidirectional laminates are not generally acceptable for practical applications. The cross-ply  $[0/90]_{3s}$  laminates exhibited similar impact performance and an improvement in material isotropy but had 25% decrease in flexural strength compared to the  $[0]_{12}$  laminates. The  $[+45/-45]_{3s}$  angle ply laminates claimed the best impact loading and high toughness, but had low flexural strengths, high strains. Damage was dominated by matrix cracking and delamination in these laminates. Finally, the  $[0/90/(+45/-45)_2]_s$  quasi-isotropic laminates showed high Charpy impact energy and flexural strength. These effects of stacking sequence on impact response were similar to previous trends on the effects of stacking sequence on tensile behavior [7,8]. Although Charpy impact tests are valuable in characterizing residual damage in CFRP laminates,

additional information can be gained through real-time monitoring of the impact response.

In an experimental study, piezoelectric transducer (PZT) sensors were attached to the surface of woven prepeg CFRP laminates with 11, 12, and 13 plies in order to record the sensor response during low-velocity impact [9]. The impact responses were compared to X-ray images of the damaged area in order to correlate the observed damage to a quantifiable response. The low-velocity impact events were at energies from approximately 10 J – 40 J. At low impact energy, no damage was sustained in the plates, whereas at the higher end of the energy range, noticeable damage was sustained. Moreover, it was found that as impact energy increased, the impact damage area increased proportionally. The vibration response frequency centroids were plotted as a function of impact energy, and it was demonstrated that the vibration response measured by the PZT transducers could be used for identifying both the presence and severity of damage. In the preceding experimental studies, it was shown that the material selection and stacking sequence have tremendous influence on the impact response and resulting impact-induced damage. In order to determine ideal stacking sequence and thickness, it is often necessary to test numerous options, which is expensive in both time and money. This has prompted recent efforts to focus on developing Finite Element (FE) models for predicting impact damage in CFRP composites.

De Moura and Marques [3] developed a FE model for predicting low-velocity impact damage in CFRP composites within the ABAQUS framework. The numerical model was based around a special 8-node shell element (S8R) that guarantees interlaminar shear stress continuity between differently oriented layers, which was

critical in order to predict delamination. Assumptions in the FE model included negligible transverse normal stress (through thickness direction) and quasi-static stress analysis. The quasi-static analysis was preferred due to savings in computational costs and was justified in that delamination can be predicted using only maximum impact force (i.e. does not require the dynamic force history). The shell element further improved computational costs, because it only required one element per layer thickness and allowed stress calculation at multiple points through the element thickness. The interlaminar shear stresses were then used in evaluating delaminations in the composite. The predicted delaminations from the FE model matched the shape and orientation of the experimental specimens very well, however the accuracy of the predicted delaminated area was only marginal. In order to better predict the delaminated area, progressive damage models have been developed.

A dynamic progressive damage model was developed by Liu et al. [10] for predicting low-velocity impact damage in CFRP laminates. A modeling plugin was developed using the ABAQUS-PYTHON scripting language, and explicit FE analysis was performed using the ABAQUS-VUMAT subroutine. Delamination was simulated using the bilinear cohesive model in ABAQUS. Chang-Chang, Hashin, and Puck failure criteria were compared to determine their accuracy within the model. The results demonstrated that in general, the error between the experimental and numerical model was smallest for the Puck failure criterion, which may be a result of the Puck criterion considering out-of-plane shear deformation effects, which were neglected in the Chang-Chang criterion. Although the Puck criterion was most accurate, the Puck criterion was most difficult for numerical implementation and had highest computational cost. For this

reason, Chang-Chang criterion is more widely used in commercial FE software. For all criteria, the dominant failure modes were delamination and matrix tension. Matrix tension damage initiated at the bottom of the impacted plate and ran along the direction of the fibers. Another significant finding was that incipient damage (first damage) was characterized by delamination, and incipient load (load corresponding to first damage) was not significantly affected by the total impact energy. Other FE models have been developed within commercial FE packages without the use of complex subroutines.

Farooq and Myler [11] utilized the commercial software package ABAQUS/Explicit for predicting damage and failure in thin-walled CFRP structures. The model employed built-in failure criteria, adaptive meshing techniques, and through-thickness effects for assessing ply-by-ply response of CFRP panels subjected to low-velocity impact. The Tsai-Hill and Tsai-Wu criteria showed limitations in predicting failure and accounting for through-thickness stresses. However, the FE model accurately predicted ply-level failure using the built-in Hashin failure criterion. The in-plane stresses were computed using a two-dimensional stress-based model while the through-thickness stresses were integrated using MATLAB code. While prediction of impact damage is of great interest to researchers and designers, for engineers who work with composites in the field, it is critical to have methods for sensing and evaluating damage of CFRP structures. A popular method for damage sensing of CFRP composites is based on the inherent electrical properties of carbon fibers.

## 2.2 Electrical Characterization of Carbon Fiber-Reinforced Polymer Composites

Historically, most research around CFRP composites focused on the mechanical and structural properties, however CFRP composites also have very unique electrical characteristics. When considering the microstructure of CFRP materials, each layer of the composite contains wire-like carbon fibers with very good electrical conductivity ( $\sim 9 \times 10^3$  S/m). These fibers are suspended within a polymer matrix, which is an insulator. The carbon fibers create an electrically conductive network that, at the macroscale, has very high conductivity in the direction of the carbon fibers (1-direction). Transverse to the fiber direction (2-direction), the polymer matrix acts as an insulator and electrical conductivity is reliant on fiber-to-fiber contact. The distribution of carbon fibers is generally not perfect, as the carbon fibers tend to agglomerate locally into bundles with many fibers in close proximity, as shown in Figure 2. 2. These bundles then form the conductive network through localized fiber-to-fiber contact points that are isolated within the insulating matrix. The volume fraction of fibers influences electrical resistivity transverse to fiber direction by affecting the density of contact points between adjacent fiber bundles [12]. The electrical conductivity transverse to fiber direction is typically 3 to 4 orders of magnitude lower than in the fiber direction [13–15]. When stacking the individual layers into a laminate, the electrical conductivity in the through thickness direction (3-direction) is typically further reduced compared to the 2-direction. The anisotropic electrical properties of CFRP laminates make experimental recovery of electrical properties much more complex than with isotropic materials.

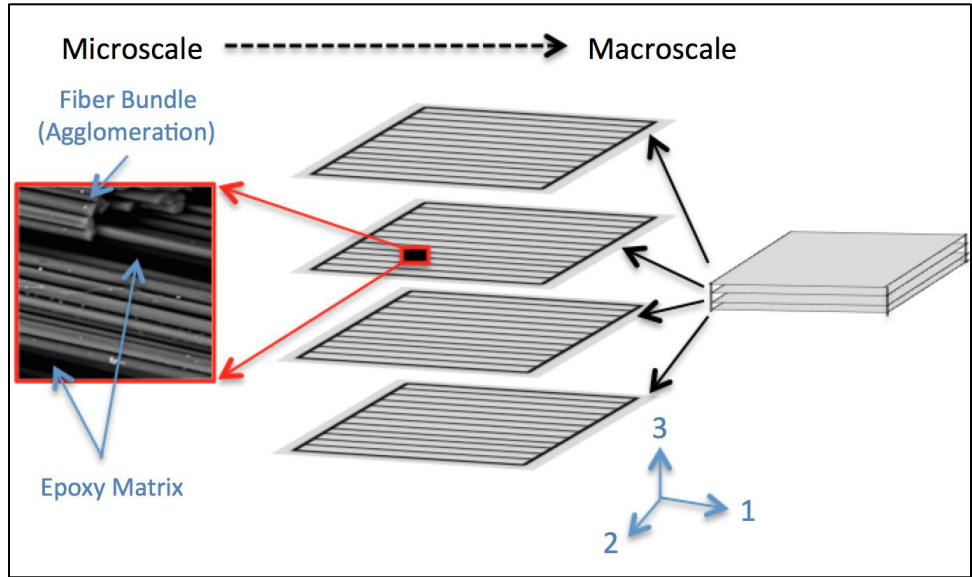


Figure 2. 2. Exploded view of CFRP laminate with fiber agglomeration at microscale.

If a traditional isotropic resistivity model is applied to an electrically anisotropic material, the resistivity recovered is a non-physical material parameter that is actually a combination of the resistivities in each of the principle directions. A few analytical models have been developed in order to illuminate the physics behind the electrical response of anisotropic materials. Busch et al. [16] used empirical data to validate an anisotropic resistivity model. The model was developed to determine the directionally dependent true resistivities of anisotropic crystals. The experimental method was based on a line-type 4-probe method where current source electrodes and measurement

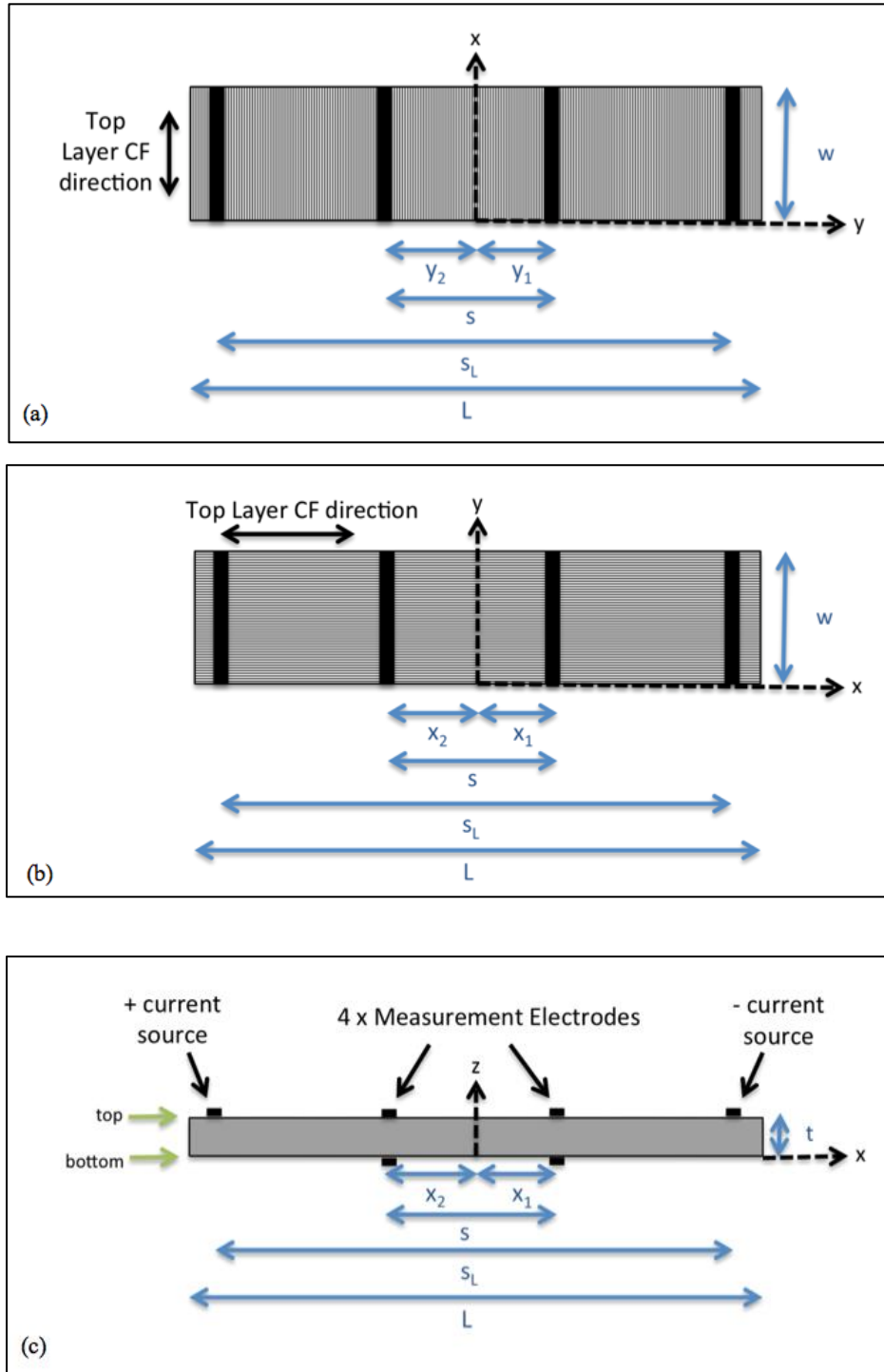


Figure 2. 3. Diagram of line-type 4 probe experimental method for (a) line of electrodes transverse to direction of electric current flow (b) line of electrodes oriented with fiber-direction (c) side view showing all 6 electrodes attached to top and bottom surface.



electrodes were placed in line on the top surface and two additional measurement electrodes were placed out of line on the bottom surface, as shown in Figure 2. 3. In this thesis, this method is referred to as a line-type 4-probe method, since the electrodes span the entire width of the specimen. Using this line-type 4-probe method and the anisotropic resistivity model below, the true resistivity can be determined for any given direction.

For recovery of electrical properties, it is critical that a 4-probe method is employed rather than a 2-probe method. In a 2-probe measurement method, only 2 electrode contacts are used for both current application and voltage measurement. In this configuration, the electrical resistance measured includes not only the CFRP material resistance but also the contact resistance between the electrode and the surface of the specimen. Conversely in the 4-probe method, the current application and voltage measurements are separated between 4 distinct contacts, which reduces the influence of the contact resistance from the electrical measurement and leads to more accurate and consistent measurements [17].

The subsequent mathematical formulation in (2. 1) - (2. 9) was originally developed by Busch et al. [16] and utilized the following notations: L is the length of the specimen, w is width, t is thickness, x-axis coincides with the fiber direction, z-axis denotes the through thickness dimension, and s is the spacing between the sensing electrodes, Figure 2. 3. The “true” resistivities in x-, y- and z-directions,  $\rho_x$ ,  $\rho_y$ , and  $\rho_z$ , cannot be obtained directly from the measured voltage and current due to non-uniform distribution of electric current within the specimen. The voltage distribution in the specimen of Figure 2. 3. (c) must satisfy the electrostatic equation:

$$\text{div } \mathbf{j} = \frac{1}{\rho_x} \frac{d^2 V}{dx^2} + \frac{1}{\rho_z} \frac{d^2 V}{dz^2} = 0 \quad (2.1)$$

The boundary condition of the electrostatic equation requires that the normal component of the electric current density,  $j_n$ , must vanish at the bottom of the specimen ( $z=0$ ) and at the edges ( $x=\pm L/2$ ). Just below the electrodes, the normal component of the current injection is given by (2. 2) and is zero elsewhere on the surface.

$$j_n = -\frac{1}{\rho_z} \frac{dV}{dz} \quad (2.2)$$

The boundary-value problem leads to a solution for voltage distribution in series form as:

$$V(x, z) = \sum_{n=1,3,5,\dots} V_n \sin \frac{\pi x}{L} \cosh \left[ \frac{n\pi z}{L} \left( \frac{\rho_z}{\rho_x} \right)^{\frac{1}{2}} \right] \quad (2.3)$$

An approximation of the voltage distribution is obtained by considering only the lowest order term of  $n=1$ . The coefficient  $V_1$  was determined using the condition that the integrated current density at the mid-plane of the material must be equal to the applied current. Voltage distribution at any location in the  $x$ - $z$  plane is:

$$V(x, z) = -\frac{I}{w} (\rho_z \rho_x)^{\frac{1}{2}} \frac{\sin \frac{\pi x}{L}}{\sinh \left[ \frac{\pi x}{L} \left( \frac{\rho_z}{\rho_x} \right)^{\frac{1}{2}} \right]} * \cosh \left[ \frac{\pi z}{L} \left( \frac{\rho_z}{\rho_x} \right)^{\frac{1}{2}} \right] \quad (2.4)$$

where  $I$  is the applied current.

In order to recover the electrical resistivities, experimental data is needed for  $V_{top}$  ( $z=t$ ) and  $V_{bot}$  ( $z=0$ ), which are obtained by taking voltage measurements on the top and

bottom surfaces, respectively, at the measurement electrodes in Figure 2. 3. (c).

Substituting these experimental values into (2. 4) yields two equations:

$$\left(\frac{\rho_z}{\rho_x}\right)^{\frac{1}{2}} \approx -\frac{L}{\pi t} \operatorname{arccosh} \left[ \frac{V_{top}}{V_{bot}} \right] \quad (2. 5)$$

$$(\rho_z \rho_x)^{\frac{1}{2}} \approx -\frac{V_{top} w}{2I \sin \frac{\pi S}{2L}} \tanh \left[ \frac{\pi t}{L} \left(\frac{\rho_z}{\rho_x}\right)^{\frac{1}{2}} \right] \quad (2. 6)$$

where the unknown parameters are  $\rho_x$  and  $\rho_z$ . The function (2. 6) has been approximated for large arguments of the term  $\rho_z/\rho_x$ , which is reasonable for CFRP materials as discussed previously. Additionally, expanding the functions  $\tanh()$  and  $\sin()$  in (2. 6) using Taylor's series, the following approximation was obtained:

$$(\rho_z \rho_x)^{\frac{1}{2}} \approx -\frac{V_{top} b L}{I \pi S} \quad (2. 7)$$

A significant facet of (2. 7) as compared to (2. 6) is that the specimen thickness  $t$  has disappeared from the equation, indicating that the current does not occupy the entire cross-section of the material [16]. The experimental work of Busch et al [16] found that the current density ( $j_x$ ) penetrates into the thickness of the electrically anisotropic material, however, the magnitude of the current density is exponentially damped within a thin surface layer. The current density within this surface layer is:

$$j_x(z) \approx j_x^0 e^{-|z|/z_{eff}} \quad (2. 8)$$

where the depth of current penetration,  $z_{eff}$ , was approximated as:

$$z_{eff} = \frac{L}{\pi} \left( \frac{\rho_x}{\rho_z} \right)^{\frac{1}{2}} \quad (2.9)$$

The term,  $z_{eff}$ , describes the depth of current penetration, which is not dependent on the overall thickness of the specimen but is dependent on the directional electrical resistivities.

The mathematical model in (2. 1) - (2. 9) has been applied to CFRP materials [12] in order to determine the electrical resistivity in the three principle directions of a unidirectional CFRP composite. In order to compute the parameters  $\rho_x$  and  $\rho_z$ , the experimental configuration of Figure 2. 3. (b) – (c) was employed to measure values for  $V_{top}$  and  $V_{bot}$ . Next, equations (2. 5) - (2. 6) were solved to recover the electrical properties  $\rho_x$  and  $\rho_z$ . In order to determine the transverse resistivity,  $\rho_y$ , a voltage measurement was taken transverse to the fiber direction, with electrodes placed in the configuration of Figure 2. 4. The true resistivity in the y-direction was determined using an optimization algorithm.

When recovering electrical properties from experimental measurement, precautions need to be taken to ensure that the electrical characterization is not affected by contact between the electrodes and the CFRP specimen. A potentially significant source of error exists in the attachment of the electrodes to the CFRP specimen. In order to reduce variability in the measurements, the surfaces of the CFRP specimen are often polished and electrodes are fixed to the surface using a silver paste. This method has been employed extensively for composite materials, however measurements are sensitive to

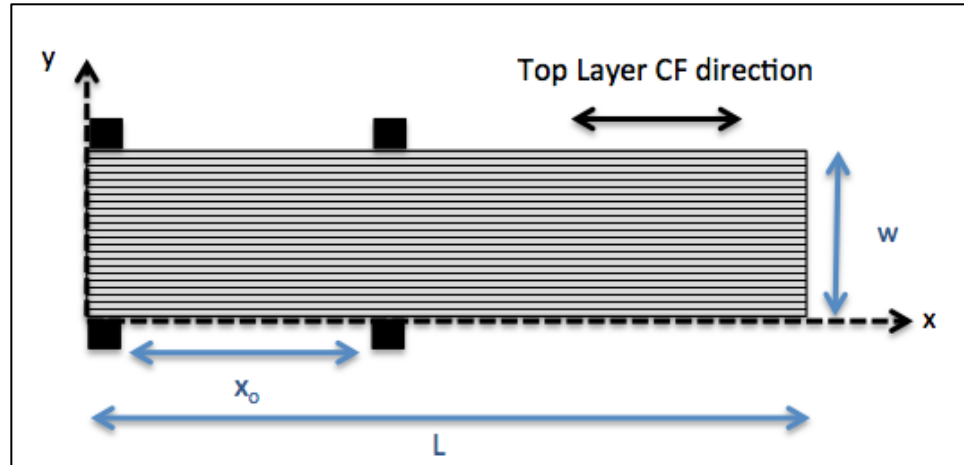


Figure 2. 4. Electrode configuration for determining resistivity transverse to fiber direction [12].

preparation of the surface and attachment of the electrodes via silver epoxy [17,18]. The line-type 4-probe method and silver epoxy treatment is not only used for recovery of material properties, but has been used extensively in the field of damage sensing.

### 2.3 Resistance-Based Damage Sensing

The performance benefits of CFRP composites are plentiful, however these high-performance materials are susceptible to impact-induced damage that is often undetectable to the human eye. When a load impacts the surface of a CFRP laminate, the visible surface may show no signs of damage, however the back surface of the material may show significant failure. In some cases, neither surface of the composite will show any damage, however, internal damage can weaken the structural integrity of the material. Numerous experimental studies have proved that monitoring changes in

electrical resistance can be an effective technique for damage sensing of CFRP composites.

In the field of resistance-based damage sensing, the dominant experimental methods are referred to as the potential method and the resistance method. In the potential method [15,19–21], current source electrodes are placed in a line on the surface of the specimen and the measurement electrodes are placed out-of-line. Measurement probes are arranged in an array across surface of the composite in order to identify the presence and location of internal damage. Although this method is useful for two-dimensional damage sensing, the potential method has limited sensitivity in that the distance between the current source line and potential gradient line results in voltage measurements that are orders of magnitude less than the source voltage. Current spreading further complicates the detection of damage using this method [22]. In the resistance method [17,18,22–25], current source and measurement probes are arranged along a single line which enables the resistance to be calculated through Ohm's law. This method achieves enhanced sensitivity to damage compared to the potential method, however electrode placement is critical in order to capture the appropriate damage modes. If damage is non-visible, it becomes difficult to ensure that the internal damage has been captured using the resistance method. When correlating electrical resistance to damage using the resistance method, each damage mechanism influences the electrical response differently.

Fiber breakage results in an increase in fiber-direction electrical resistivity due to discontinuities in the path of current flow. Fiber-matrix debonding and matrix cracking increase the resistivity in the directions transverse to fiber direction and through thickness

due to a reduction in contact points between adjacent fiber bundles. Finally, delamination increases through thickness resistivity due to a reduction in contact between the fibers in adjacent lamina. Four distinct measurement planes are used to capture these damage mechanisms [17,18]. The top and bottom surface measurement planes provide excellent sensitivity to fiber breakage whereas the through thickness measurement plane provides the most sensitive response to delamination and fiber-matrix debonding. The oblique plane (i.e.: through the thickness at an oblique angle) measurement is sensitive to all three damage modes [22].

McAndrew and Zhupanska [17] studied the influence of low-velocity impact on electrical resistance in AS4/3501-6 CFRP laminates with layup arrangements of  $[0/45/-45/90]_{2s}$  and  $[0/45/-45/90]_{4s}$ . The specimens were square 152.4mm x 152.4mm with thicknesses of 2.25mm and 4.5mm, respectively. Line-type 4-probe resistance measurements were observed through the top and oblique measurement planes. For a single impact event, the oblique resistance was found to be more sensitive to impact damage compared to the top surface resistance. The top resistance measurement failed to capture the impact damage in several of the specimens, even with visible impact damage. Although in this study the resistance method did show limited success in identifying impact damage, the measurements were not sensitive enough to distinguish between the magnitudes of impact energy applied to the specimen. In another empirical study of cumulative low-velocity impact damage, the capabilities of the resistance and potential methods were compared.

IM7/epoxy composites with quasi-isotropic layup configuration  $[0/45/90/-45]_{3s}$  and thickness of 3.2mm were subjected to repeated low-velocity impact [19]. It was

found that as the impact energy continued to increase, the electrical resistance increased as well. Moreover, in order to maintain good sensitivity in the 2-D potential method it was necessary to keep close proximity between the current source line and the potential gradient (voltage sensing) line. Overall, in the 2-D potential method, the impact damage caused a change in voltage potential of only up to 6%. In the 1-D resistance method, however, the resistance measurement increased as much as 1700% due to the cumulative low velocity impact. In another study, Angelidis et al. [15] studied the electric potential technique for damage detection in Hexcel T300/914 cross-ply composites with layup configurations of  $[0_2/45_2/90_2/-45_2]_s$ . In this investigation, the potential method provided better sensitivity of up to 45% compared to undamaged specimens. While material characterization necessitates the use of empirical investigation, through finite element analysis (FEA) a plethora of additional information becomes available on the electrical response in CFRP composites. For example, in the preceding study, 2-D voltage potential contours revealed noticeable distortions around the damaged region [15].

Additional finite element (FE) models were developed for simulating line-type 4-probe resistance and potential tests for damaged and undamaged CFRP composites [13]. The FE models were developed in ABAQUS and utilized linear, quadrilateral elements. The material in the two-dimensional FE model was given a fixed longitudinal (fiber direction) conductivity and the through thickness conductivity was varied from approximately  $10^{-3}$  to 1 times the conductivity of the fiber direction. These models demonstrated accuracy only for very large through thickness conductivity (similar in magnitude to fiber direction conductivity), which is typically a false assumption for CFRP materials [13–15]. In a different numerical FE based model of unidirectional



CFRP composites [26], microscopic fiber breakage was accounted for by modifying the material resistivity at the local elements (see Figure 2. 5 (a)). At larger scales, however, discontinuities required the removal of the damaged elements from the volume of the model thus ensuring that the current passes around and not through the damaged sections (see Figure 2. 5 (b)). Contemporary advancements in nanomaterials have led to further enhancements in the sensitivity of electrical resistance-based damage sensing for CFRP composite materials.

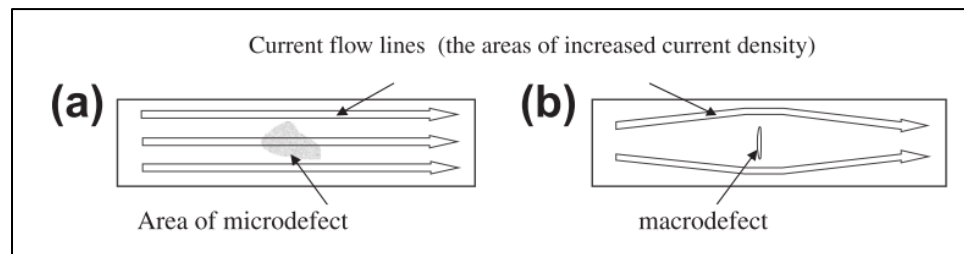


Figure 2. 5. Model of (a) microdefect and (b) macrodefect in electrical FE model of CFRP specimen [26].

Gallo and Thostenson [27,28] presented a comparative study on the damage sensing capabilities of cross-ply CFRP and glass/carbon nanotube (CNT) composites. FE COMSOL models were developed such that each layer of the composite was modeled as a homogenous orthotropic material and the cracks were modeled as an electrical insulation boundary condition. In  $[0/90]_s$  CFRP specimens, the high fiber-direction conductivity in the outer layers resulted in low current density in the interior transverse plies. The low current density in the interior plies resulted in reduced sensitivity to transverse cracks located in the inner lamina. In the model of glass-CNT composites, the material had similar electrical conductivity in fiber, transverse, and through thickness

directions, which improved the sensitivity of detecting interior cracks. Dispersing CNT's within the epoxy matrix has also been demonstrated to improve the capability of CFRP composites in damage sensing applications [29]. Similar findings were reported for CNT/ultra-high-molecular-weight polyethylene fiber composites subjected to uniaxial loading [30]. The sensitivity of the nanotube network to damage was strongly dependent on the nanotube distribution. The CNT distribution influences the electric percolation behavior at the micro scale. A related investigation confirmed a significant improvement in through-thickness electrical conductivity in glass fiber reinforced composites when CNT's were dispersed in the polymer matrix [31]. The use of these so-called "smart" materials within traditional composites has become a trending topic in the composite materials community.

Recently a new smart polymer nanocomposite layer was developed, based on semiconductor  $\text{Cu}_2\text{S}$  nanoparticles within a polystyrene matrix [32]. Under UV-light excitation, the photo-luminescent smart layer emitted light within the visible range. This smart layer allowed for optical identification of low-velocity impact damage in a non-destructive manner. Modern efforts have focused on incorporating damage sensing capabilities in-situ for real-time damage sensing of a structure in the field. This class of composite materials is commonly referred to as multifunctional composite materials, because the composite structure may serve several functions such as structural load bearing, electrical damage sensing, ballistic protection, thermal shielding, and more.

## 2.4 Multiphysics Interactions in Composites

In ground vehicle and aerospace applications, design engineers are tasked with the developing structures with lower weight, higher strength, and improved fuel efficiency. Moreover, the structures must enclose and/or interact with high performance systems with enormous electrical and thermal loads, while minimizing the size of the design envelope. In order to accommodate all of these requirements, one solution is to treat a composite structure as a multifunctional material. Multifunctionality suggests combining multiple subcomponents (load carrying, sensing, control, power, ballistic protection, etc.) into a single multifunctional component with the potential to improve overall system efficiency. Composite materials lend themselves well to the concept of multifunctionality due to their multiphase nature and inherent tailorability. For example, Reifsnider et al. [33,34] have successfully developed a heterogeneous functional material, called HeteroFoaM, with functionally tailored electrochemical, thermal, and mechanical material properties. Multifunctionality is not only of interest at the manufacturing level, but is also of great interest in field applications. Raihan et al. [35] have developed models for predicting changes in dielectric properties due to mechanical loads. This concept is similar to the electrical resistance-based damage sensing methods discussed previously, which rely on the interactions between mechanical and electrical fields. While resistance-based damage sensing is an example of how mechanical loads can affect electrical properties, additional studies have demonstrated the ability of utilizing electrical loads to influence mechanical response.

Carbon nanotube foams exhibited promising shock absorbing characteristics due to electro-mechanical coupling via coordinated application of a programmable electric

field and low velocity impact [36]. Magnetic fields have been successfully employed for slowing down metal projectiles at low (5 m/s) [37] and medium (600 m/s) [38] velocity. At high velocity (1000 m/s), magnetic braking has demonstrated potential to change the shape of a projectile, which could aid in defeating the threat to the impacted surface [37]. For CFRP laminates, application of electromagnetic fields can have appealing effects on impact resistance.

Experimental studies [39,40] revealed that CFRP composites exhibited higher impact resistance when exposed to an electrical field during a low-velocity impact event. Moreover, as the intensity of the applied current increased, the impact resistance continued to increase. When subjected to direct current (DC) [39–43], electrical resistance and Joule heating were limiting factors in the maximum current intensity that could be applied to AS4/3501-6 and IM7/977-3 composites without causing thermal degradation of the material. These results stimulated further theoretical studies by Barakati and Zhupanska [14,44] on the effects of applying pulsed electromagnetic fields of high magnitude and short duration. The study aimed to enhance electromagnetic field effects while reducing the detrimental thermal effects by applying high intensity current pulses for a very short duration. The results invigorated experimental studies to examine the response of CFRP composites subjected to simultaneous application of high-intensity pulsed electric fields and low-velocity impact [45,46], which were conducted by the author of the current thesis.

Hart and Zhupanska [46] evaluated the influence of high-intensity current pulse (up to ~1,700A) on low-velocity impact resistance of unidirectional IM7/977-3 [0]<sub>32T</sub> specimens by comparing the impact response to control specimens with no electric

current applied. The specimens exhibited a decrease in electrical resistance as electric current increased. The average peak impact load and average absorbed energy increased by as much as 22% and 13%, respectively when an electric current pulse was applied compared to specimens with no current pulse. In 16-ply unidirectional IM7/977-2 [0]<sub>16T</sub> and cross-ply IM7/977-2 [0/90]<sub>4S</sub> specimens, the benefits of the current pulse were marginal due to high electrical resistance and thermal degradation of the specimens [45]. One cause of the thermal degradation was identified as a rough mating surface between the CFRP specimen and the copper electrodes that applied the electric current. As the current flowed from the highly conductive copper electrode to the less conductive CFRP material, current was constricted at the interface, which caused heating. This problem was exacerbated by the fact that epoxy matrix was insulating, meaning that the current was constricted through very tiny contact points where the carbon fibers were in direct contact with the copper electrode as shown in Figure 2. 6. Such microscale phenomena are not visible to the naked eye and require advanced techniques to be evaluated. One such technique commonly used for composites is computerized tomography (CT) imaging.

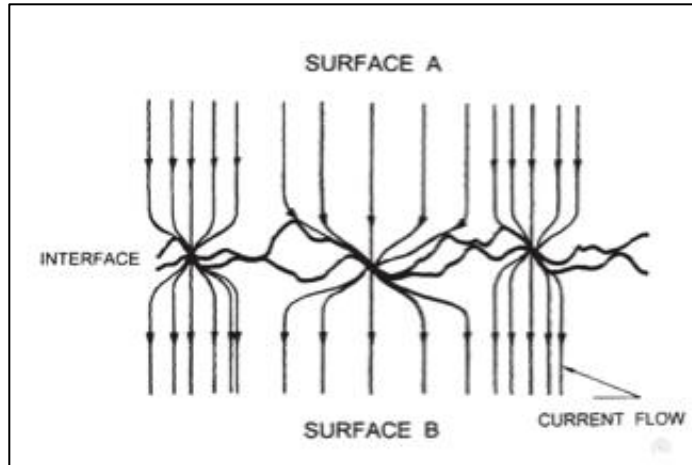


Figure 2. 6. Current constricted through contact of rough surfaces [47].

### 2.5 Computerized Tomography Imaging of Composites

Several non-destructive imaging techniques are available for elucidating the microstructure of composite materials. Ultrasonic C-Scan inspection involves sending ultrasonic pulses into the composite material. In the standard pulse-echo mode, the waves are either reflected off of the back surface of the specimen or reflected off of a flaw interface. The time and amplitude of the reflected wave provide information on internal damage in composite materials. Rather than using ultrasonic waves, thermography relies on application of a brief heat flow into the composite material. Internal flaws affect the ability of the material to transmit heat, and thus these flawed areas are identified using infrared cameras [48]. Examples of ultrasonic and thermography images are shown in Figure 2. 7. (a) – (b). These aforementioned methods are useful in identifying damage, however, superior imaging resolution is achieved through scanning electron microscopy (SEM), as displayed in Figure 2. 7. (c). SEM produces images of a specimen through the use of a focused beam of electrons that interacts with the atoms in the material, and the

resulting signals give information on the material composition down to the nanoscale. SEM has been successfully used for identifying individual carbon fibers, CNT's, voids, cracks, and delaminations in laminated composite materials [48,49]. A disadvantage of SEM is that specimens may require significant preparation, such as application of a metallic coating, in order to reflect the electrons properly. CT imaging serves as an excellent alternative for developing 3-D images of microstructure within a composite material.

Synonyms for CT imaging include X-Ray computed tomography (X-Ray CT) and computerized axial tomography scan (CAT Scan). A CT scan is performed by taking

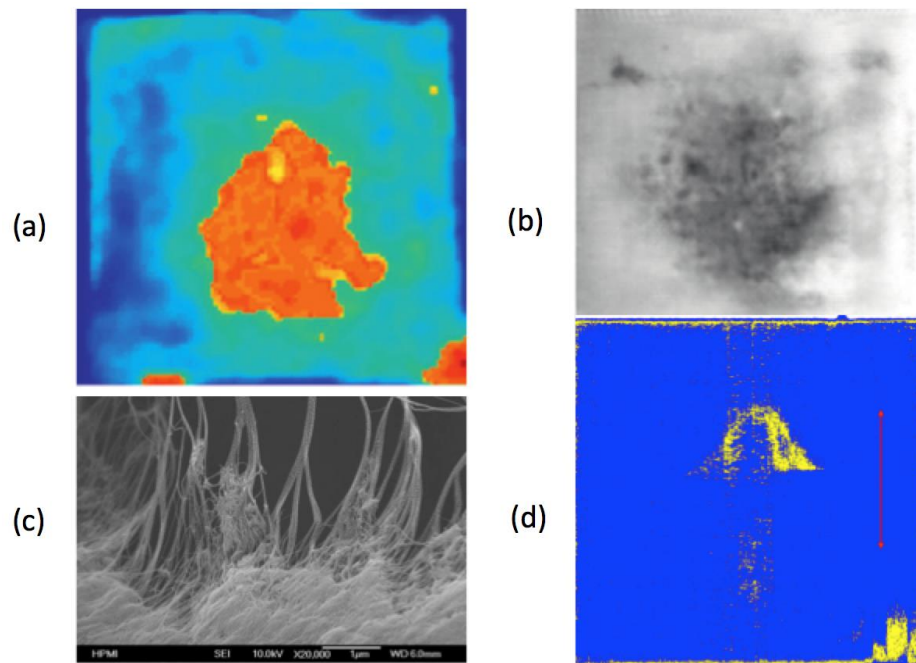


Figure 2. 7. (a) Ultrasonic C-scan and (b) thermography images showing presence of voids in glass fiber-PEEK composites [48]. (c) SEM morphology of cross-sectional fracture in CNT BP composite [49] and (d) CT image slice showing delamination (yellow) in cross-ply CFRP laminate [50].

several 2-D X-ray images around a single axis of rotation. The 2-D image slices are then assembled via digital image processing to form a full 3-D image of the internal structure of the scanned object. This method utilizes differences in density and X-ray absorption to distinguish the local microstructure [50]. This technique has been refined over the past several decades for medical applications and in more recent years has been used for illuminating the microstructure of CFRP composites.

Tensile damage, in the form of micro-delamination and transverse cracking, has been identified using CT images in CNT conductive networks [30]. Haboub et al. [51] developed an experimental setup for in-situ X-ray tomography during tensile testing and was able to capture matrix cracks that were bridged by continuous fibers. Song [52] used CT imaging for quantifying low-velocity impact damage in satin weave carbon-epoxy composites. Demerath [50] performed similar analysis for studying delamination caused by low-velocity impact in IM7/977-3 cross-ply laminates. In this study, 152.4 x 152.4 mm IM7/977-3 [0/90]<sub>8s</sub> specimens were subjected to low-velocity impact at high enough energy to cause internal delaminations as well as visible perforation on the back surface of the specimen. For CT imaging, resolution can be improved as the size of the specimen decreases, so the damaged area of interest was cut from the larger specimen. The damaged region was isolated to the local impact point, so the specimens were cut down to 45 x 45 mm size for CT scanning. Once the 3-D CT image was developed, one image slice per layer was extracted for processing. The gray-values of the image slices were set so that the damaged areas showed up as yellow and undamaged areas were blue, as shown in Figure 2. 7 (d). The images were then processed through a custom Matlab code, which integrated the damaged areas to determine the total damaged volume as a percent



of the specimen volume. These methods provide a useful tool to compare experimental results to numerically predicted damage.

## 2.6 Literature Review: Summary

While CFRP composite laminates provide engineers with exceptional design flexibility and high strength-to-weight ratio, characteristics such as modest impact resistance and low toughness leave some designers hesitant to convert. This has prompted significant investment into researching impact response and damage evolution in CFRP composites. In the field of damage sensing, much recent attention has focused on developing real time, in-situ damage sensing system. One such method, utilizes the electrical conductivity of the carbon fibers to sense the presence and intensity of internal damage. It is often difficult to characterize internal damage through electrical resistance measurement alone. In order to illuminate the interior microstructure of damaged CFRP specimens, FE models and CT imaging provide excellent insight. In the current thesis, the preceding methods were used in parallel to develop a comprehensive framework for electrical resistance-based damage sensing in CFRP laminates. The first step was to characterize the electrical and impact response of the CFRP specimens. Next, FE models were developed for both predicting impact-induced damage as well as sensing the damage using electrical resistance measurement. Finally, CT imaging results were utilized for validation of FE predictions and as well as for further analysis of the interior microstructure.

## CHAPTER 3: EXPERIMENTAL METHODS

The experimental techniques in the current study were aimed at investigating the relationship between electromagnetic and mechanical fields in CFRP laminates. CFRP laminates of varying thickness, layup, and composition were included in the study (Section 3.1) to determine their influence on the experimental response. Low velocity impact characterization was completed in order to set a baseline for impact response for each specimen type (Section 3.2). Next, electrical characterization (Section 3.3) was performed to provide a control for the electrical response of the CFRP specimens. The anisotropic electrical resistivities of the specimens were recovered using a traditional line-type 4-probe method (Sections 3.3.1 – 3.3.2). Next, a newly developed point-type 4-probe method was employed to reduce geometry effects on the resistance measurements (Section 3.3.3). Additionally, the specimens were subjected to a high-intensity current pulse and the electrical response was observed (Section 3.3.4). Once the impact and electrical characterization was performed, specimens were subjected to simultaneous application of low-velocity impact and high-intensity current pulse in order to determine the influence of the current pulse on the impact response of the specimens (Section 3.4). Finally, select specimens were analyzed via CT imaging in order to observe the local microstructure and to analyze the effects that the microstructure may have had on the electrical and impact responses (Section 3.5). Some of the experimental methods presented in the following sections 3.2 – 3.4 have been detailed in previously published work by author of the current thesis. More detailed information on impact characterization (Section 3.2), 2-probe electrical characterization (Section 3.3.4), and

coordinated electrified-impact testing (Section 3.4) can be found in these previous works [45,46].

### 3.1 Description of Specimens

The CFRP specimens tested in this study varied in thickness, layup, fiber-composition, and epoxy-matrix type. The specimens included 9 different specimen types: (1) IM7/977-3 [0]<sub>32T</sub> called 32-ply unidirectional, (2) IM7/977-3 [0/90]<sub>8S</sub> called 32-ply cross-ply, (3) IM7/977-2 [0]<sub>16T</sub> called 16-ply unidirectional, (4) IM7/977-2 [0/90]<sub>4S</sub> called 16-ply cross-ply, (5) AS4/3501-6 [0/45/-45/90]<sub>4S</sub> called 32-ply quasi-isotropic, (6) AS4/3501-6 [0/45/-45/90]<sub>2S</sub> called 16-ply quasi-isotropic, (7) IM7/977-3 [0]<sub>16T</sub> also referred to as CF<sub>16</sub>, (8) CF<sub>2</sub>/[BP/CF<sub>4</sub>]<sub>3</sub>/BP/CF<sub>2</sub>, and (9) [CF<sub>2</sub>/BP]<sub>7</sub>/CF<sub>2</sub>. Specimens types (7), (8), and (9) each contained 16 layers of unidirectional IM7/977-3 carbon fibers (CF). Specimen types (8) and (9) also included 4 and 7 layers of carbon nanotube buckypaper (BP). For example, in the layup arrangements above, CF<sub>2</sub> designates two layers of unidirectional carbon fiber and BP indicates the placement of a single ply of carbon nanotube buckypaper. The layup arrangements above give very detailed information on the material constituents of each specimen type.

In the standard notation for carbon fiber composite laminates, the identifiers IM7 and AS4 distinguish the carbon fiber type. IM7 and AS4 carbon fibers are both high performance aerospace grade carbon fibers with high stiffness and strength. The IM7 fibers have tensile strength and modulus approximately 15-20% higher compared to AS4 fibers (6K Tow) [53,54]. The numbers 977-2 and 977-3 after the slash identify the type of matrix. 977-2 and 977-3 are toughened epoxy resins with exceptional impact properties. The materials properties of the two epoxy types are very similar; however, the 977-2

epoxy resin has a slightly higher tensile strength of 2690 MPa at room temperature compared to 2510 MPa for 977-3 [55,56]. The term in the square bracket identifies the lamina orientation. Unidirectional, or  $[0]_{\#T}$ , signifies that all plies are oriented in the same direction. Cross-ply, or  $[0/90]_{\#S}$ , indicates that the fiber orientation in each layer alternates at  $0^\circ$  and  $90^\circ$  and the “S” indicates that the layers are symmetric with respect to the middle plane of the laminate. The specimens  $[0/45/-45/90]_{\#S}$  are often referred to as quasi-isotropic laminates, because the stacking sequence is arranged such that the material properties simulate an isotropic material [57]. The total number of plies in a laminate is determined by adding the number of plies in the brackets, then multiplying by the subscript number, and finally multiplying by 2, if the laminate is symmetric. For example, an AS4/3501-6  $[0/45/-45/90]_{4S}$  laminate contains  $4 \times 4 \times 2 = 32$  plies of AS4 fibers in a 3501-6 epoxy matrix. For all specimens utilized in the current work, large panels were manufactured in an autoclave or similar manufacturing process requiring intense heat and pressure. The first step in the specimen preparation process was to cut large specimen panels down to the desired dimensions.

The final specimen dimensions were achieved by cutting larger sheets to size. The preferred method of cutting used in the current study was CNC water-jet. This method has been utilized for cutting CFRP laminates by Demerath [50] and Hill [58]. These studies found that the CNC water-jet cutting method minimized free edge delamination compared to use of a table saw [17,18,43,45,46,59]. In order to further minimize free edge delamination at the start and end of the cutting path, Demerath left small stabilization tabs attached to the specimens, which were then cut off by hand. Some of the 4-probe specimens in the current study had been previously impacted and thus the

surfaces of the specimen were damaged and no longer flat. These specimens could not be secured within the CNC water-jet machine, so they had to be cut by hand. These specimens were cut using a Dremel ® style rotary tool with a special fiberglass-reinforced cutting wheel, as shown in Figure 3. 1. The cutting wheel does contain any cutting teeth but instead uses abrasion to cut through the specimen without causing delamination. This cutting method worked well for small specimens requiring minimal cutting, but would not be appropriate for larger specimens, because the friction of the cutting wheel could cause excessive heating and potential thermal damage to the specimen.



Figure 3. 1. Rotary cutting tool and reinforced cutting wheel utilized for cutting specimens from larger panels.

In the current thesis, each group of specimens was given a specimen label in the form of: number of carbon fiber plies – layup (unidirectional, cross-ply, or quasi-

isotropic) – specimen number. For example 32-X-2 refers to the second specimen with the layup IM7/977-3 [0/90]<sub>8S</sub>. The three batches of specimens containing BP included an additional term indicating the number of BP plies. For instance, 16-U-4BP-3 refers to the third specimen with the layup CF<sub>2</sub>/[BP/CF<sub>4</sub>]<sub>3</sub>/BP/CF<sub>2</sub>. Throughout this paper, the results are reported as average results for multiple specimens of the same type. For example the average results for the three specimens 16-U-1, 16-U-2, and 16-U-3 are referred to in general as results for “16-U” specimens. If the individual specimen number is used, such as 32-Q-1, then the reported result is only for the single individual specimen. A full summary of test specimens, labeling notation, dimensions, and cutting method are detailed in Table 3. 1., Table 3. 2., Table 3. 5, and Table 3. 6.

### 3.2 Impact Characterization

Low-velocity impact characterization was performed using an Instron 8200 Dynatup low-velocity impact tester, as shown in Figure 3. 2. The Instron 8200 is suited primarily for plastic and composite materials and is capable of a maximum drop height of 1 meter, maximum impact velocity of 4.4 m/s, and maximum impact energy of 132.8 Joules. The drop height was measured as the distance between the top surface of the clamped specimen and the bottom of the striker head, with the drop weight carriage at the set position. The striker consisted of a load cell, or tup, and a tup insert that covers the outside of the load cell and comes in direct contact with the test specimen. The stock tup inserts were electrically conductive tool steel and posed a concern for electrified impact testing. A custom dielectric flat-ended tup insert with the same diameter (15.88 mm) as the standard tup was fabricated. The tup insert was machined from DELRIN® material, which boasts excellent impact resistance and low electrical conductivity. The release

mechanism was customized in order to integrate within the electrified-impact setup. The release mechanism was outfitted with an air-actuated cylinder and 12 V air solenoid, which enabled the release of the drop carriage to be controlled from a remotely located PC and coordinated with the application of a high-intensity current pulse.

The short-term application of electric current has been shown to improve the impact performance of CFRP laminates in previous work [39,42,45,46,58]. The full experimental setup in Figure 3. 2. was developed so that low-velocity impact could be coordinated with application of a high-intensity current pulse. However, in order to

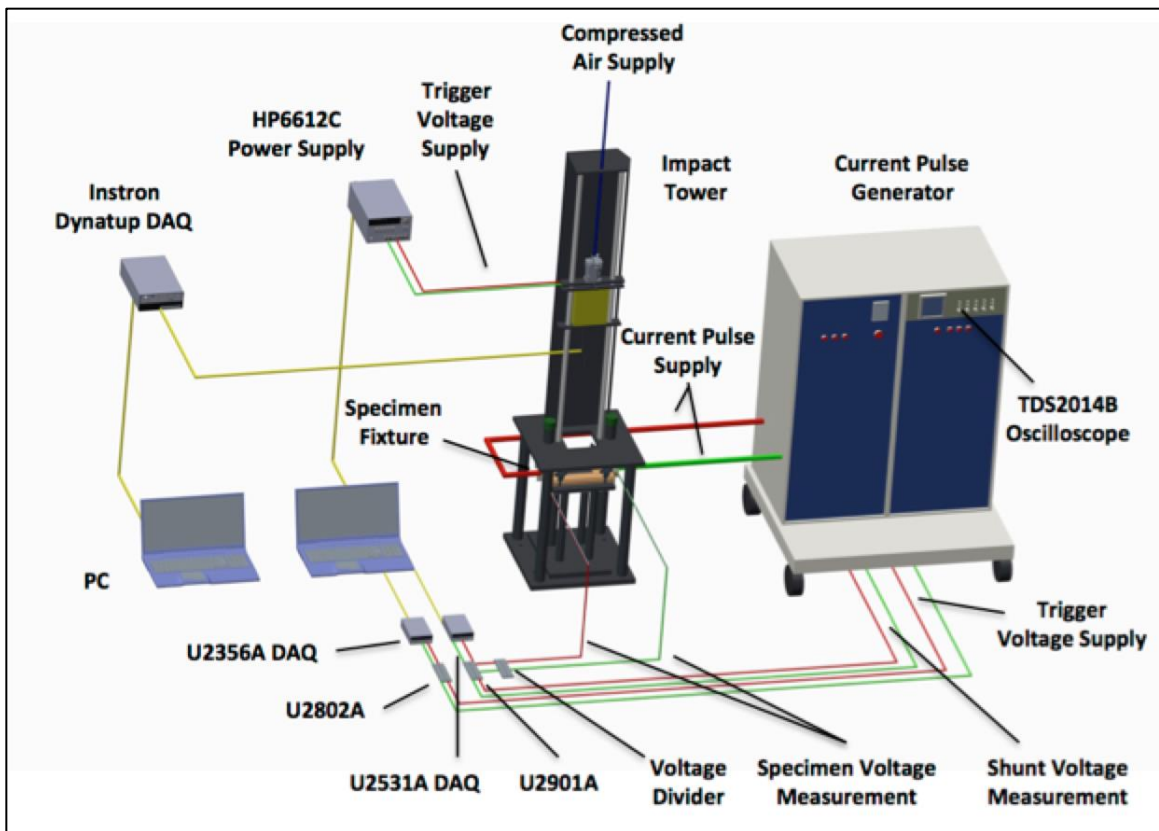


Figure 3. 2. Experimental setup for the application of coordinated pulsed electric current and low-velocity impact to CFRP composites [46].

understand the influence of the current pulse on impact behavior, impact characterization testing was required as a baseline with no electric current applied.

Impact characterization testing was performed on specimens in Table 3. 1. for CFRP specimens with varying layup and thickness. The impact tests were carried out at sufficient energy to cause barely visible impact damage such as localized matrix cracking, fiber breakage, and delamination, but not so high energy to cause complete perforation of the specimen. The Instron Dynatup Impulse DAQ (5 MHz sampling rate, built-in filtering and conditioning) was utilized for monitoring impact force throughout the impact event. The Dynatup software package automatically calculated acceleration by dividing force by mass at each time step. Next, velocity was determined through integration of the acceleration versus time, and subsequently, deflection through integrating velocity versus time. Finally, energy was determined by integrating the force versus deflection curve. All integrations were performed numerically using the trapezoidal technique. After completing impact characterization, electrical characterization tests were performed on the specimens using 3 different measurement techniques.



Table 3. 1. List of Layup Sequences, Specimen Labels, Final Dimensions, and Cutting Method for all Impact Characterization Specimens

Specimen Type	Qty	Specimen ID #’s	t [mm]	L [mm]	w [mm]	s [mm]	s <sub>L</sub> [mm]	Cut Method
IM7/977-2 [0] <sub>16T</sub>	3	16-U-10,11,12	2.31	152.4	152.4	--	--	Table Saw
IM7/977-3 [0] <sub>32T</sub>	3	32-U-10,11,12	4.23	152.4	152.4	--	--	Table Saw
IM7/977-2 [0/90] <sub>4S</sub>	3	16-X-10,11,12	2.30	152.4	152.4	--	--	Table Saw
CF <sub>16</sub>	1	16-U-0BP-10	2.15	152.4	152.4	--	--	CNC Water-Jet
CF <sub>2</sub> /[BP/CF <sub>4</sub> ] <sub>3</sub> /BP/CF <sub>2</sub>	1	16-U-4BP-10	2.23	152.4	152.4	--	--	CNC Water-Jet
[CF <sub>2</sub> /BP] <sub>7</sub> /CF <sub>2</sub>	1	16-U-7BP-10	2.35	152.4	152.4	--	--	CNC Water-Jet
AS4/3501-6 [0/45/-45/90] <sub>4S</sub>	11	16-Q-1,...,11	2.25	152.4	152.4	30.0	90.0	Table Saw
AS4/3501-6 [0/45/-45/90] <sub>2S</sub>	12	32-Q-1,...,12	4.50	152.4	152.4	30.0	90.0	Table Saw

### 3.3 Electrical Characterization

As discussed in the literature review Section 2.2, for electrical resistance measurement of CFRP composites, common experimental methods involve the use of a line-type 4-probe method (discussed in Section 3.3.1). The term “line-type” indicates that the electrodes span the entire width of the specimen and are in uniform contact across the width. This is in contrast to “point-type” 4-probe methods, which will be discussed in Section 3.3.2. All 4-probe methods utilize 2 electrodes for the current source (1 positive and 1 negative) and 2 separate electrodes for sensing (1 positive and 1 negative). Using this method, the contact resistance of the electrode/composite interface due to the current source electrodes is removed from the measurement at the sensing electrodes [17]. For this reason, the 4-probe methods are generally preferred over 2-probe methods, where the

Table 3. 2. List of Layup Sequences, Specimen Labels, Final Dimensions, and Cutting Method for all Electrical Characterization Specimens

	Specimen Type	Qty	Specimen ID #'s	t [mm]	L [mm]	w [mm]	s [mm]	s <sub>L</sub> [mm]	Cut Method
Line-Type 4-Probe Method	IM7/977-2 [0] <sub>16T</sub>	6	16-U-1,...,6	2.31	75.0	25.0	20.0	73.5	Cutting Wheel
	IM7/977-3 [0] <sub>32T</sub>	6	32-U-1,...,6	4.23	75.0	25.0	20.0	73.5	Cutting Wheel
	IM7/977-2 [0/90] <sub>4S</sub>	6	16-X-1,...,6	2.30	75.0	25.0	20.0	73.5	Cutting Wheel
	CF <sub>16</sub>	6	16-U-0BP-1,...,6	2.15	152.4	50.0	40.0	80.0	Cutting Wheel
	CF <sub>2</sub> /[BP/CF <sub>4</sub> ] <sub>3</sub> /BP/CF <sub>2</sub>	6	16-U-4BP-1,...,6	2.23	152.4	50.0	40.0	80.0	Cutting Wheel
	[CF <sub>2</sub> /BP] <sub>7</sub> /CF <sub>2</sub>	6	16-U-7BP-1,...,6	2.35	152.4	50.0	40.0	80.0	Cutting Wheel
	AS4/3501-6 [0/45/-45/90] <sub>4S</sub>	11	16-Q-1,...,11	2.25	152.4	152.4	30.0	90.0	Table Saw
	AS4/3501-6 [0/45/-45/90] <sub>2S</sub>	12	32-Q-1,...,12	4.50	152.4	152.4	30.0	90.0	Table Saw
Point-Type 4-Probe Method	IM7/977-2 [0] <sub>16T</sub>	2	16-U-7,8	2.31	80.0	50.0	--	--	Cutting Wheel
	IM7/977-3 [0] <sub>32T</sub>	2	32-U-7,8	4.23	80.0	50.0	--	--	Cutting Wheel
	IM7/977-2 [0/90] <sub>4S</sub>	2	16-X-7,8	2.30	80.0	50.0	--	--	Cutting Wheel
	CF <sub>16</sub>	3	16-U-0BP-7,8,9	2.15	80.0	50.0	--	--	Cutting Wheel
	CF <sub>2</sub> /[BP/CF <sub>4</sub> ] <sub>3</sub> /BP/CF <sub>2</sub>	3	16-U-4BP-7,8,9	2.23	80.0	50.0	--	--	Cutting Wheel
	[CF <sub>2</sub> /BP] <sub>7</sub> /CF <sub>2</sub>	3	16-U-7BP-7,8,9	2.35	80.0	50.0	--	--	Cutting Wheel
Current Pulse 2-Probe Method	IM7/977-2 [0] <sub>16T</sub>	3	16-U-7,8,9	2.31	152.4	152.4	--	--	Table Saw
	IM7/977-3 [0] <sub>32T</sub>	3	32-U-7,8,9	4.23	152.4	152.4	--	--	Table Saw
	IM7/977-2 [0/90] <sub>4S</sub>	3	16-X-7,8,9	2.30	152.4	152.4	--	--	Table Saw
	IM7/977-2 [0/90] <sub>8S</sub>	3	32-X-7,8,9	2.30	152.4	152.4	--	--	Table Saw
	CF <sub>16</sub>	3	16-U-0BP-7,8,9	2.15	152.4	152.4	--	--	CNC Water-Jet
	CF <sub>2</sub> /[BP/CF <sub>4</sub> ] <sub>3</sub> /BP/CF <sub>2</sub>	3	16-U-4BP-7,8,9	2.23	152.4	152.4	--	--	CNC Water-Jet
	[CF <sub>2</sub> /BP] <sub>7</sub> /CF <sub>2</sub>	3	16-U-7BP-7,8,9	2.35	152.4	152.4	--	--	CNC Water-Jet

measurement includes contact resistance as the current source and sensing electrodes are the same (1 positive electrode for both source and sensing and 1 negative electrode for both source and sensing). In some applications, such as application of high-intensity current pulse (Section 3.3.3), the 4-probe methods are not appropriate, so 2-probe methods must be employed. A summary of electrical characterization specimen layout, dimensions, and cutting method are tabulated in Table 3. 2.

### 3.3.1 Line-Type 4-Probe Method: Experimental Methods

In the current work, the line-type 4-probe experimental methods were developed based on the previous 4-probe electrical resistance methods for electrically anisotropic materials. The specimen preparation process was adapted from McAndrew and Zhupanska [17,18] and the electrode placements were adapted from Busch et al. [16]. The 16-U, 32-U, and 16-X specimens were cut to the dimensions 25.0 mm x 75.0 mm, whereas the 16-U-0BP, 16-U-4BP, and 16-U-7BP specimens were cut to dimensions of 152.4 mm x 50.0 mm. The different specimen sizes were selected due to availability of materials, but also demonstrated that the methods presented herein were independent of specimen size. For each of the specimen types in Table 3. 2., 3 specimens (labeled – 1,2,3) were cut so that the carbon fibers in the top layer of the specimen were oriented transverse to the line of electrodes (see Figure 2. 3. (a)) and 3 specimens (labeled – 4,5,6) were cut with the fibers aligned with the line of electrodes (see Figure 2. 3. (b)). The cut specimens were then labeled with a marker according to the labeling scheme discussed previously. Once the specimens were cut to the final size, the surfaces needed to be prepared for attachment of the electrodes.

In order to improve contact between the electrodes and carbon fibers, as well as decrease noise in the results, the specimens were lightly sanded at the location of each of each electrode [21]. Progressively, 220, 400, and 600 grit sandpaper was used to sand at the electrode locations. The sandpaper was wrapped around 8mm wide plywood block to aid in ensuring flat, even sanding over the surface of the specimen. The sanding operation was intended to remove some of the epoxy covering the outermost fibers in order to improve electrical conduction between the fibers and copper electrodes. The specimens were then covered with masking tape, leaving 3mm wide sanded strips exposed. Each strip was centered over the desired electrode location, as shown in Figure 3. 3. The use of masking tape was critical in ensuring that the electrode strips were straight as to not affect the electrical measurements.

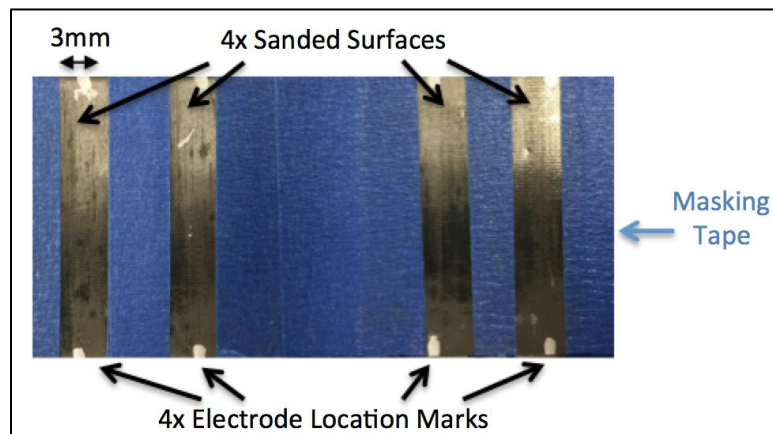


Figure 3. 3. Line-type 4-probe specimen with masking tape.

The next step in the specimen preparation procedure was fabrication of the copper electrodes. 22-gauge copper bus wires were cut to 80mm length and utilized as the copper electrodes. The electrodes were straightened by hand using needle nosed pliers. In

order to further improve electrical contact between the electrodes and specimen, conductive filler was employed. High purity silver conductive paint, manufactured by SPI, was utilized for attaching the copper electrodes to the specimen. According to the manufacturer datasheet, the silver paint had a bulk resistivity of  $3 \times 10^{-5} \Omega\text{-cm}$  and typical adhesion tensile strength of  $1000 \text{ N/cm}^2$ . A thin layer of the silver paint was applied to the exposed surfaces on the top of each specimen using the brush attached to the cap of the silver paint. Careful consideration was made to ensure that paint was only applied to the top surface of the specimen and that no silver paint was applied to the cut edges that run through the thickness of the specimen so that the electrical results would not be compromised. Each electrode was positioned over the top of each specimen so that the electrode was centered in the wet paint at locations specified by Figure 2. 3. (c) and Table 3. 2. A second layer of silver conductive paint was applied over the copper electrodes to improve adhesion. Specimens were allowed to set for 2 hours to allow the paint to dry.

A bead of LOCTITE® Hysol® E-120HP high strength, low viscosity epoxy was applied over each electrode to improve adhesion of the electrodes to the CFRP specimen and ensure that the electrodes would not break off due to handling. After drying for 24 hours, the specimens were turned over, and the process above was repeated for the bottom surface of the specimens. After all electrodes were placed, the masking tape was removed from each specimen, and the excess electrode wire was trimmed such that the top and bottom surface electrodes would overhang on opposite sides of the specimen. Once the specimens were prepared, the resistance of the each specimen was studied.

The Agilent DC Power Supply, capable of providing up to 20 V and 2 A, was selected as the current source for all tests in the present study. The Agilent 34420A 7 ½

Digit Nano Volt/ Micro Ohm Meter, capable of measuring up to 120V, was utilized for data acquisition. Voltage measurements between the top sensing electrodes were recorded as  $V_{\text{top}}$  where as measurements across the bottom sensing electrodes were recorded as  $V_{\text{bot}}$ . Figure 3. 4. displays a schematic of the full experimental test setup. Each resistance test was repeated 6 times on each specimen at 10 mA and the results were averaged for each set of 3 similar specimens. During initial resistance testing using the line-type 4-probe method, the results for specimens containing layers of BP did not follow expectations. Dr. David Andersen (University of Iowa Department of Electrical and Computer Engineering) suggested that the line-type electrodes might be introducing edge effects into the voltage measurements. The line-type electrodes spanned the full width of the specimen from edge to edge. When electrodes are placed close to the boundary (edge), the current distribution can be significantly distorted, which can cause an increase in the measured potential drop [60]. In order to reduce these edge effects, one method is to use sharp point-type probes at measurement locations away from the specimen boundary.

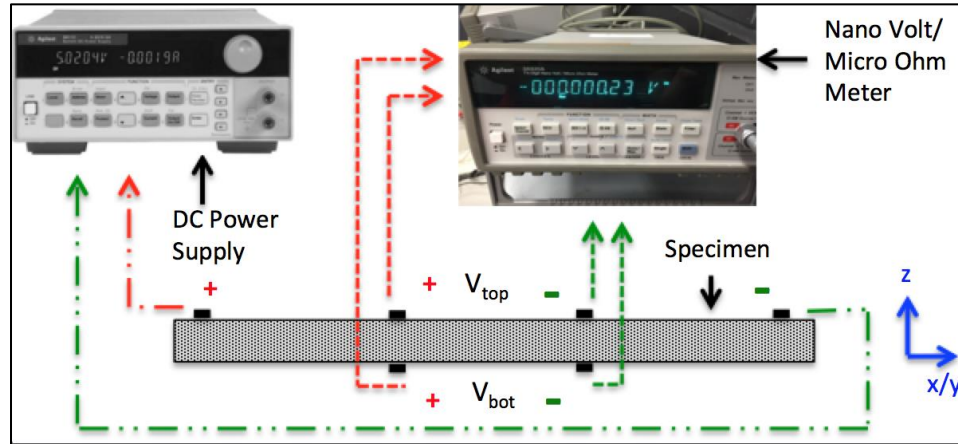


Figure 3. 4. Experimental setup for electrical resistance testing using the line-type 4-probe method.

### 3.3.2 Recovery of Experimental Electrical Resistivity

Using the experimental methods of Section 3.3.1 and the analytical model of Busch et al. [16], a straightforward process was developed for recovering the anisotropic electrical resistivities for unidirectional CFRP laminates. If top and bottom voltage measurements are available from experimental data and the thickness of the specimen is small, the fiber-direction resistivity  $\rho_x$  and through-thickness resistivity  $\rho_z$  can be calculated using equations (2. 5) and (2. 6). However, when the effective thickness is less than the physical specimen thickness, it may not be possible to record a bottom voltage measurement. Moreover, based on the previous discussion, even if a very small bottom voltage measurement is registered, the response could be non-linear, which would cause the method to break down. Nonetheless, if the resistivities in the transverse-direction  $\rho_y$  and through thickness-direction  $\rho_z$  are comparable in magnitude, then the current will penetrate through the full thickness of the specimen, which enables both top and bottom

voltage measurements. The directional resistivities  $\rho_x$ ,  $\rho_y$ , and  $\rho_z$  were recovered through a systematic procedure as follows:

1. Measure  $V_{top}$  and  $V_{bot}$  using line-type 4-probe method with top ply fibers oriented transverse to the line of electrodes (i.e.: replace the x-direction coordinate with y-direction coordinate in all equations above).
2. Calculate  $\rho_y$  and  $\rho_z$  using  $V_{top}$  and  $V_{bot}$  from step 1 and equations (2. 5) and (2. 6) (replace the x-direction coordinate with y-direction coordinate in both equations).
3. Measure  $V_{top}$  only for line-type 4-probe method with fibers oriented with the line of electrodes ( $V_{bot}$  may not be available as discussed above).
4. Calculate  $\rho_x$  using equation (2. 7) and the  $\rho_z$  and  $V_{top}$  obtained from steps 2 and 3.

Utilizing the procedure in steps 1 – 4, the directional resistivities,  $\rho_x$ ,  $\rho_y$  and  $\rho_z$ , and corresponding directional conductivities  $\sigma_x$ ,  $\sigma_y$  and  $\sigma_z$ , were calculated based on experimental measurements for unidirectional specimens. It is noteworthy, that bulk electrical properties could not be recovered directly from specimens with layers containing alternating fiber orientations (i.e. cross-ply and quasi-isotropic specimens). Therefore for cross-ply and quasi-isotropic specimens, the material properties in principle material directions were assumed to be the same as the unidirectional specimens. Therefore, the material properties from unidirectional specimens were used in the development of FE models for cross-ply and quasi-isotropic specimens, which demonstrated the power of the methods to predict an electrical response for specimens



with varying thickness and layup. A summary of recovered electrical properties is listed for unidirectional specimens in Table 3. 3.

Table 3. 3. Electrical Properties Recovered from Experimental Line-Type and Point-Type 4-Probe Techniques

Specimen Type	Bulk Electrical Properties Recovered from Line-Type 4-Probe Method						Point-Type Method
	$\sigma_x$ [S/m]	$\rho_x$ [Ohm-cm]	$\sigma_y$ [S/m]	$\rho_y$ [Ohm-cm]	$\sigma_z$ [S/m]	$\rho_z$ [Ohm-cm]	$\rho_x$ [Ohm-cm]
16-U	29330	0.0034	1.61	62.3	0.287	348.4	0.0036
32-U	35146	0.0028	1.19	82.2	0.237	422.5	0.0036
16-U-0BP	10993	0.0091	1.51	66.2	0.539	185	0.0111
16-U-4BP	5185	0.0193	67.24	1.487	6.59	15.2	0.0183
16-U-7BP	8533	0.0117	162.34	0.616	15.917	6.3	0.0129

### 3.3.3 Point-Type 4-Probe Method: Experimental Methods

The Japanese Industrial Standard (JIS) K7194 [61] specifies a testing method for resistivity of conductive plastics with a four-point probe array. The JIS K7194 method is meant for testing conductive plastics with known thickness up to 20mm. Per the standard, the specimens must be rectangular-shaped with dimensions 50 mm x 80 mm ( $\pm 0.2$  mm). Compared to the line-type 4-probe method, this technique utilizes a handheld probe device (see Figure 3. 5) rather than epoxy-fixed electrodes. This handheld device allows for measurements to be recorded at 9 locations across the surface of the specimen, as shown in Figure 3. 6. The measurements are repeated using forward and reverse current directions so that a total of 18 unique measurements are recorded for each test specimen. The measurements at each location are adjusted using a correction factor. In 4-point probe theory, the correction factor can adjust for edge effects and the thickness of the specimen [62].

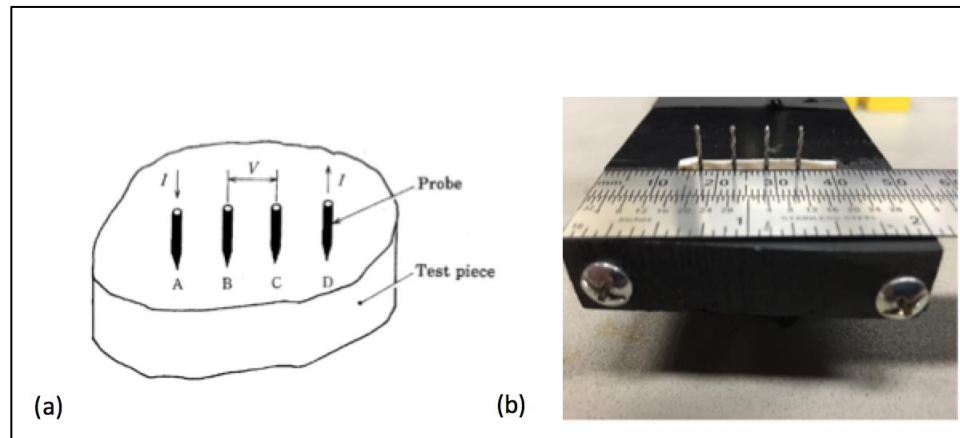


Figure 3. 5. (a) JIS K7194 4-point probe schematic. (b) Handheld measurement device for point-type 4-probe resistivity testing of CFRP laminates.

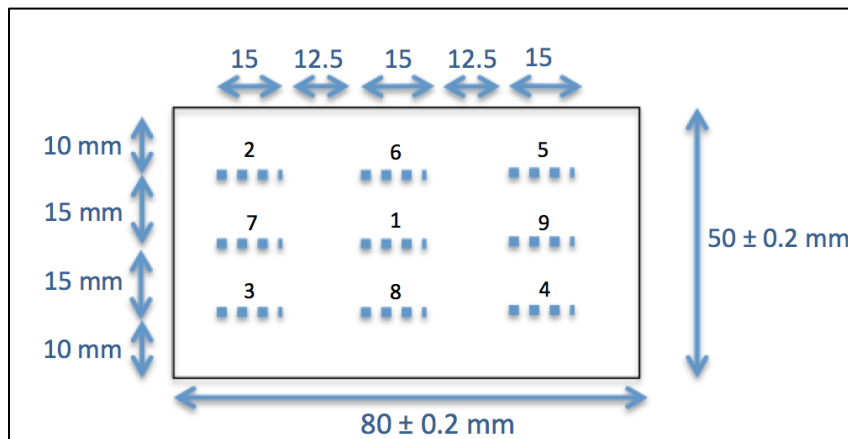


Figure 3. 6. Diagram of 4-point probe specimen and measurement locations based on JIS K7194.

The standard calls for a constant current source of 1  $\mu$ A to 100 mA, per Table 3.

4. In the current work, a direct current source of 10 mA was applied using the Agilent DC Power Supply. Although some resistance measurements were outside of the range for the 10 mA source, it was determined that all tests should be carried out at the same current to

avoid errors due to the scale of measurement. The current was applied through two outer electrodes and measured through the two inner electrodes. The four electrodes were spaced equally at a distance of 5mm point-to-point. The standard called out 0.5 to 0.8 mm tungsten probes (or material with similar conductivity) with spherically worked ends. Due to availability of materials, the probes in the current work were 0.8mm diameter tungsten carbide probes with tips machined to a 118° tip. The probes were secured within an ABS support structure, and wire leads were soldered to the probes at the end opposite the machined tip. The methods of JIS K7194 were based on the assumption of isotropic electrical properties so in order to be adapted to anisotropic CFRP laminates certain modifications were required.

Table 3. 4. Current Source Magnitude vs. Resistance (per JIS K7194)

Resistance of test piece	< 200 mΩ	< 20 Ω	< 2 kΩ	< 20 kΩ	< 200 kΩ	< 2 MΩ
Applied current $I_0$	100 mA	10 mA	1 mA	100 μA	10 μA	1 μA

After preliminary testing, it was determined that the surfaces of the CFRP specimens needed to be sanded in order to improve contact between the point-type electrodes and carbon fibers. The surface of the specimen was sanded lightly using 220, 400, and 600 grit sandpaper in a manner similar to the previous methods of the line-type 4-probe method [17,18]. The sanding operation was used to remove the top layer of epoxy so that the electrodes could come in direct contact with the conductive carbon fibers. Once the specimens were sanded, the 9 measurement locations were marked on

the surface of the specimen using a permanent marker. The probe device was then placed at each location under a force of approximately 10 lbs. to ensure full and even contact of the probes. This force was much greater than the standard callout of 1 – 2 N, but was necessary due to the hardness of the composites and sporadic fiber-electrode contact points.

### 3.3.4 2-Probe High Intensity Current Pulse: Experimental

#### Methods

In the previous work of Hart and Zhupanska [45,46], a custom current pulse generator was built for simultaneous application of high magnitude, short duration electric pulses and low-velocity impact to CFRP composite specimens. The experimental setup included: a custom-built current pulse generator, impact tower, data acquisition, triggering devices, and programming required to coordinate the simultaneous application of the current pulse and impact load to the tested specimens. The system, shown in Figure 3. 2., centered around a custom-built electric current pulse generator that utilized a bank of capacitor modules capable of producing a 20 millisecond current pulse with an amplitude of up to 2500 A. The setup allowed for real-time measurements of pulsed electric current, voltage, resistance, load, and deflection. Operation of the experimental setup was semi-automatic so that the user could set certain parameters for each test and then observe the test from a safe distance.

During the electrical characterization tests, current entered the edge of the CFRP specimen through a positive electrode and exited the opposite side of the specimen from the negative electrode, as shown in Figure 3. 7. Voltage was measured between these two electrodes and specimen resistance was calculated by dividing the voltage by current.

The electrical characterization tests were carried out using the TDS 2014B oscilloscope as the data acquisition system. The Tektronix TDS 2014B oscilloscope, capable of sampling up to 100 MHz over 4 channels, was installed directly into the pulse generator housing for convenient data acquisition. Since the current source electrodes and measurement electrodes were one in the same, this method was referred to as the 2-probe method. It is important to note that in the 2-probe method, the measured specimen resistance also includes contributions from the contact resistance at the interface of the

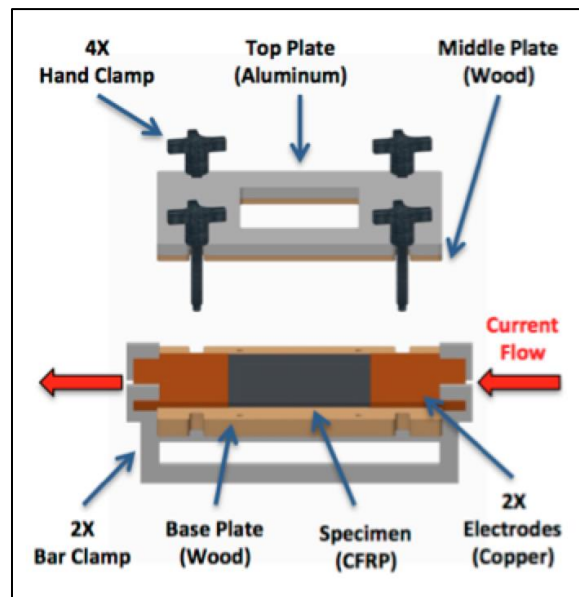


Figure 3. 7. Exploded view of fixture utilized for holding CFRP composites during electrical characterization, impact characterization, and coordinated electrical-impact testing [46].

CFRP specimen and the copper electrodes. Electrical characterization tests were performed on the specimens in Table 3. 2. at various current magnitudes in order to

observe the influence of the high-intensity current pulse on the CFRP and CFRP/BP specimens.

### 3.4 Coordinated Electrified-Impact Testing

Once the impact characterization and 2-probe electrical characterization tests were complete, tests were performed using simultaneous application of low-velocity impact and high-intensity current pulse in order to determine the influence of the current pulse on impact behavior. The full experimental setup in Figure 3. 2. was operated in a systematic, semi-automatic manner. Operation of the system was controlled using two personal computers and an Agilent VEE Pro 8.5 program.

For coordinated electrical-impact testing, both data acquisition and triggering were controlled remotely. The Agilent U2531A and U2901A were used for sampling electrical data at a rate of 10,000 samples per second. The voltage drop across the shunt resistor ( $\ll 1$  V) and specimen (up to 100 V) differed by orders of magnitude, thus the signals needed to be scaled to better match the resolution of the DAQ, which measures 0 to  $\pm 10$ V. The voltage across the shunt resistor was amplified by a factor of 11 using an amplifier built into the current pulse generator, and specimen voltage was reduced by a factor of 21 through a voltage divider with accuracy of 1%. A second PC was employed for data acquisition from the impact tower.

The experimental setup was operated by the following procedure: (1) Set U2356A voltage output to 5 V to prepare the current pulse trigger, (2) current pulse generator is powered on and set to desired voltage, (3) user alerts the program that the system is ready to fire, (4) the program waits “X” seconds, as specified by the user, before continuing with the program so that the user can move to a safe location prior to triggering the

current pulse, (5) HP6612C power supply output is set to 12V to release the drop carriage on the Instron 8200 impact tower, (6) the system then waits a specified delay of “Y” seconds as the drop carriage falls, (7) immediately before onset of low-velocity impact, the program sets the output of the Agilent U2356A to 0 V, which triggers the current pulse generator to fire and the DAQ’s to begin data collection, and (8) the Agilent VEE Pro 8.5 program automatically sets the voltage output back to 5 V to prepare the system for the next test. The setup allowed for flexibility in testing so that pure electrical characterization testing (Section 3.3.3) was accomplished by disconnecting the impact tower. Similarly, impact characterization testing (Section 3.1) was achieved by omitting the steps related to the current pulse generator. This flexibility allowed the user to gather unbiased electrical and impact data prior to conducting coordinated electrical-impact testing in order to elucidate the effects of electro-mechanical coupling.

Table 3. 5. List of Layup Sequences, Specimen Labels, Final Dimensions, and Cutting Method for all Electrified-Impact Characterization Specimens

Specimen Type	Qty	Specimen ID #’s	t [mm]	L [mm]	w [mm]	s [mm]	s <sub>L</sub> [mm]	Cut Method
IM7/977-3 [0] <sub>32</sub> T	5	32-U-13,...,17	4.23	152.4	152.4	--	--	Table Saw
IM7/977-2 [0/90] <sub>4</sub> S	3	16-X-13,...,15	2.30	152.4	152.4	--	--	Table Saw
CF <sub>16</sub>	2	16-U-0BP-11,12	2.15	152.4	152.4	--	--	CNC Water-Jet
CF <sub>2</sub> /[BP/CF <sub>4</sub> ] <sub>3</sub> /BP/CF <sub>2</sub>	2	16-U-4BP-11,12	2.23	152.4	152.4	--	--	CNC Water-Jet
[CF <sub>2</sub> /BP] <sub>7</sub> /CF <sub>2</sub>	2	16-U-7BP-11,12	2.35	152.4	152.4	--	--	CNC Water-Jet

### 3.5 Computerized Tomography Imaging

In order to illuminate the interior microstructure of the composite laminates, CT scans were performed on CFRP/BP specimens in Table 3. 6., courtesy of Schneider Electric in Cedar Rapids, IA. The CT scans were performed using a Zeiss METROTOM 1500 computed tomography (CT) system. The METROTOM 1500 utilizes an x-ray emitter that emanates a conical imaging beam. An x-ray detector records and digitizes the x-ray intensity after the beam has passed through the specimen. The specimen, placed between the emitter and detector, rotated on a turntable through a full 361° during the scan. The location of the turntable can be adjusted closer or farther from the x-ray emitter, depending on the specimen size. A small specimen placed close to the emitter is magnified greater on the receiver and results in better scan resolution. The METROTOM 1500 can produce voxel (volumetric pixel) resolutions ranging from 5 μm to 400 μm and can scan objects as large as a 300 mm by 300 mm cylinder [50]. For the CFRP/BP specimens, the BP layers were estimated to be between 10-25 μm in thickness per layer. In general, the resolution of the scan is up to 1/1000 the length of the specimen. In order to capture the detail of the BP layers, the specimens were cut to 10mm in length in order to achieve an approximate resolution of 10 μm. The CT scans were reconstructed into 3D image stacks using VGStudio MAX by the CT Analyst at Schneider Electric and further processed using myVGL Viewer by the author of the current work.



Table 3. 6. List of Layup Sequences, Specimen Labels, Final Dimensions, and Cutting Method for all CT Imaging Specimens

Specimen Type	Qty	Specimen ID #’s	t [mm]	L [mm]	w [mm]	s [mm]	s <sub>L</sub> [mm]	Cut Method
CF <sub>16</sub>	1	16-U-0BP-13	2.15	10.0	10.0	--	--	Cutting Wheel
CF <sub>2</sub> /[BP/CF <sub>4</sub> ] <sub>3</sub> /BP/CF <sub>2</sub>	1	16-U-4BP-13	2.23	10.0	10.0	--	--	Cutting Wheel
[CF <sub>2</sub> /BP] <sub>7</sub> /CF <sub>2</sub>	1	16-U-7BP-13	2.35	10.0	10.0	--	--	Cutting Wheel

### 3.6 Experimental Methods: Summary

The CFRP specimens in the current thesis were of the following types: 16-ply unidirectional (16-U), 32-ply unidirectional (32-U), 16-ply cross-ply (16-X), 32-ply cross-ply (32-X), 16-ply quasi-isotropic (16-Q), 32-ply quasi-isotropic (32-Q), and 16-ply unidirectional specimens with 0, 4, and 7 layers of carbon nanotube buckypaper (16-U-0BP, 16-U-4BP, and 16-U-7BP). Low-velocity impact characterization experiments were carried out using an Instron Dynatup 8200 impact tower. The impact energy was selected such that only barely visible impact damage was induced in the specimens. The peak impact loads from the experimental data were recorded and used in development of quasi-static impact models in Chapter 6.

Next, electrical response was characterized using a traditional line-type 4-probe method as well as a newly developed point-type 4-probe method. The point-type 4-probe method utilized a handheld probe device compared to the epoxy-fixed electrodes used in the line-type 4-probe method. Previously, this new point-type 4-probe method had never been applied to electrically anisotropic materials. This method offers a potentially less invasive measurement technique, which could potentially be used in the field for non-destructive electrical resistance measurements. Using the electrical resistance

measurements and an analytical model, a new method was developed for recovering the electrically anisotropic electrical resistivities for each specimen using measurements from the line-type 4-probe method. These recovered properties were then used in the electrical FE models of chapters 5 and 6. Next, select specimens were subjected to simultaneous application of low-velocity impact and high-intensity current pulse in order to observe the effects of electro-mechanical coupling. Finally, CT scans were performed on CFRP/BP specimens in order to better understand the local microstructure, including the distribution of manufacturing defects.

## CHAPTER 4: EXPERIMENTAL AND ANALYTICAL CHARACTERIZATION OF ELECTRICAL & IMPACT RESPONSE

The objectives of the electrical and impact characterization work included: (i) expand upon previous analytical models for electrically anisotropic materials and apply them to line-type and point-type 4-probe methods (Section 4.1), (ii) leverage the concept of effective thickness to develop electrical FE models for line-type and point-type 4-probe methods (Section 4.2), (iii) compare experimental and FE results for line-type (Section 4.3) and point-type (Section 4.4) 4-probe methods, (iv) compare the advantages and disadvantages of the line-type and point-type 4-probe methods (Section 4.5), (v) develop a method for identifying optimal electrical properties based on material thickness (Section 4.6), (vi) observe specimen response to 2-probe high-intensity current pulse (Section 4.7), and (vii) observe the influence of the high-intensity current pulse on impact response (Section 4.8). In order to apply the 4-probe analytical models of Busch et al. [16] to the methods of the current study, additional mathematical manipulation was necessary.

### 4.1 Mathematical Electrical Models

In the Literature Review in Chapter 2.2, a mathematical model of the voltage distribution for a line-type 4-probe specimen (Figure 2. 3.) was presented in equations (2. 1) - (2. 9). In the current work, the model is extended enabling interpretation of the electrical resistance results for fiber-reinforced laminates of different layup and thickness. The following mathematical discussion is an original contribution of the current work. Through experimental study Busch et. al. found that for electrically anisotropic materials,

the current density was exponentially damped within a thin surface layer, which was defined by an effective depth of current penetration in equation (2. 9). This concept of effective conducting depth provides valuable physical insight into the behavior of electric current within CFRP specimens. For instance, if equation (2. 9) is substituted into equation (2. 7), the resistivity in the fiber direction  $\rho_x$  can be solved for as a function of  $z_{eff}$ :

$$\rho_x \approx \frac{R_{top}bz_{eff}}{s} \quad (4. 1)$$

This expression in (4. 1) is a novel contribution of the current thesis work and lends tremendous physical insight. The term  $z_{eff}$  introduced into the equation describes the depth of current penetration into the thickness of the composite specimen and is not dependent on the overall thickness of the specimen. Furthermore, the equation (4. 1) for the fiber direction resistivity compares term for term to the resistivity equation for isotropic materials:

$$\rho = \frac{RA}{L} \quad (4. 2)$$

where  $R$  is the experimental resistance,  $A$  is the cross-sectional area, and  $L$  is the length of the specimen between the measurement probes. When comparing (4. 2) for isotropic and (4. 1) for anisotropic materials, the area term  $A$  has been replaced by the term  $bz_{eff}$ , which describes the effective cross-sectional area. In addition, the length  $L$  has been replaced by the electrode spacing  $s$ .

For CFRP specimens, the resistivity ratio  $\rho_x/\rho_z$  is generally very small, which results in a very shallow depth of current penetration  $z_{eff}$ . If the resistivity ratio  $\rho_x/\rho_z$  is relatively large, the calculated depth of current penetration may actually be larger than the physical thickness of the specimen. Therefore, in the current work the depth of current penetration was defined as the minimum of  $z_{eff}$  and the physical specimen thickness  $t$ :

$$t_{eff} = \min(z_{eff}, t), \quad (4.3)$$

The term  $t_{eff}$  will be referred to as the effective conducting thickness of the current-carrying specimen, and the updated fiber-direction resistivity becomes:

$$\rho_x \approx \frac{R_{top} b t_{eff}}{s} \quad (4.4)$$

Although the preceding formulation was developed for the line-type 4-probe method, similar concepts were applied to the point-type 4-probe method in order to enable the use of the JIS K7194 methods on anisotropic materials.

The JIS K7194 methods [61] were developed to be used for determining the resistivity of conductive plastics with isotropic electrical properties. The JIS K7194 standard gives the calculation of the specimen resistivity as

$$\rho = F(w, t) t R \quad (4.5)$$

Where  $\rho$  is the resistivity (Ohm-cm),  $t$  is the thickness (cm),  $R$  is the resistance (Ohm), and  $F(w,t)$  is a dimensionless correction factor that correlates with the thickness and width,  $w$  (cm), of the specimen. In the JIS K7194 standard,  $F$  is given in tabular form as a function of the specimen thickness. The full mathematical equation for determining  $F$  is given in the Appendix in equation (A. 1). In order to use the JIS K7194 methods on electrically anisotropic CFRP specimens, the concept of effective depth of current penetration was employed. This constitutes another contribution of the current work. The following mathematical formulation and subsequent results for the point-type 4-probe method can be characterized as a “modified JIS method.”

Similar to the line-type 4-probe method, the thickness in (4. 5) needed to be replaced by the effective thickness. In the current work, the effective thickness was calculated using the material properties from the line-type 4-probe method, since the JIS method did not allow for bottom resistance measurements. Contrary to the previous line-type 4-probe method, the current electrodes did not span the entire width of the specimen, so the correction factor  $\square(\square,t)$  was adjusted for the effective width denoted by  $w_{eff}$ . In the JIS K7194 standard, the correction factor  $F$  is provided in tabular form for a specimen with dimensions 8 cm x 5 cm x  $t$ . In (4. 6), the standard correction factor has been replaced by an effective correction factor  $F_{eff}$ . This effective correction factor is an approximation for the exact correction factor given in equation (A. 1) in the Appendix. The exact correction was derived in the current study for the 16-U specimens using (A. 1) and the difference between the  $F_{eff}$  in (4. 9) and exact correction factor in (A. 1) was only 3.7%. The term  $y_{eff}$  comes from the assumption that the current density was exponentially

damped in the y-direction, similar to the assumption in the z-direction for  $t_{eff}$ , discussed previously. Replacing  $t$  by  $t_{eff}$  and  $w$  with  $w_{eff}$  in the resistivity equation leads to:

$$\rho_x \approx F_{eff} t_{eff} R \quad (4.6)$$

$$w_{eff} \approx w_{electrode} + 2 * y_{eff} \quad (4.7)$$

$$y_{eff} \approx \frac{L}{\pi} \left( \frac{\rho_x}{\rho_y} \right)^{\frac{1}{2}} \quad (4.8)$$

$$F_{eff} \approx F(w, t_{eff}) \frac{w_{eff}}{w} \quad (4.9)$$

The effective dimensions in (4.7) and (4.8) require the ratios  $\rho_x / \rho_y$  and  $\rho_x / \rho_z$ . For the point-type 4-probe method, however, the electrodes only measure a voltage drop on the top surface of the specimen and do not capture the through-thickness effects. For this reason, the electrical resistivities could not be recovered directly from this single experimental measurement. However, in the current work, data history for  $\rho_x / \rho_y$  and  $\rho_x / \rho_z$  was available from the line-type 4-probe experiments, so these ratios could be calculated for the given specimens and inserted into the above equations. Since this point-type 4-probe method uses approximations of the ratios  $\rho_x / \rho_y$  and  $\rho_x / \rho_z$ , the values calculated from equation (4.6) is only an approximation of the fiber direction resistivity  $\rho_x$ . Electrical resistivity values  $\rho_x$  were recovered using equations (4.6) - (4.8) for all

unidirectional specimens (16-U, 32-U, 16-U-0BP, 16-U-4BP, 16-U-7BP) and are listed in Table 3. 3.

#### 4.2 Development of Finite Element Electrical Models

Finite element (FE) models were generated for each specimen type tested using the line-type and point-type 4-probe methods. The purpose of the FE models was to verify the methods for recovering experimental electrical properties and to develop predictive capabilities for CFRP laminates with varying thickness and layup. Models were initially developed using the COMSOL software package for basic electrical simulations. The models were then replicated in ABAQUS for the damage sensing feasibility study in Chapter 5. Table 4. 1. lists a summary of FE model dimensions and parameters for all 4-probe models in the current study, and Table 4. 2. lists the electrical properties used in the FE models for each specimen type in the current study. For the specimens 16-U-4BP and 16-U-7BP, in the original models, the initial objective was to model the layers of BP and CF separately. These CFRP/BP specimens were provided as laminated plates, so it was not possible to analyze the electrical response of the BP layers separately from the rest of the laminate. Without the ability to measure the experimental resistivity of the BP layers, it was not possible to accurately develop a material model for the BP layers in the FE models. Moreover, the BP layers were manufactured in small batches hand, which meant that the properties could not be estimated based on data in literature. For these reasons, the 16-U-4BP and 16-U-7BP specimens were modeled as bulk orthotropic materials with no distinction between the BP and CF layers. The



material properties applied to these models were recovered for each specimen using the line-type 4-probe method.

Table 4. 1. FE Model Parameters and Effective Dimensions

		Standard 6-Probe Method		JIS 4-Probe Method			
		Line of Electrodes in Fiber Direction	Line of Electrodes Transverse to Fiber Direction	Line of Electrodes in Fiber Direction		Line of Electrodes Transverse to Fiber Direction	
Specimen Type	Current [A]	$t_{eff}$ [mm]	t or $t_{eff}$ [mm]	$t_{eff}$ [mm]	$w_{el}+2w_{eff}$ [mm]	t or $t_{eff}$ [mm]	w [mm]
16-U	0.01	0.075	2.31	0.088	1.22	2.31	50
32-U	0.01	0.075	4.23	0.088	1.22	4.23	50
16-X	0.01	0.075	0.219	0.088	1.22	0.232	50
16-Q	0.01	N/A	2.25	N/A	N/A	N/A	N/A
32-Q	0.01	N/A	4.50	N/A	N/A	N/A	N/A
16-U-0BP	0.01	0.34	2.15	0.179	1.40	N/A	N/A
16-U-4BP	0.01	1.73	2.23	0.907	6.60	N/A	N/A
16-U-7BP	0.01	1.85	2.35	1.097	7.82	N/A	N/A

Table 4. 2. Material Properties Used in FE Models

Specimen Type	$\sigma_x$ [S/m]	$\rho_x$ [Ohm-cm]	$\sigma_y$ [S/m]	$\rho_y$ [Ohm-cm]	$\sigma_z$ [S/m]	$\rho_z$ [Ohm-cm]
16-U	29330	0.0034	1.61	62.3	0.287	348.4
32-U	29330	0.0034	1.61	62.3	0.287	348.4
16-X	29330	0.0034	1.61	62.3	0.287	348.4
16-Q	36177	0.000028	36.2	0.0276	7.24	0.138
32-Q	36177	0.000028	36.2	0.0276	7.24	0.138
16-U-0BP	10993	0.0091	1.51	66.2	0.539	185
16-U-4BP	5185	0.0193	67.24	1.487	6.59	15.2
16-U-7BP	8533	0.0117	162.34	0.616	15.917	6.3

#### 4.2.1 Significance of Effective Thickness in FE Models

In the current thesis, the concepts of effective thickness (4. 3) and effective width (4. 7) were leveraged when building the geometry of the FE models. As discussed in the Literature Review in Section 2.3, some previous FE models of the 4-probe experimental setup were not able to accurately predict the electrical resistance of CFRP specimens that had a high-degree of electrical anisotropy [13]. The author of the current thesis found that the use of effective thickness was a critical factor in achieving accurate numerical results. The rationale in using effective dimensions was that the analytical model by Busch et al. found that when electrodes were placed on the top surface of an electrically anisotropic specimen, the current density was exponentially damped through the thickness and confined within a thin surface layer, or effective thickness. The linear current-voltage response (Ohmic response) was confined to this effective thickness. The analytical model of Busch et al. only considered the linear response. At very small voltage measurements, however, non-linear response was observed [16]. Therefore, in order to keep the newly developed FE models consistent with the Ohmic model of Busch, the linear current-voltage response in the CFRP specimens was assumed to be contained within the effective thickness (and effective width for point-type method). The geometry below the effective thickness (or beyond the effective width) was assumed to have non-linear response and disregarded from the model. Due to the complexity introduced by the effective dimensions, the FE models needed to be developed systematically for each specimen configuration and for each electrode orientation.

#### 4.2.2 FE Models: Line-Type 4-Probe Method with Line of Electrodes Aligned with Fiber Direction

In the line-type 4-probe method, the electrodes spanned the full width of the specimen, (see Figure 2. 3). For line-type 4-probe specimens with the electrode wires running transverse to the fiber direction ( $y$  – direction), the line of electrodes was said to align with the fiber direction. The conductivity in the fiber direction ( $x$  – direction) was much higher than the through thickness direction ( $z$  – direction), therefore the effective thickness  $t_{\text{eff}}$  was calculated to be less than the physical thickness of the specimens. Since the analytical model [16] did not consider any non-linear voltage current behavior that occurred below the effective thickness, the FE model, which also only considered linear behavior, negated the volume of the composite below the effective thickness. The corresponding FE geometry was modeled with the effective dimensions ( $L \times w \times t_{\text{eff}}$ ). In COMSOL, the specimen and current source electrodes were modeled using quadrilateral elements calibrated for general physics. An electrical insulation condition was specified on the specimen, and current conservation was applied to the entire model. The electrode material was an isotropic homogenous material and was assigned the conductivity of copper ( $5.96 \text{ E}7 \text{ S/m}$ ). The carbon fiber-reinforced composite material was created as an orthotropic homogeneous material and was assigned directional anisotropic properties given in Table 4. 2. The current density was applied as a positive source at the left electrode and a negative source at the right electrode, in reference to the configuration of Figure 2. 3. (c). The voltage drop between the sensing electrodes was measured using the internal probe functions in COMSOL. Top resistance measurements were calculated by dividing the measured voltage by applied current.

An important item of note was that for some specimen types (16-U, 32-U, 16-X), the effective thickness  $t_{\text{eff}}$  was less than the thickness of a single ply. In this case, the current did not even penetrate through the full thickness of the first ply, therefore the FE models for 16-U, 32-U, and 16-X specimens were identical (i.e. no difference for different thickness or stacking sequence). In the FE models, the properties applied to the 32-U and 16-X models were taken from the properties recovered from experiments for the 16-U model. This was done to validate the predictive capabilities of the models, so that the properties calculated for a given thickness could be used to predict or validate experiments on specimens of a different thickness or layup. The next step was to develop FE models with electrodes rotated 90°.

#### 4.2.3 FE Models: Line-Type 4-Probe Method with Line of Electrodes Transverse to Fiber Direction

For specimens with electrode wires oriented with the top-ply fiber direction (x – direction), the line of electrodes was transverse to the fiber direction. Since the properties in the y and z – directions were of similar magnitude in the current study, for unidirectional specimens, the effective thickness of the specimen was equal to the full physical thickness of the specimen by equations (2. 9) and (4. 3). Therefore in COMSOL, the full specimen dimensions and current source electrodes were modeled using quadrilateral elements calibrated for general physics. Top resistance measurements were calculated by dividing the measured voltage by applied current. It is noteworthy that the material properties recovered experimentally from the 16-ply specimens were used in the finite element models for both 16-ply and 32-ply specimens. This was done to

demonstrate once again that the FE models could be used to predict response in specimens with varying thickness. For cross-ply FE models, a more complex multi-layer model was required.

For the 16-X specimens, portions of the previously discussed models were combined to generate the cross-ply model. As discussed above, for unidirectional specimens with the line of electrodes transverse to the fiber direction, the current penetrated through the full thickness of the specimen. In the cross-ply specimens, however, the plies alternated by 90 °. This resulted in the current flowing through the entire thickness of the top ply but damped through the effective thickness of the next ply where the current flowed in the fiber direction. For this reason, the cross-ply specimens were represented in the FE model by a two-layer structure, where the top layer had a thickness of the single ply of the composite laminate and the thickness of the second layer was equal to the effective thickness. Therefore, the resulting dimensions of the FE model were  $(L \times w \times t/16 + t_{\text{eff}})$ . Between the two layers, a contact resistance (surface impedance) was applied as  $2.9 \times 10^{-5} \Omega\text{m}^2$  [63]. This modeling was quite straightforward taking advantage of the fact that the effective thickness for current in the fiber direction was less than the thickness of a single ply of the laminate. Had the effective thickness been greater than a single ply thickness, additional layers would have needed to be included in the model. While the top resistance measurement is often convenient for use, this measurement plane is limited in capturing through-thickness effects. In order to better characterize the through-thickness electrical response, the oblique measurement plane is useful.

#### 4.2.4 FE Models: Oblique Measurement Plane Using Line- Type 4-Probe Method

In order to further extend the methods and FE models of the current thesis to specimens with additional layup arrangements, experimental data was obtained from work by McAndrew and Zhupanska [17,18]. In this work, 4-probe electrical measurements and low-velocity impact data was gathered for AS4/3501-6 quasi-isotropic specimens with layup arrangements of  $[0/45/-45/90]_{2S}$  and  $[0/45/-45/90]_{4S}$ . These specimens were square plates with dimensions of 152.4 x 152.4 x 2.25 mm and 152.4 x 152.4 x 4.5mm, respectively. The electrodes were placed with a spacing of 30mm and were symmetric to the centerline of the specimen. In this study, there were no unidirectional specimens tested, so it was not possible to recover the orthotropic electrical resistivities in the manner discussed previously for 16-U and 32-U specimens. In order to develop electrical FE models, the material properties for the AS4/3501-6 quasi-isotropic specimens were calculated from available material datasheet properties and theory referred to as the rule of mixtures. In the local coordinate system, the x-direction corresponds to the fiber-direction, the y-direction is transverse to fiber direction in-plane, and the z-direction corresponds to the through-thickness direction. Based on the rule of mixtures, the theoretical fiber-direction electrical conductivity is given as:

$$\sigma_x = v_f \sigma_f + (1 - v_f) \sigma_m \quad (4.10)$$

where  $v_f$  is fiber volume fraction,  $\sigma_f$  is the electrical conductivity of fibers (S/m), and  $\sigma_m$  is the electrical conductivity of matrix (S/m), For an electrically insulating epoxy matrix  $\sigma_m \approx 0$  resulting in:

$$\sigma_x \approx v_f \sigma_f \quad (4.11)$$

From previous literature [13–15], the conductivity in the y-direction is typically assumed to be 3 orders of magnitude less than conductivity in the fiber direction. When stacked into a laminate, the through thickness conductivity is typically 3-4 orders of magnitude less than conductivity in the fiber direction.

From the AS4/3501-6 datasheets [54,64], the electrical resistivity of the AS4 fiber is typically  $1.7 \times 10^{-3}$  Ohm-cm, which corresponds to electrical conductivity of 58,800 S/m. Assuming a fiber volume fraction of 62.5%, x-direction electrical conductivity was calculated as 36,177 S/m . Scaling fiber-direction conductivity by  $10^{-3}$  and  $2 \times 10^{-4}$  for the y and z-directions, respectively yields the material properties in Table 4. 2.

In the case of the quasi-isotropic 16-Q and 32-Q specimens, the fibers in the +45 and -45 plies did not coincide with the axes in the global coordinate system for the line-type 4-probe experimental setup. Relative to the global coordinate system, the electrical properties in these plies were considered generally anisotropic (i.e. not orthotropic which was the case in 0 and 90 plies). In order to build the FE models, the electrical properties needed to be converted from the local coordinate system to the global coordinate system. For a generally anisotropic material, electrical conductivity in the global coordinate system is given as:

$$\boldsymbol{\sigma} = \begin{bmatrix} \sigma_{xx} & \sigma_{xy} & \sigma_{xz} \\ \sigma_{xy} & \sigma_{yy} & \sigma_{yz} \\ \sigma_{xz} & \sigma_{yz} & \sigma_{zz} \end{bmatrix} \quad (4.12)$$

In the case of a fiber-reinforced composite it is assumed that there is no coupling between neither the x-z directions nor y-z directions, thus  $\sigma_{xz}^{(i)} = \sigma_{yz}^{(i)} = 0$ . Therefore within a composite laminate, the conductivity for a single ply  $i$  in the laminate (global) coordinate system is given by:

$$\boldsymbol{\sigma}^{(i)} = \begin{bmatrix} \sigma_{xx}^{(i)} & \sigma_{xy}^{(i)} & 0 \\ \sigma_{xy}^{(i)} & \sigma_{yy}^{(i)} & 0 \\ 0 & 0 & \sigma_{zz}^{(i)} \end{bmatrix} \quad (4.13)$$

$$\sigma_{xx}^{(i)} = \sigma_x^{(i)} \cos^2 \theta + \sigma_y^{(i)} \sin^2 \theta \quad (4.14)$$

$$\sigma_{yy}^{(i)} = \sigma_y^{(i)} \cos^2 \theta + \sigma_x^{(i)} \sin^2 \theta \quad (4.15)$$

$$\sigma_{xy}^{(i)} = (\sigma_x^{(i)} - \sigma_y^{(i)}) \sin \theta \cos \theta \quad (4.16)$$

$$\sigma_{zz}^{(i)} = \sigma_z^{(i)} \quad (4.17)$$

Using the orthotropic properties in Table 4. 2. and equations (4. 14) - (4. 17), the individual lamina properties were calculated for the plies of the AS4/3501-6 quasi-isotropic specimens as listed in Table 4.3.



Table 4. 3. Electrical Conductivity by Fiber Angle for 16-Q and 32-Q Specimens

Fiber Angle [°]	$\sigma_{xx}$ [S/m]	$\sigma_{yy}$ [S/m] [Ohm-cm]	$\sigma_{xy}$ [S/m]	$\sigma_{zz}$ [S/m] [Ohm-cm]	$\sigma_{xz}$ [S/m]	$\sigma_{yz}$ [S/m] [Ohm-cm]
0	36177	36.2	0	7.24	0	0
90	36.2	36177	0	7.24	0	0
45	18106	18106	18070	7.24	0	0
-45	18106	18106	-18070	7.24	0	0

When building the top resistance FE model for the 16-Q and 32-Q specimens, the lessons learned from the cross-ply model were leveraged. As with the cross-ply model, the effective thickness of each individual layer was analyzed to determine if the current would penetrate through the ply. In the case of the quasi-isotropic specimens, the effective thickness was calculated using the properties in Table 4.3. and the following equation:

$$t_{eff} = \frac{L}{\pi} \left( \frac{\rho_{xx}}{\rho_{zz}} \right)^{\frac{1}{2}} \quad (4. 18)$$

The effective thickness was calculated using the properties for each ply in the quasi-isotropic specimens, and for every ply, the effective thickness was greater than the thickness of the individual ply. Therefore, in the electrical FE model, all plies were included. In the experimental work by McAndrew, the electrodes were placed such that the line of electrodes was transverse to the fiber direction of the top (and bottom) plies. In this configuration, the stacking sequences were effectively [90/-45/45/0]<sub>2S</sub> and [90/-45/45/0]<sub>4S</sub>. In addition to a top resistance measurement, McAndrew also included an oblique resistance measurement. In order to add this additional measurement plane to the FE model, additional source electrodes were placed on the bottom surface of the specimen directly below the top surface electrodes. For the FE simulations for oblique

resistance measurement, the only modifications required to the model were to change the locations of the negative current source and sensing locations from the top to bottom surface, as shown in Figure 4. 1. In addition to the concept of effective thickness employed in the line-type methods, for the point-type 4-probe models, the concept of effective width was employed.

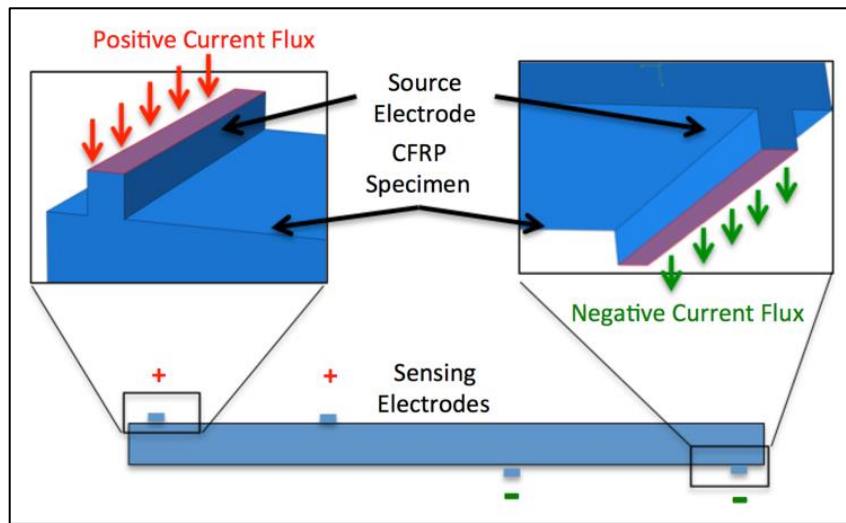


Figure 4. 1. Current source and sensing locations for oblique measurement plane.

#### 4.2.5 FE Models: Point-Type 4-Probe Method

For the FE models of point-type 4-probe tests, experience gained from the models for the line-type method was used and expanded upon. The primary difference between the point-type models and previous line-type FE models was that in the point-type tests, the electrodes contacted the specimen at localized points and did not span the entire width of the specimen. The 0.8mm electrodes were modeled and attached to the top of the specimen at the “1” position according to Figure 3. 6. Contrary to the experimental

measurement the FE model did not take into account the positional effects of the electrodes so this location was sufficient for comparing to the average experimental resistance. As discussed in Section 4.2.3, when the line of electrodes was transverse to fiber direction in the top ply, the current penetrated through the full thickness of the specimen. Therefore for these simulations, the full plate dimensions were modeled. Conversely, when the line of electrodes was oriented with the fiber direction in the top ply, the current occupied only the top effective thickness, and the material outside of this zone was excluded from the model. This assumption was also used when modeling the material beyond the width of the electrode, thus the same exponential damping was assumed in the positive and negative y-directions. The FE model dimensions for the point-type 4-probe tests were therefore ( $L \times w_{\text{eff}} \times t_{\text{eff}}$ ). Similar to the line-type 4-probe simulations, cross-ply laminates were represented in the FE model by a two-layer structure, where the top layer had a thickness of the single ply of the laminate and the thickness of the second layer was equivalent to the effective thickness. The resulting dimensions of these FE models were ( $L \times w \times t/16 + t_{\text{eff}}$ ). Between the two plies, a contact resistance (surface impedance) was applied as  $2.9 \times 10^{-5} \text{ } \Omega\text{m}^2$  [63].

#### 4.2.6 FE Models: Summary of Methods

The application of effective specimen dimensions in the FE models of the current study were unique in comparison to previous literature, and these unique methods were found to be critical in the accurate simulation results obtained herein. The concepts could be generalized for greater applications than the specimen types and stacking sequences tested in the current work. The following findings were unique to the methods of the

current thesis and could provide guidance for development of models in the future. Generally, if: (i) the line of electrodes was oriented with direction of fibers in the top ply and (ii) the effective thickness was less than the thickness of the top ply, then unidirectional and cross-ply FE models were identical, as was the case for specimens 16-U, 32-U, and 16-X. Moreover, for specimens with alternating stacking sequence, the effective thickness of each layer needed to be analyzed from top to bottom to determine if the current would penetrate through the full layer thickness. If the effective thickness was greater than a single layer thickness, then a multi-layer model was needed to properly simulate the flow of current through the specimen. Although the FE models in the current work were primarily used to validate experimental data, in Section 4.6, the FE models were used to target optimized electrical properties based on material thickness.

#### 4.3 Line-Type 4-Probe Method: Results

Electrical characterization tests were performed using the line-type 4-probe method, and the results are summarized in Table 4. 4. The results discussed in this section were average results for all specimens of a specific layup arrangement (See Table 3. 2). For example, the results for 16-U specimens with the line of electrodes transverse to fiber direction were the average results for specimens 16-U-1, 16-U-2, and 16-U-3. On the other hand, the results for 16-U specimens with the line of electrodes oriented with fiber direction were the average results for specimens 16-U-4, 16-U-5, and 16-U-6. Upon a cursory review of the results, the experimental top resistance measurements and FE simulations correlated very well for all specimens. As discussed previously, the electrical resistivity values recovered from the 16-U specimens were used in building the FE models for specimens with varying thickness and layup (32-U, 16-X, 16-Q, and 32-Q) in

order to show the predictive capabilities of the models. Therefore the lowest error was observed for the 16-U specimens, where experimental and FE measurements differed by only 1.6% and 0.8% for resistance measurements with the line of electrodes in fiber-direction and transverse to fiber-direction, respectively. These errors were considered acceptable due to the known sensitivity of experimental results on specimen preparation (i.e.: sanding of surface and application of silver paint). These results validated the method of recovering the electrical resistivity properties as well as the FE models.

Table 4. 4. Experimental and FE Results Using Line-Type 4-Probe Method

Specimen Type	Line of Electrodes in Fiber Direction (x-direction)			Line of Electrodes Transverse to Fiber Direction (y-direction)		
	Exper. $R_{top}$ [Ohm]	FE Model $R_{top}$ [Ohm]	% diff	Exper. $R_{top}$ [Ohm]	FE Model $R_{top}$ [Ohm]	% diff
16-U	0.334	0.3394	1.60%	199.5	201.0	0.80%
32-U	0.336	0.3394	1.00%	137.1	121.2	-11.60%
16-X	0.325	0.3394	4.20%	0.357	0.340	-4.60%
16-U-0BP	0.2047	0.212	3.50%	223.2	221.8	-0.60%
16-U-4BP	0.0892	0.088	-1.20%	5.416	5.40	-1.20%
16-U-7BP	0.0447	0.047	5.40%	2.243	2.10	-5.00%

The largest error between experimental and FE resistance was 11.6% for the 32-U specimens with the line of electrodes transverse to fiber-direction. This measurement was considered anomalous, since for the 32-U specimens with the line of electrodes oriented with fiber direction, the discrepancy was only 1.0%. This incongruity can be attributed to specimen preparation, which is highly sensitive to surface treatment (i.e.: sanding of the

surface and application of the silver paint). Another notable remark was that for the 16-X specimens, the FE top resistance differed from the experimental results by only 4.2% for specimens with the line of electrodes oriented with the fiber-direction of top ply and 4.6% for specimens with the line of electrodes oriented transverse to fiber-direction of the top ply. These results demonstrate the true power of the newly developed procedure for measuring and calculating directional properties: the results from one specimen can be used to model and predict results for a specimen with different thickness or layup. The specimens 16-U-0BP, 16-U-4BP, and 16-U-7BP were manufactured in hand-layup process, so the bulk electrical properties recovered from the line-type 4-probe measurements for each individual specimen were applied to each unique FE model.

For the abovementioned specimens, the best correlation between experimental and FE simulations was for specimens 16-U-0BP, where the difference in top resistance was only 0.6%. The largest error observed for specimens 16-U-7BP at 5.4%. For all of these tests, the error was again considered to be acceptable due to the known sensitivity of experimental results on specimen preparation. A significant takeaway of this study was that the addition of layers of BP caused the top resistance of the specimen to decrease considerably. This indicated that the current not only flowed through the top CF layers but also penetrated through the thickness of the specimen and flowed through the highly conductive BP layers. When moving from 0 to 4 layers of BP, the top resistance measurement was 1 to 2 orders of magnitude less in the specimens with 4 layers of BP compared to the control specimens with 0 layers. This significant change in resistance was attributed to the BP layers having conductivity several orders of magnitude greater than the CF layers. When increasing the BP count from 4 layers to 7 layers, the resistance

decreased by 50% in the fiber direction and 59% perpendicular to the fiber direction. This trend was greater than anticipated when comparing to simple resistors in parallel model. Using this approximation, when increasing from 4 to 7 layers of BP, the resistance should only decrease by a maximum of  $3/7$  or 43%. A possible explanation for the gap was nonlinear edge effects, which generally occur when the sensing electrodes are very close to the edges of the specimen. In the semiconductor industry, resistance measurements are taken away from the edges of the specimen to mitigate this effect. This motivated the exploration of the point-type 4-probe method (discussed in Section 4.4) as a viable method for reducing the possible influence of edge effects on the measurement data. In order to further visualize the trends in top resistance, box-plots were generated for each specimen with the line of electrodes oriented with fiber direction in Figure 4. 2.

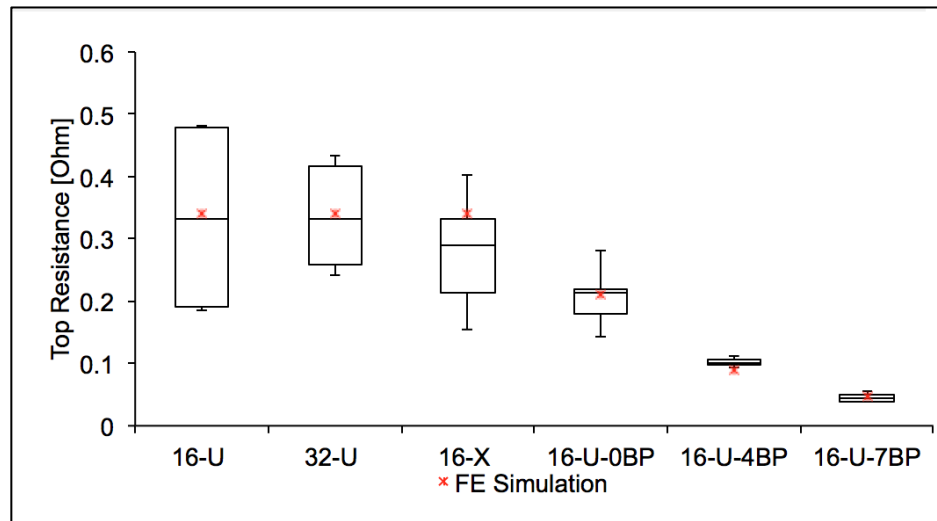


Figure 4. 2. Box plots of top resistance measurement for line-type 4-probe specimens with electrodes aligned with fiber direction of top ply.

Upon review of Figure 4. 2., the FE simulation results fit within the data spread for all specimens. Moreover, the FE results fell within the interquartile range for all specimens, except 16-X and 16-U-4BP. As discussed in the development of the FE models in Section 4.2 (and Table 4. 1.), the effective thickness was the same for specimens 16-U, 32-U, and 16-X. Therefore the FE models and simulation results, shown in Figure 4. 2., were identical for each of these specimens. Overall, there was no statistical difference between the experimental top resistance for 16-U, 32-U, and 16-X specimens. When comparing the results for the BP specimens, as the number of BP layers increased, the resistance decreased as well. More significantly, the specimens with 4 and 7 layers of BP had very little scatter in the experimental data compared to specimens with no BP. This result suggests that the BP layers may not only reduce the electrical resistance of the specimens but may improve the precision of electrical resistance measurements.

For the quasi-isotropic specimens, the material properties were theoretically derived instead of recovered from experimental data, thus the experimental and FE predictions did not match as closely in Table 4. 5. as they did in Table 4. 4. For instance, the most accurate FE prediction differed from the experimental average by only 3% for the 16-Q oblique resistance, however the poorest discrepancy was 54% for the 32-Q top resistance. There exist two explanations for this large discrepancy between the FE predictions and average experimental results. First, as mentioned previously, the material properties were theoretically derived, which means that they do not match the exact properties of the physical specimens. The second explanation is that there was a broad scatter in the experimental data and a limited number of specimens tested, thus the



average resistance may not accurately represent a larger sample size. For this reason, box plots were also generated for these specimens, as displayed in Figure 4. 3.

Table 4. 5. Experimental and FE Results For Quasi-Isotropic Specimens Using Line-Type 4-Probe Method

Specimen Type	Top Resistance			Oblique Resistance		
	Exper. $R_{top}$ [Ohm]	FE $R_{top}$ [Ohm]	% diff	Exper. $R_{obl}$ [Ohm]	FE $R_{obl}$ [Ohm]	% diff
16-Q	0.0087	0.0066	-25%	0.0109	0.0112	3%
32-Q	0.0142	0.0065	-54%	0.0172	0.0236	27%

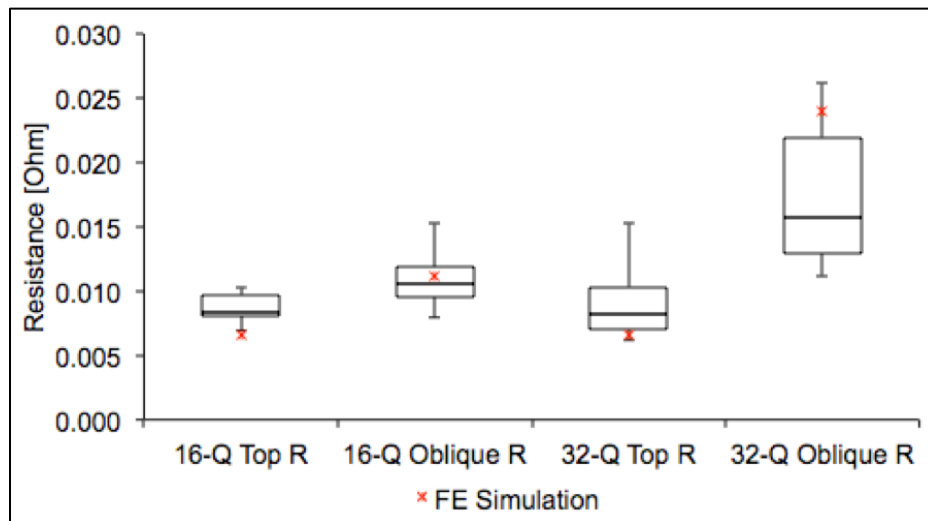


Figure 4. 3. Experimental Resistance Box Plots [17] and FE Simulation Results for 16-ply and 32-ply Quasi-Isotropic Specimens in Top and Oblique Measurement Planes.

In box plot form, the issue of data scatter becomes more readily apparent. For all four sets of data in Figure 4. 3., the FE prediction fell within the data spread, albeit only for the 16-Q oblique resistance did the FE prediction fall within the interquartile range. Considering

the former discussion and the accuracy issues in some of the literature, these results were considered reasonable. While the electrical resistance was readily comparable between experimental and FE simulations, the FE models were able to elucidate phenomena that could not be observed in the experiments.

In order to gain additional insight into the electrical response of the laminated composites using the line-type 4-probe method, 2-D plots of current density and voltage potential were composed and are displayed in Figure 4. 4. (a) – (b) and Figure 4. 5. (a) – (b), respectively. The contour plots in Figure 4. 4. and Figure 4. 5. are shown only in the  $x - z$  plane, because the electrodes spanned the entire width of the specimens, which essentially eliminated variation in the  $y -$  direction. In Figure 4. 4. (a), the current density distribution was plotted for a 16-U specimen with the line of electrodes oriented in the fiber-direction. For this specimen, the current density was most highly concentrated at the top surface of the specimen near the current source electrodes, where as the lowest values for current density were found directly under the source electrodes at the depth of the effective thickness of the specimens. At the outermost edges of the specimen ( $x = \pm L/2$ ), there was a significant gradient in the current density through the thickness of the specimen. At the center of the specimen, however, the current density was much more uniform through the thickness. This result indicated that the greater the specimen length and source electrode spacing, the more uniform the current density distribution in the specimen. In Figure 4. 4. (b), current density contours are displayed for a 16-X specimen with the line of electrodes transverse to the fiber-direction in the top ply.

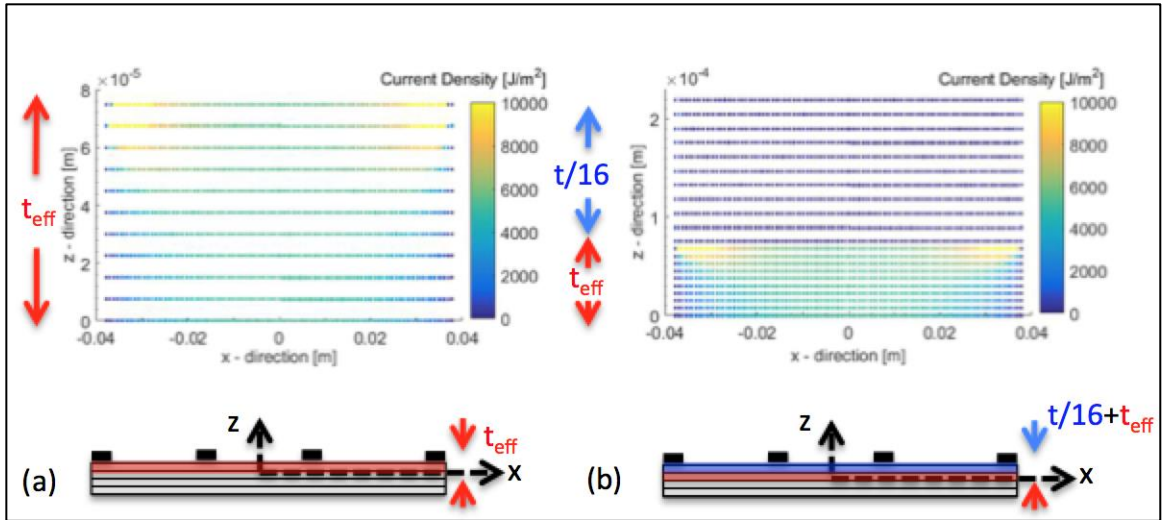


Figure 4. 4. Line-type 4-probe FE simulation plots of current density magnitude in  $x - z$  plane for (a) 16-U specimens with line of electrodes aligned with fiber direction and (b) 16-X specimens with line of electrodes transverse to direction of fibers in top ply.

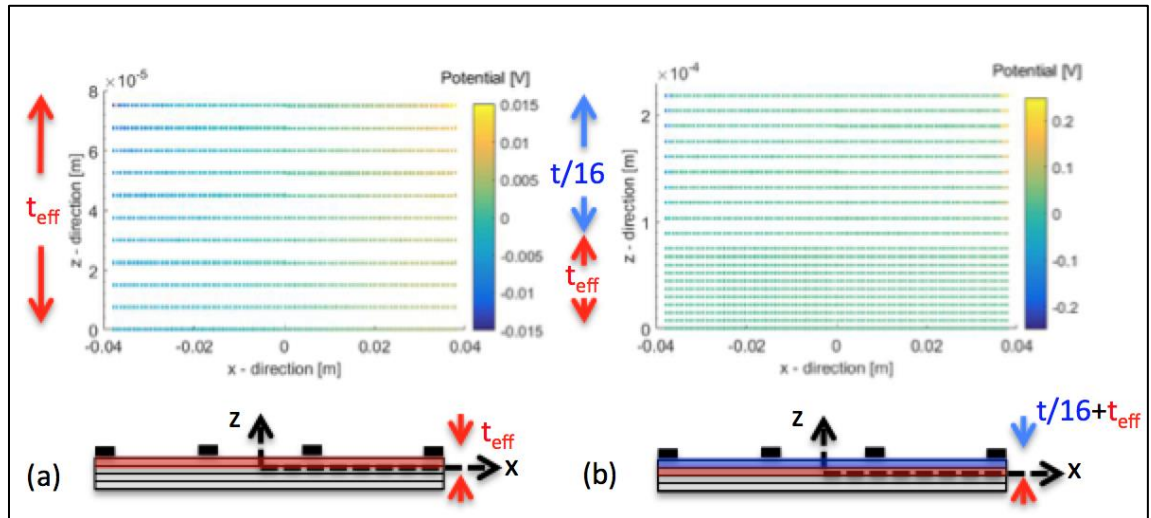


Figure 4. 5. Line-type 4-probe FE simulation plots of voltage distribution in  $x - z$  plane for (a) 16-U specimens with line of electrodes aligned with fiber direction and (b) 16-X specimens with line of electrodes transverse to direction of fibers in top ply.

For the 16-X specimen with the line of electrodes transverse to the fiber-direction in the top ply, the current density in the top ply was very low compared to the current

density in the second ply. This result was significant, because the current essentially flowed straight down in the  $z$  – direction from the electrodes through the top ply before flowing in the  $x$  – direction within the second ply. More significantly, the current density distribution in the second ply of Figure 4. 4. (b) visually resembles that of Figure 4. 4. (a). Additional insight was gained through 2-D contour plots of voltage distribution in Figure 4. 5.

Similar to the current density distribution, the voltage in Figure 4. 5. (a) was damped moderately through the thickness of the 16-U specimen. The voltage was concentrated near the electrodes, but not nearly as much as the current density. Proximal to the center of the specimen ( $x = 0$ ), the voltage distribution was more uniform compared to the outer edges. In Figure 4. 5. (b), on the other hand, the voltage distribution in the 16-X specimen was much more concentrated near the source electrodes compared to the rest of the specimen. Directly below the electrodes, the voltage was close to 0.25 V, whereas the voltage potential in the remainder of the specimen was on the millivolt scale. The voltage potential concentration was further evidence that the current penetrated vertically down through the top ply before flowing horizontally through the second ply. In order to determine the influence of the measurement method on the electrical response, further investigation was performed using the point-type 4-probe method based on the JIS K7194 standard.

#### 4.4 Point-Type 4-Probe Modified JIS Method: Results

Electrical characterization tests were performed using the point-type 4-probe method, and the results are summarized in Table 4. 6. The results discussed in this section

were average results for all specimens of a specific layup arrangement (See Table 3. 2). The error between experimental and FE resistance was 10.5% or less for specimens 16-U and 32-U with the line of electrodes oriented with the fiber-direction. Conversely, for tests performed with the line of electrodes transverse to the fiber-direction in the top ply, the error was significantly higher at 5.7% and 17.4% for the 16-U and 32-U specimens, respectively. This similar trend was found for the line-type 4-probe method above, where the FE models predicted a lower resistance for the 32-U specimens compared to the experimental resistance. It should be noted that for both methods, the properties calculated from the 16-U specimens were applied to the 32-U FE models. When observing the individual specimens, however, there was greater fiber fraying at the edges of the 32-U specimens compared to the 16-U specimens. This fraying was caused by mechanically cutting the specimens perpendicular to the fibers and could have contributed to the elevated experimental resistance measurements compared to the FE models. Comparing the results for the 16-X specimens, the FE models predicted resistances that were 15.2% and 12.8% greater than the empirical results. For the 16-U-0BP, 16-U-4BP, and 16-U-7BP specimens with various layers of BP, there were additional challenges in obtaining experimental measurements.

When attempting to measure the resistance with the line of electrodes transverse to the fiber direction, the voltage (resistance) measurements were much larger in magnitude than recommended by the standard for the given current source of 10mA. For resistances above 20 Ohms, the standard recommends to use only 1mA current source. The power supply utilized in the current study was unable to provide a constant current source at this low magnitude, thus testing was not performed on these specimens. For

Table 4. 6. Experimental and FEM Results Using Point-Type 4-Probe Method

Specimen Type	Line of Electrodes in Fiber Direction (x-direction)			Line of Electrodes Transverse to Fiber Direction (y-direction)		
	Exper. $R_{top}$ [Ohm]	COMSOL $R_{top}$ [Ohm]	% diff	Exper. $R_{top}$ [Ohm]	COMSOL $R_{top}$ [Ohm]	% diff
16-U	3.94	3.94	0.00%	27.64	29.3	5.70%
32-U	3.92	4.94	0.50%	23.6	19.5	-17.40%
16-X	3.34	5.94	15.20%	0.184	0.211	12.80%
16-U-0BP	10.952	10.202	-6.80%	N/A	N/A	N/A
16-U-4BP	4.269	4.343	1.70%	N/A	N/A	N/A
16-U-7BP	2.885	2.828	-2.00%	N/A	N/A	N/A

these reasons, top resistance measurements were only recorded for tests with the line of electrodes aligned with the carbon fiber-direction. The best correlation between experimental and FE simulations was for specimen with layup 16-U-4BP, where the difference in top resistance was only 1.7%. The greatest error was for specimens with arrangements of 16-U-0BP at 6.8%. When observing trends due to the number of BP layers, it was clear that with the point-type 4-probe method, the BP content had less influence on the measured resistance. When increasing from 0 to 4 layers of BP, the resistance only decreased by 61%. Moreover when increasing from 4 layers to 7 layers of BP, resistance decreased by 32%, which was less than the 43% maximum theoretical decrease discussed earlier. This result suggested that the modified JIS method might demonstrate potential to: (i) reduce the influence of edge effects and (ii) provide a reliable method for 4-probe resistance testing. Overall, the average error was greater with the point-type 4-probe method compared to the standard line-type 4-probe method discussed previously.

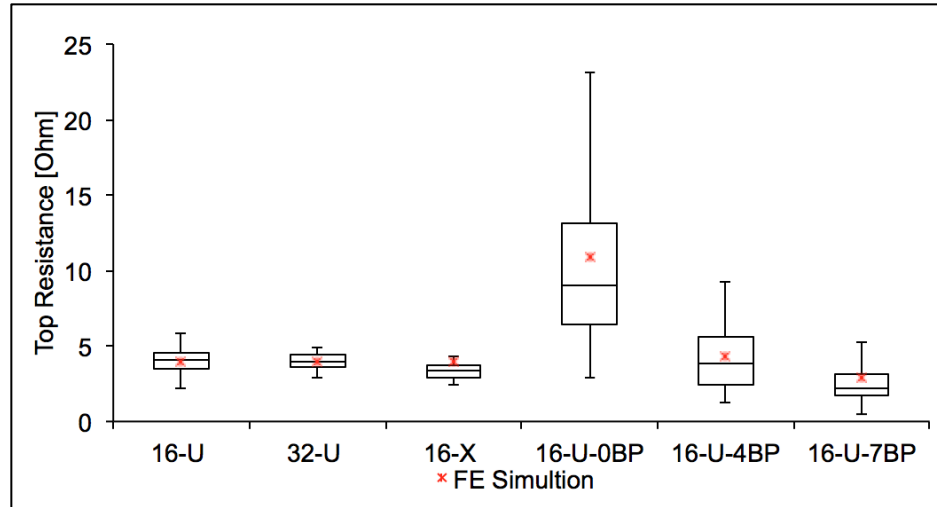


Figure 4. 6. Box plots of top resistance measurement for point-type 4-probe specimens with electrodes aligned with fiber direction of top ply.

The top resistance data was plotted in box-plot form in Figure 4. 6. for all specimens studied with the point-type 4-probe method. Similar to the results for the line-type method, the average top resistance was quite similar for specimens 16-U, 32-U, and 16-X. This was expected, because based on the previous discussion, the effective thickness (and FE model) for each of these specimens was identical. A significant takeaway from the box-plots was that for the hand-layup specimens with 0, 4, and 7 layers of BP, there was a much greater spread in the data compared to the 16-U, 32-U, and 16-X specimens. There are a couple potential explanations for the scatter in the experimental data. In the point-type 4-probe method, the electrodes were spaced very closely together, thus the resistance measurement was highly localized compared to the line-type method. The specimens were produced by hand, which generally increases the likelihood of introducing defects. Some of the observed data scatter could have been caused by localized defects in the specimens. These results motivated further study into the

local microstructure using CT imaging in Section 5.4. Another source of error could have been inherent to the experimental method.

Another potential source of error was identified as surface preparation. A previous study [21] showed that the specimen preparation was critical in ensuring consistency between specimens and to reduce error. Since the point-type 4-probe method did not utilize silver based paint to improve contact between the electrodes and specimen, it was expected that results might not be as consistent. Further refinement of the point-type 4-probe method may be needed in order to reduce variation in test results. As evidenced by Table 4. 4 and Table 4. 6, the magnitude of top resistance measurements was significantly different for the common line-type 4-probe method compared to the point-type 4-probe method, so resistance alone could not be used to compare the methods. The electrical resistivity takes into account the specimen dimensions and method of measurement and provided a better parameter to compare the two methods.

#### 4.5 Comparison of Line-Type and Point-Type 4-Probe Methods

In order to compare the line-type and point-type methods, the resistivity must be used, since resistivity is independent of geometry. As outlined in the procedures of Section 3.3.2, the line-type 4-probe method enables recovery of x, y, and z – direction resistivity values given the experimental voltage measurements on the top and bottom surfaces of the specimen. The results of Section 4.3 demonstrated the robustness in this method without requiring any assumptions on the relative magnitude of the resistivities in the principle directions. For the point-type 4-probe method, on the other hand, no bottom



voltage measurement was available, so the resistivity values could not be directly recovered from empirical data. However if prior data on  $\rho_x/\rho_y$  and  $\rho_x/\rho_z$  is available from the line-type 4-probe method (as in this study), the point-type 4-probe could be used to approximate the resistivity  $\rho_x$  by equation (4. 6). The x-direction resistivity  $\rho_x$  was calculated for point-type 4-probe method and was tabulated in Table 4. 2. The x-direction resistivity  $\rho_x$  for the point-type 4-probe method has been compared to the results for the line-type 4-probe method for the 16-U specimens in Figure 4. 7. Upon a cursory review, the box-plots in Figure 4. 7. resemble the resistance box-plots of Figure 4. 2 and Figure 4. 6, which follows intuition because electrical resistivity is directly related to electrical resistance. Consequently, only box plots of resistivity for 16-U were selected as an example to compare methods.

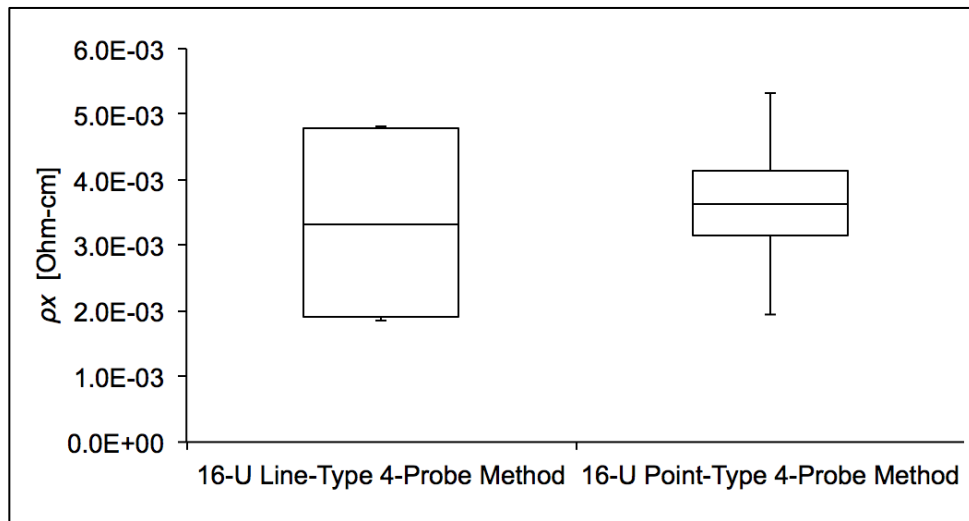


Figure 4. 7. Box-plot for fiber direction resistivity of 16-U specimens, using line-type 4-probe method and point-type 4-probe methods.

In general the median, maximum, and minimum were all very similar for both the line-type and point-type methods. The key difference was that the line-type 4-probe method had greater interquartile range compared to the point-type 4-probe method. This result highlights a prominent difference between the two methods. In the line-type 4-probe method, electrodes were permanently fixed to each specimen, which ensured that for each individual test specimen the data was precise. However, there was greater specimen-to-specimen variation in this method, because the results were subject to bias generated from specimen preparation. For the point-type 4-probe method, on the other hand, the electrodes were raised and reset onto the specimen for each measurement, which lead to a larger amount of data scatter for each individual specimen, however, there was not as much variation in the average from specimen to specimen. The results show that even though the sources of error were different in each method, both methods were capable of recovering the average resistivity in the fiber direction. This result has an important implication on the usefulness of the two methods.

If the directional resistivities of a given CFRP material are determined first using the line-type 4-probe method, the in-plane fiber-direction resistivity can be recovered using the point-type 4-probe method outlined above. This has great significance in the composites community, because the line-type 4-probe electrical method is a destructive method that requires permanent attachments of the electrodes to the surface. The point-type 4-probe method, on the other hand, is less invasive and does not require permanent modification of the composite surface in order to attach the electrodes. These results insinuate the prospect that the point-type 4-probe method could provide an alternative in the monitoring of electrical properties of CFRP composites. This newly developed point-

type 4-probe technique could provide value in the field of electrical resistance-based damage sensing where mechanical damage is correlated to electrical resistivity. If the initial undamaged state is characterized via the standard line-type 4-probe method, it may be possible to identify local damage via the point-type 4-probe method. While the discussion up until this point has focused on characterizing the electrical response of known CFRP specimens via experimental and FE simulation, in some applications it may be beneficial to use these models to optimize material properties based on the application.

#### 4.6 Optimization of Electrical Properties Based on Material Thickness

In the development of smart multifunctional materials, it may be useful to utilize the previously discussed analytical and FE models to target specific desired material properties. The current thesis work considered an electrically optimized material as a material with electrical properties such that the effective depth of Ohmic response  $z_{eff}$  in equation (2. 9) was equal to the physical thickness. In the current study, the electrical FE models only consider Ohmic current-voltage response within the effective thickness of the CFRP specimen. When applying these FE models in damage sensing applications in Chapter 5, the models are therefore only able to provide sensitive response to damage (fiber breakage, crack, delamination, etc.) when the damage is located within the effective thickness. Likewise, if the damage is located below the effective thickness, the 4-probe model will not capture the damage within the resistance measurement. For this reason, it is critical that the current must penetrate through the full thickness of the specimen, so that the damage can be sensed regardless of the location.

In order to optimize the electrical properties, a few assumptions were required: (i) the fiber direction resistivity  $\rho_x$  would be kept constant at 0.0034 Ohm-cm, and (ii) the resistivity in the through thickness direction  $\rho_z$  would be modified. In equation (2. 9)  $z_{eff}$  was set to the thickness of the specimen and the equation was solved for  $\rho_z$ . The material optimized here was considered an ideal unidirectional material, thus the electrical resistivities in the y and z directions were assumed to be identical. This assumption would be the ideal case for a transversely isotropic unidirectional CFRP composite. In order to distinguish between the simulations for the optimized material properties and the simulations with original properties, an additional term was added to the end of the specimen label to indicate the new material. For instance, specimen 16-U-T-Opt referred to a 16-ply unidirectional specimen with the line of electrodes transverse to fiber direction and optimal material properties. The optimal material properties were calculated for specimens with varying thickness (i.e.: 16-U and 32-U specimens). The optimized material properties calculated for 16-U-Opt and 32-U-Opt specimens are tabulated in Table 4. 7. Similar to the previous models, the properties for the 16-X FE simulations were assumed based on the 16-U material. Discussion of the FE simulation results for optimized properties are discussed in detail in Chapter 5.3 in the context of damage sensing capabilities.

Table 4. 7. Optimized CFRP Material Properties to Achieve Ohmic Response Through the Full Material Thickness

Specimen	t [mm]	$\sigma_x$ [S/m]	$\rho_x$ [Ohm-cm]	$\sigma_y$ [S/m]	$\rho_y$ [Ohm-cm]	$\sigma_z$ [S/m]	$\rho_z$ [Ohm-cm]
16-U-Opt	2.31	29330	0.0034	274.3	0.3645	274.3	0.3645
32-U-Opt	4.23	29330	0.0034	919.9	0.1087	919.9	0.1087

#### 4.7 2-Probe High Intensity Current Pulse: Results

A high-intensity current pulse was applied to specimens in Table 3. 2. using the custom current pulse generator in Figure 3. 2. The 2-probe electrical characterization tests were performed on pure CFRP specimens (16-U, 32-U, 16-X, 32-X) by Hart [45] and on CFRP specimens with 0, 4, and 7 layers of BP (16-U-0BP, 16-U-4BP, 16-U-7BP) by Hill [58]. The purpose of the electrical characterization was to observe the electrical response of these CFRP laminates subjected to a short-duration (~25ms) current pulse with intensity of up to ~1700 A. The analysis and interpretation of results for the 16-U, 32-U, 16-X, and 32-X specimens were discussed by Hart in a previous study [45] and are further analyzed in greater detail in the current work. In this previous study, a few noteworthy trends were observed during the electrical characterization tests.

When considering the current pulse generator, it was concluded that as the analog voltage increased on the generator, the maximum current in the test increased at a linear rate. This occurred because the magnitude of the current pulse was determined based on the charge voltage on the generator and the total system resistance (resistance of generator plus 2-probe resistance of specimen). Since the intensity of the current pulse was dependent on the resistance of the specimen, each specimen had a unique linear correlation between current magnitude and analog voltage. Next, it was determined that

the maximum current for a successful current pulse test always occurred at 6.5 milliseconds after start of the pulse, which was critical in ensuring the proper coordination of the current pulse and low-velocity impact, which will be discussed in Section 4.8.

As far as the specimen response, the study concluded that as the intensity of the current pulse increased, the 2-probe resistance of the specimen decreased. Moreover in comparing the resistance for each specimen type, the 32-U specimens had the lowest resistance whereas the 16-X specimens had the highest resistance. This occurred because as the thickness of the specimen decreased (from 32 to 16 plies), the current was constricted through a smaller cross-sectional area, which caused resistance to increase. Moreover, in the cross-ply specimens, the current was further constricted through the 0° plies leading to a further increase in specimen resistance. This previous study focused on the influence of specimen thickness and layup on the electrical resistance, and concluded that thicker unidirectional specimens had lower resistance and were less susceptible to electrical arcing and burning. In some applications, however, the thickness of the laminate may be limited and therefore other techniques must be used to reduce specimen resistance and improve electrical response. In the current study, this was attempted by adding layers of the carbon nanotube buckypaper to the CFRP specimens.

Three specimens of each type (16-U-0BP, 16-U-4BP, 16-U-7BP) were used for high-intensity current pulse characterization. Multiple tests were completed on each specimen with current pulse intensities ranging from ~250 A to ~1150 A in the previous work of Hill [58]. The results published in the previous work contained errors, which motivated further analysis of the experimental data in the current study. In the previous

study, the current pulse data was processed improperly such that current pulse data was computed as a running average over 5ms intervals. The running average the electrical current was then plotted every 0.1 ms. The resulting current pulse and voltage appeared inordinately smooth, given the high number of plotted points. In addition, the current pulse appeared to last for 30 ms, when the actual current pulse of only 25ms. Moreover, due to the 5ms smoothing function, the peak current pulse appeared to occur at approximately 10ms, where as the actual peak occurred at 6.5ms. This result was particularly concerning, because the 6.5ms peak was critical in achieving coordinated current pulse, which is discussed in Section 4.8. In the current study, the raw data from the current pulse tests was recovered and refined by smoothing over 0.5 ms increments, which was the same increment used in the tests by Hart [45]. The full electrical characterization results are included in the Appendix A Table A. 1. for all 2-probe specimens. Using the corrected experimental data, the current versus time was plotted for select specimens at three voltage levels in Figure 4. 8. Similar conclusions were drawn for the BP specimens compared to the CFRP specimens of the previous study [45]. The peak current pulse occurred at ~6.5 ms for each current pulse test, and as the analog voltage on the generator increased, the amplitude of the current pulse increased as well. In order to compare the electrical response of individual specimen types, the 2-probe resistance provides a superior measuring stick compared to the system current pulse.

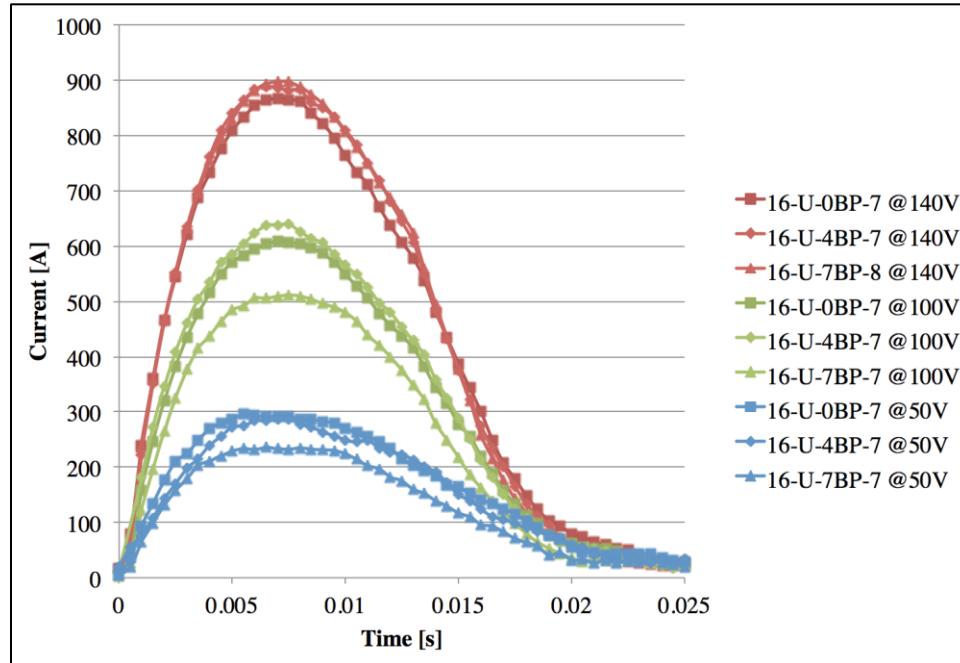


Figure 4. 8. Electric current vs. time comparing specimens with 0, 4, and 7 layers of buckypaper at analog voltages of 50, 100, and 140V.

When comparing to the 16-U-0BP specimens, the peak current magnitude observed in 16-U-4BP specimens were 3.7% and 2.6% higher at analog voltage levels of 100 V and 120V, respectively. More significantly, the addition of four layers of buckypaper lead to resistances that were 9% and 26% lower at 80 V and 140 V, respectively. For 16-U-7BP specimens, the resistance decreased by 14% and 25% compared to the 16-U-0BP specimens, but demonstrated no significant change compared to specimens with 4 layers of buckypaper. These trends were evident visually through plotting the average specimen resistance versus current intensity in Figure 4. 9. Similar to the previous study [45], the average resistance decreased as the intensity of the applied current increased. Moreover, the specimens containing BP layers (16-U-4BP and 16-U-7BP) had lower resistance at every current level compared to the specimens with no



layers of BP (16-U-0BP). Additionally, in comparing the specimens with 4 and 7 layers of BP (16-U-4BP and 16-U-7BP) as the intensity of the current pulse increased, the resistance versus current curves began to converge. Based on these results, adding 4 BP layers to the CFRP composite had a positive influence on 2-probe resistance of the specimen, however, diminishing returns were observed when adding additional BP layers. Once the electrical characterization tests were performed, the current-pulse generator was implemented alongside the low-velocity impact tower of Figure 3. 2. to observe the influence of the high-intensity current pulse on the low-velocity impact response of the CFRP and CFRP/BP laminates.

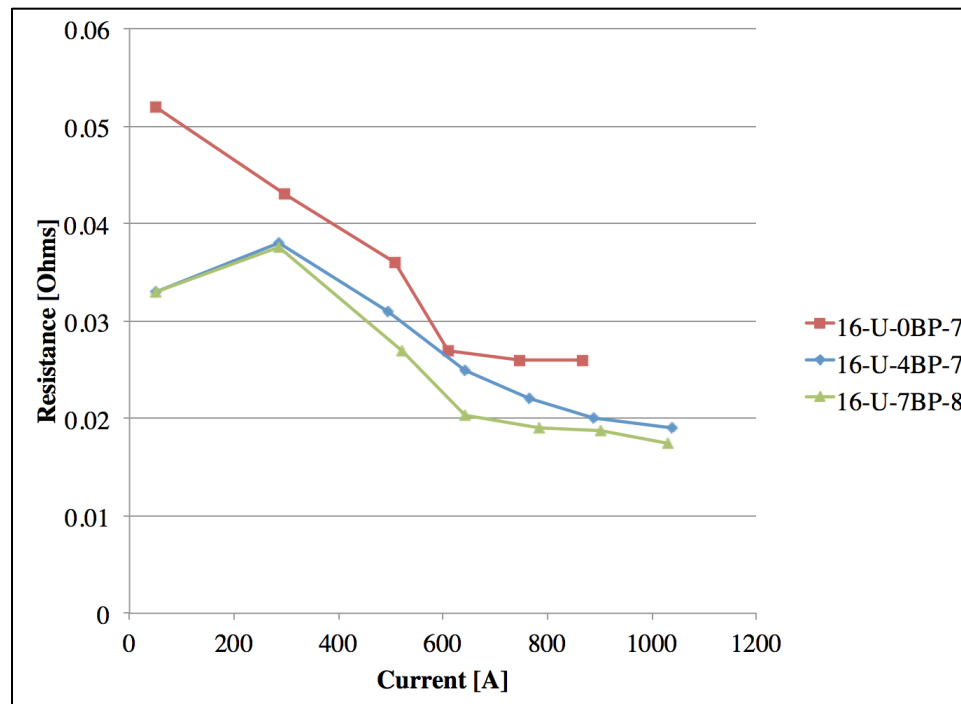


Figure 4. 9. Average electrical resistance vs. current comparing specimens with 0, 4, and 7 layers of buckypaper.

## 4.8 Impact Characterization and Coordinated Electrified-

### Impact Testing: Results

As discussed in the Literature Review in Section 2.4, several studies [39,40,45,46] have demonstrated that application of electric current can temporarily improve the peak impact force and absorbed energy of CFRP specimens subjected to low-velocity impact. Moreover, as the intensity of the current increased the impact benefits increased further. The short-duration high-intensity current pulse was identified as a potential method for maximizing the current pulse intensity while limiting the thermal effects (i.e.: matrix softening and cracking). The method of simultaneously applying a high-intensity current pulse has been detailed by Hart in previous work [45,46] and summarized in the current study in Section 3.4. In order to set a baseline for each specimen's impact performance, impact characterization testing was performed first on each specimen and then coordinated electrified impact testing was performed to determine the influence on the high-intensity current pulse on the impact response. The results for peak impact load, absorbed energy, and visual damage are presented in Table 4.8.

In comparing the results in Table 4.8. to the previously published results of Hart and Hill [45,58], a couple differences are immediately apparent. First, when analyzing the previous literature, it was determined that the absorbed energy values that were reported were incorrect. In the previous work, the reported absorbed energy was taken directly from the calculations made by the Instron Dynatup software. The software automatically calculated the absorbed energy by integrating underneath the force versus deflection curves. When calculating by this integration method, the absorbed energy is only correct if at the end of the test, the impact load returns to zero. For several of the tests, however,

the impact load did not return to zero, which meant that the absorbed energy was over reported. In the current work, the raw data was obtained and for tests in which load did not return to zero, the impact load was forced to zero at the end of the test by extending the force versus deflection curve so that it intersected the x-axis. The intersection point was estimated using linear approximation given the slope of the force versus deflection curve at the end of the test. The absorbed energy was then integrated using the trapezoidal technique. Another item of note is that the peak current values reported in Table 4.8. are different from Hill [58], due to the current smoothing errors in the previous work that were discussed previously in Section 4.7.

The impact testing was performed at impact energies such that barely visible impact damage was induced in approximately half of the tested specimens. For the unidirectional specimens, the visible damage emerged in the form of a line crack through the epoxy matrix and in the direction of the carbon fibers, as shown in Figure 4. 10. (a). For cross-ply specimens, the visual damage was revealed in the form of delamination and fiber breakage on the backside of the impacted specimen, as evidenced in Figure 4. 10. (b). For 16-U specimens, after impact characterization was performed, it was determined that the coordinated electrified-impact testing could not be safely performed on the specimens without significant electrical arcing and burning. When considering the 32-U specimens, however, some significant trends were observed.

For 32-U specimens, all electrified and non-electrified specimens sustained minor visible damage in the form of a line crack. Since the mass, drop height, and impact energies were all similar, any significant difference in peak load and absorbed energy was

Table 4. 8. Impact Data for Impact Characterization Tests and Coordinated Electrified-Impact Tests

Specimen ID	Velocity [m/s]	Impact Energy [J]	Absorbed Energy [J]	Peak Load [N]	Peak Current [A]	Visual Impact Damage	Electrical Arcing/Burning
16-U-10	1.235	4.1962	1.8386	1895.4	---	no	---
16-U-11	1.235	4.1982	1.7743	1894.7	---	no	---
16-U-12	1.232	4.1793	1.7526	1894.7	---	no	---
<b>Average</b>	<b>1.234</b>	<b>4.1912</b>	<b>1.7885</b>	<b>1894.9</b>	---	---	---
32-U-10	1.769	8.6101	3.9601	4496.9	---	yes	---
32-U-11	1.767	8.5916	2.9478	2610.2	---	yes	---
32-U-12	1.768	8.5993	3.6573	4009.2	---	yes	---
<b>Average</b>	<b>1.768</b>	<b>8.6003</b>	<b>3.5217</b>	<b>3705.4</b>	---	---	---
32-U-13	1.765	8.576	4.1943	4503.7	964	yes	no
32-U-14	1.766	8.5867	4.2453	4449.3	906	yes	no
32-U-15	1.768	8.5974	3.525	4063.9	957	yes	no
<b>Average</b>	<b>1.766</b>	<b>8.5867</b>	<b>3.9882</b>	<b>4339.0</b>	<b>942</b>	---	---
32-U-16	1.771	8.6286	4.1302	4850.9	1631	yes	no
32-U-17	1.77	8.6227	3.659	4208.3	1516	yes	no
<b>Average</b>	<b>1.77</b>	<b>8.6256</b>	<b>3.8946</b>	<b>4529.6</b>	<b>1574</b>	---	---
16-X-10	2.434	38.4286	24.0671	9863.3	---	yes	---
16-X-11	2.432	38.3706	24.1148	9844.8	---	yes	---
16-X-12	2.433	38.4042	16.4313	9785.8	---	no	---
<b>Average</b>	<b>2.433</b>	<b>38.4011</b>	<b>21.5377</b>	<b>9831.3</b>	---	---	---
16-X-13	2.433	38.3996	17.9697	9744.1	758	no	yes
16-X-14	2.432	38.3611	41.632	9659.6	577	yes	yes
16-X-15	2.433	38.3970	25.1559	9404.8	605	yes	yes
<b>Average</b>	<b>2.433</b>	<b>38.3859</b>	<b>28.2525</b>	<b>9602.8</b>	<b>647</b>	---	---
16-U-0BP-10	1.4842	3.8548	0.8255	1490.6	---	yes	---
16-U-0BP-11	1.4826	3.8469	1.0743	1834.4	477	no	no
16-U-0BP-12	1.4796	3.8312	0.2398	1367.9	---	yes	---
16-U-4BP-10	1.4867	3.868	1.0383	1974.0	---	no	---
16-U-4BP-11	1.4799	3.8327	2.1908	1923.4	321	yes	yes
16-U-4BP-12	1.4808	3.8375	0.8173	1376.4	1037	yes	no
16-U-7BP-10	1.4793	3.8294	0.6345	1664.9	---	yes	---
16-U-7BP-11	1.4833	3.8504	0.9428	2007.6	510	no	no
16-U-7BP-12	1.4862	3.8652	0.0409	1417.6	778	yes	yes

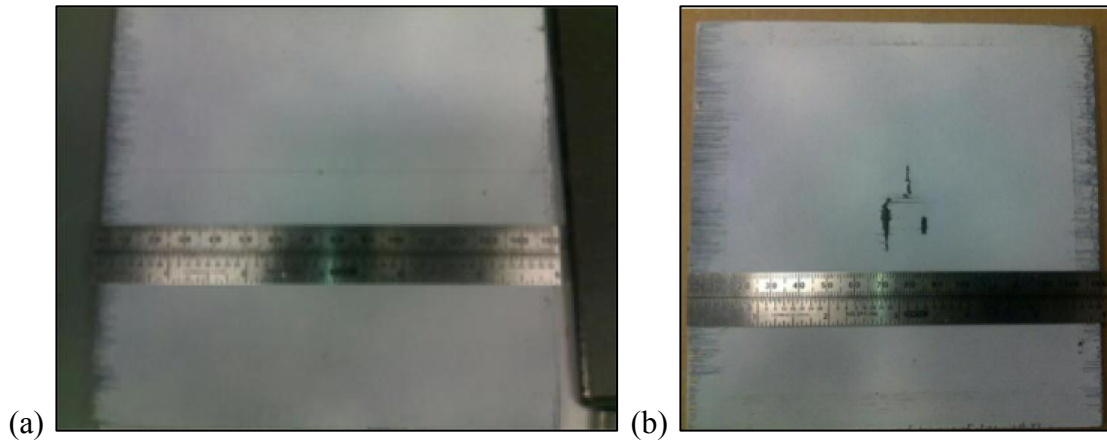


Figure 4. 10. Impact damage in the form of (a) line crack on unidirectional specimen and (b) delamination and fiber breakage on cross-ply specimen [45].

attributed to the influence of the high-intensity current pulse. The average peak load increased from 3705.4 N to 4339.0 N to 4529.6 N for specimens with no current pulse, 942 A current pulse, and 1574 A current pulse, respectively. Hence, the application of the 942 A current pulse led to a 17% increase in average peak impact load compared to non-electrified specimens. Furthermore, the 1574 A current pulse resulted in a 22% increase in average peak impact load of over non-electrified specimens. Similarly, the average absorbed energy in the electrified specimens was 13% and 11% greater due to the application the 942 A current pulse and 1574 A current pulse, respectively. These trends are visually evident in the plots of average peak load and average absorbed energy in Figure 4. 11. and Figure 4. 12., respectively. For the 16-X specimens, on the other hand, the high-intensity current pulse was correlated with a slight diminishment of peak impact load.

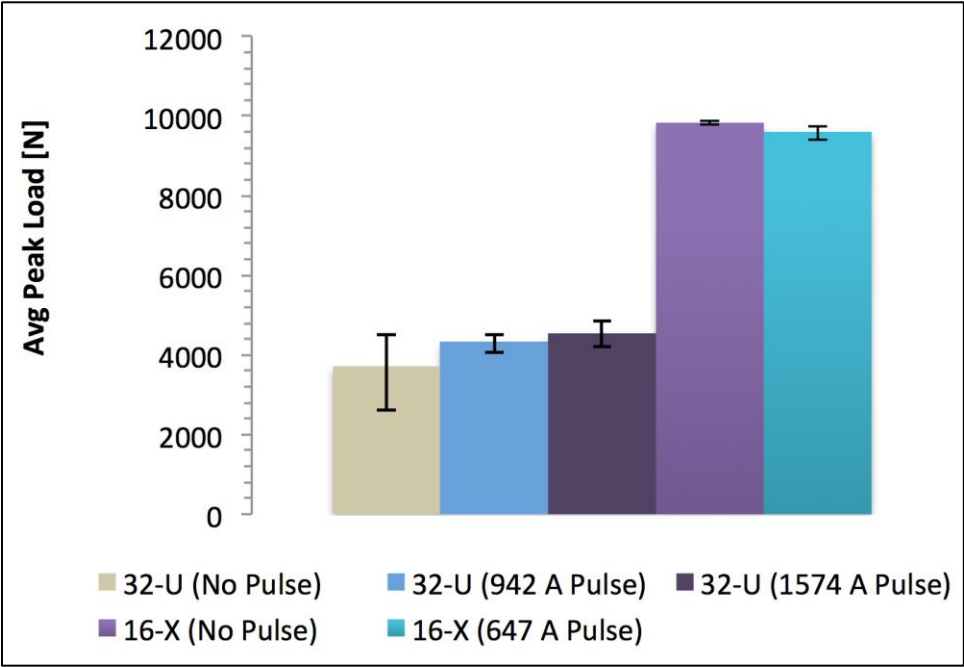


Figure 4. 11. Average peak impact load for 32-U and 16-X impacted specimens. Error bars show highest and lowest values for individual specimens.

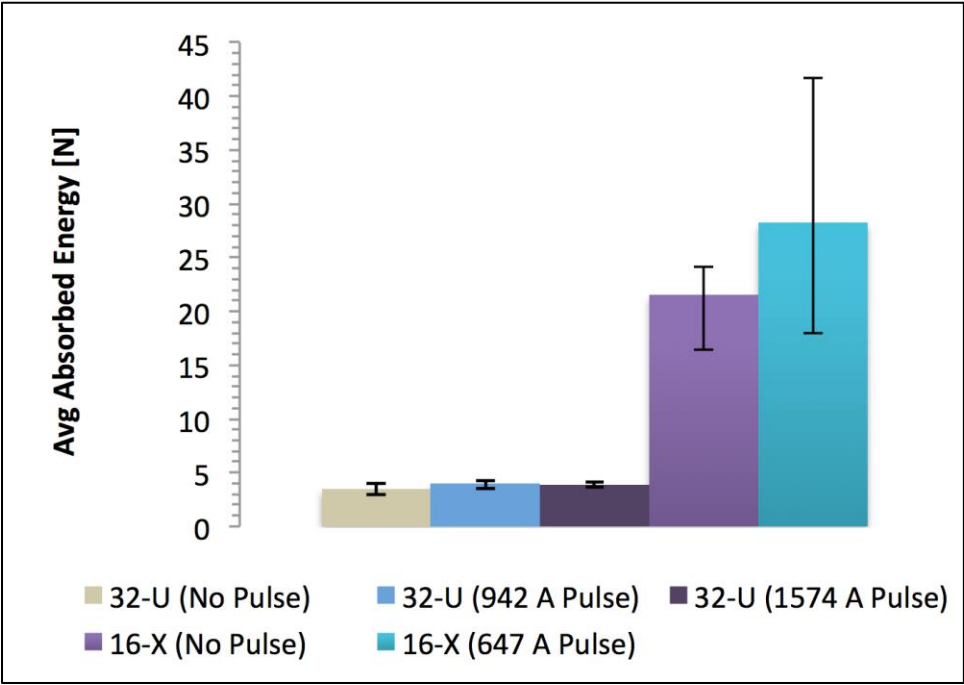


Figure 4. 12. Average absorbed energy for 32-U and 16-X impacted specimens. Error bars show highest and lowest values for individual specimens.

The average peak impact load decreased by 2.32% for 16-X specimens subjected to a current pulse of 647 A compared to specimens with no current pulse applied. The peak impact load was lower for every electrified specimen compared to the non-electrified specimens. It is noteworthy that for every electrified 16-X specimen, significant electrical arcing and burning occurred in the specimen, which was likely the cause of the small reduction of peak impact load. The average absorbed energy, on the other hand, increased by 31.2% for the electrified specimens compared to the non-electrified specimens. The average absorbed energy of the electrified specimens was heavily influenced by the specimen 16-X-14, which had an absorbed energy of 41.632 J, which corresponded to a 93.3% increase over the average absorbed energy of the specimens with no current pulse applied.

The absorbed energy was calculated by integrating underneath the load versus deflection curve from the start of the impact to the point at which the load returned to zero. For most specimens, the load versus deflection curve resembled the curves for 16-X-11 and 16-U-10 in Figure 4. 13. where the load increased as deflection increased and as the specimen deflected back, the specimen was unloaded with some hysteresis. For the specimen 16-X-14, the load returned to zero very shortly after the peak load occurred, which led to the significantly higher absorbed energy when integrating under the curve. This single specimen was an outlier compared to the others, and with the limited sample size (3 specimens) in the current study, a definitive conclusion could not be made on the influence of the high-intensity current pulse on 16-X specimens. For the specimens 16-U-0BP, 16-U-4BP, and 16-U-7BP, the influence of the high-intensity current pulse also yielded mixed results.

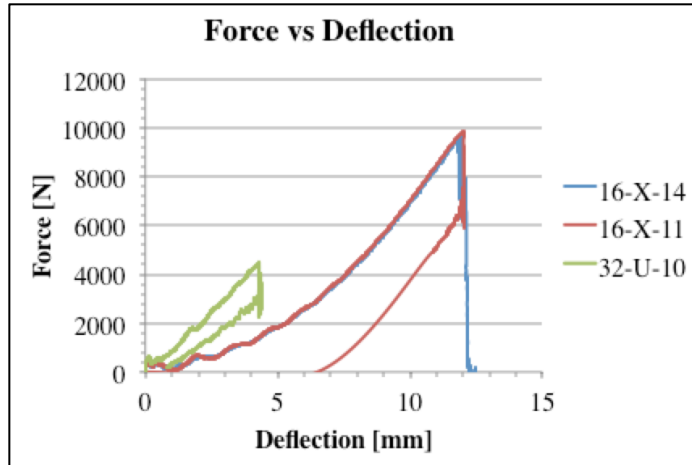


Figure 4. 13. Force versus deflection curves for specimen 16-X-11 with no current pulse and specimen 16-X-14 with high-intensity current pulse.

The hand layup specimens with 0, 4, and 7 layers of BP (16-U-0BP, 16-U-4BP, and 16-U-7BP) were produced individually in three separate batches. Due to the hand-made nature of these specimens and the influence of the BP layers on stiffness, each specimen was evaluated independently in regards to impact resistance and absorbed energy and results were not averaged. When considering the specimens with no layers of BP, the specimen 16-U-0BP-11 had the highest peak impact load (1834.4 N) and absorbed energy (1.0743 J) compared to specimens 16-U-0BP-10 (1490.6 N and 0.8255 J) and 16-U-0BP-12 (1367.9 N and 0.2398 J). It is noteworthy that the specimen 16-U-0BP-11 was subjected to a current pulse of 477 A, whereas the other two specimens had no current pulse applied. For the specimens with 4 layers of BP, the highest peak impact load of 1974.0 N was observed in the non-electrified specimen 16-U-4BP-10. In comparison, the electrified specimens 16-U-4BP-11 and 16-U-4BP-12 had peak impact loads of only 1923.4 N and 1376.4 N, respectively. When comparing absorbed energy, the highest absorbed energy belonged to the specimen 16-U-4BP-11 (2.1908 J) followed



by the specimens 16-U-4BP-10 (1.0383 J) and 16-U-4BP-12 (0.8173 J). Interestingly, the specimen 16-U-4BP-11, which had the greatest absorbed energy, was the only specimen of this type that was burned from the current pulse. Similar mixed results were observed for the specimens with 7 layers of BP. The highest absorbed energy and peak load was observed in the electrified specimen 16-U-7BP-11 (497.4 A current pulse), whereas the lowest peak impact load and absorbed energy was recorded for the electrified specimen 16-U-7BP-12 (754.9 A current pulse). It should be noted that the specimen 16-U-7BP-11 was not burned from the current pulse, whereas the specimen 16-U-7BP-12 showed evidence of significant burning, which could have influenced the results.

Overall, due to the limited sample size of the BP specimens (16-U-0BP, 16-U-4BP, 16-U-7BP), no definitive conclusions could be drawn from the results of these specimens. In order to better evaluate the influence of the high-intensity current pulse on the impact response of the specimens, a minimum of three specimens of each type would need to be tested under each condition. Due to material availability the current study was only able to test 1 specimen of each type at each test condition. Another item that complicated interpretation of the results for the BP specimens was that the impact testing was performed in the work of Hill [58], where the current pulse signals were incorrectly processed. This error in signal processing could have caused the current pulse to be incorrectly timed with respect to the impact load. The objective of the coordinate impact was to time the peak of the current pulse to the peak impact load. The incorrect signal processing could have caused the coordination of the current and load to be shifted by as much as 5ms. The hand-made nature in which the specimens were produced also

contributed to the uncertainty in interpreting the results. This result further stimulated the study of the microstructure of these specimens using CT imaging in Section 5.4.

#### 4.9 Electrical and Impact Response: Summary

In this chapter, the electrical models of Busch et al [16] were extended to gain better physical insight into the line-type and point-type 4-probe methods. The concept of effective conducting thickness was leveraged in development of macro-scale electrical FE models. The consideration of the effective conducting thickness was critical in order to accurately predict electrical resistance compared to experimental data. Moreover the electrical FE models demonstrated predictive capabilities when applied to specimens with varying thickness and layup. When comparing the line-type and point-type methods, the fiber-direction electrical resistivity was comparable between the two methods. In the line-type method, the measurements were more precise for a given specimen, however there was more specimen-to-specimen variation due to specimen preparation bias. For the point-type method the measurements were less precise with more random scatter, however there was less noticeable variation from specimen to specimen. In order to guarantee that the current density penetrated through the full thickness of the specimen, the electrical properties in the through-thickness direction were theoretically optimized such that the effective thickness was equivalent to the physical specimen thickness. Finally, the influence of the high-intensity current pulse on low-velocity impact was analyzed. For 32-U specimens, the high-intensity current pulse correlated with an increase in peak impact load and absorbed energy. For 16-X specimens, however, the current pulse coincided with an increase in absorbed energy but a reduction in peak

impact load. The reduction in peak impact load was likely due to excessive electrical arcing and burning which occurred in the 16-X specimens. In order to apply the 4-probe electrical FE models of the current chapter in damage sensing applications, a feasibility study was performed for sensing damage of specified size and location.

## CHAPTER 5: DAMAGE SENSING FEASIBILITY MODELS

In Section 4.3, FE models were developed in COMSOL for line-type 4-probe specimens. The electrical resistivities were recovered from experimental data for 16-ply unidirectional specimens. When applying these electrical properties for the 16-U specimens to FE models with varying specimen thickness and layup, the FE models demonstrated predictive capabilities by correctly simulating the specimen resistance, in comparison to the experimental results. The FE models in Section 4.3 relied on the concept of effective thickness to achieve accurate results. In the current chapter, the concept of effective thickness is extended to evaluate the feasibility of the electrical models in damage sensing applications. The objectives for the damage sensing feasibility study included: (i) develop line-type 4-probe models in ABAQUS for damage sensing applications (section 5.1), (ii) determine the influence of prescribed damage to CFRP laminates with varying thickness and layup (section 5.2), (iii) evaluate damage sensing feasibility for FE models using thickness-optimized material properties discussed in Section 4.6 (section 5.3), and (iv) generate a summary of the influence of damage and voids on the electrical response (section 5.4).

### 5.1 Development of Damage Sensing Feasibility Models

#### 5.1.1 FE Models: Prescribed Fiber Breakage and Matrix

##### Cracks

FE models were developed in COMSOL for line-type 4-probe specimens in Section 4.3. The models were then replicated in ABAQUS for the purpose of damage

sensing for Chapters 5 and 6. Although the modeling could be performed using either software package, the advantages of ABAQUS over COMSOL were identified as: (i) ABAQUS has superior mesh generation and adaptive meshing capabilities, (ii) ABAQUS is a more commonly used FEA package compared to COMSOL, which is advantageous for other researchers, and (iii) ABAQUS allows for multiple models within a single CAE database, which is advantageous for file organization. A couple slight differences were identified in the modeling process when comparing the COMSOL and ABAQUS models.

In COMSOL the current sources were applied as volumetric current density, where as in ABAQUS the current was applied as a current flux over an area. For the ABAQUS models, the electrodes were modeled as rectangular blocks and the current flux was applied to top surface of the electrode as shown in Figure 5. 1. It was critical that the current flux was applied to the copper electrode and not directly to the CFRP material, because once damage was introduced into the model, the current needed to be able to flow naturally around the damage, which would not occur if the current density was forced uniformly over width the CFRP material. The voltage drop was measured between the two sensing electrodes on the top of the specimen using internal probe functions in ABAQUS and the top resistance was calculated by dividing the voltage by current. The specimens 16-U, 32-U, and 16-X were modeled using standard linear, thermal-electric hexagonal elements. In order to better differentiate between the FE models, an additional term was added to the end of the naming sequence for the damage models. For specimens with the line of electrodes oriented with the fiber direction an “F” was added to the end of the specimen label. Similarly, for the specimens with the line of electrodes transverse to the fiber direction the letter “T” was added to the label. For instance the 32-ply

unidirectional models with line of electrodes oriented with fiber direction were referred to as 32-U-F. The material properties dimensions of the specimens in Chapter 5 were the same as the previous models, given in Table 4. 1. and Table 4. 2.

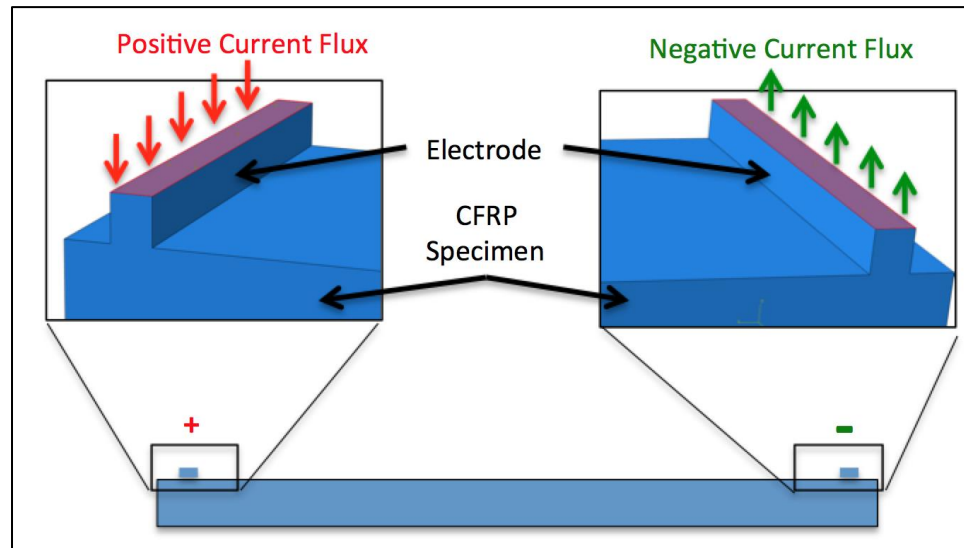


Figure 5. 1. Current load applied as current flux per unit area on the source electrodes in top resistance test.

In order to study the influence of damage on electrical resistance, simulated damage was added to the models. The modes of damage studied in the current work included localized fiber breakage and matrix cracking. For both damage modes, it was assumed that the damage was significant enough that there was no current flow across the damaged region, as shown in the Literature Review Figure 2. 5. (b) [26]. In the continuum models developed herein, there was no distinction between the fibers and matrix. Therefore instead of modeling the individual broken fibers (or cracked matrix), the material properties of the localized element were modified to represent the damage, similar to the work of Pyrzanowski et al. [26].

The material properties of the damaged elements were modified such that the electrical conductivity was near zero (ABAQUS will not allow conductivity equal to zero) thus preventing any current from passing through the damaged elements. The damaged elements were introduced into the models at the center of each specimen as shown in Figure 5. 2. The damage modeled in the current work corresponded to the specifications in Table 5.1. and were characterized as: top matrix crack, bottom matrix crack, side matrix crack, center-top fiber breakage, center-bottom fiber breakage, and center-thru fiber breakage. The fiber breakage was modeled in tests with the line of electrodes oriented with the fiber direction, whereas the matrix cracks were modeled in the tests with the line of electrodes transverse to fiber direction. These orientations were used to provide the most sensitive response of resistance to the specified damage. In addition to fiber breakage and matrix cracking, delamination poses a significant threat to the performance of CFRP laminates.

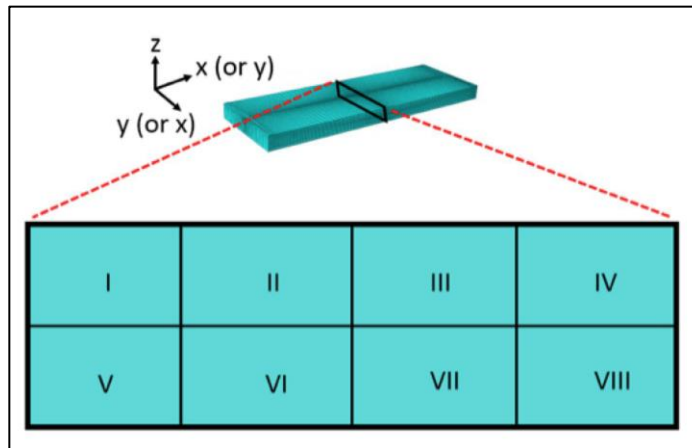


Figure 5. 2. Zones of damage located at center of specimen in finite element models.

Table 5. 1. Locations of damage modeled in finite element simulations. <sup>1</sup>For unidirectional specimens area is total cross sectional area. For cross-ply specimens area is percentage of individual layer cross sectional area

Description of Damage	Direction of Line of Electrodes	Zones Included (refer to Figure 5. 2.)	Area of Damage (as % of cross-sectional area <sup>1</sup> )
Top Matrix Crack	y (transverse to fibers)	I, II, III, IV	50%
Bottom Matrix Crack	y (transverse to fibers)	V, VI, VII, VIII	50%
Side Matrix Crack	y (transverse to fibers)	III, IV, VII, VIII	50%
Center-Top Fiber Breakage	x (fiber direction)	II, III	25%
Center-Bottom Fiber Breakage	x (fiber direction)	VI, VII	25%
Center-Thru Fiber Breakage	x (fiber direction)	II, III, VI, VII	50%

#### 5.1.2 FE Models: Prescribed Delamination

Different from the failure modes of fiber breakage and matrix cracking, previous literature [17] noted that in the 4-probe experiment, the top resistance plane is generally considered insensitive to delamination damage. In order to sense delamination, the literature proposed that a through-thickness measurement plane was required, such as the oblique measurement plane (through thickness at an oblique angle). The current feasibility study aimed to test this hypothesis by introducing delamination damage of multiple sizes into CFRP specimens with varying thickness and layup. The top resistance and oblique resistance were recorded from the FE results and compared to specimens with no damage in order to determine the influence of delamination damage. Similar to the study of fiber breakage and matrix cracking, it was assumed that the delamination damage was significant enough that there was no current flow through the delaminated region [26]. The material properties of the damaged elements were modified such that the electrical conductivity was near zero (ABAQUS will not allow conductivity equal to



zero) thus preventing any current from passing through the damaged elements. It noteworthy that in the case of slight delamination, fibers in adjacent plies could still touch and conduct electric current through the delaminated area but at a reduced rate compared to an undamaged laminate. This case was not included in the feasibility study, but could be easily modeled by simply reducing the through-thickness conductivity of the damaged elements.

The delamination damage was introduced into the models at the every interface between plies with different fiber angles, as shown in Figure 5. 3. For example, in a 16-ply AS4/3501-6 [0/45/-45/90]<sub>2S</sub> laminate there were 14 interfaces between plies with different angles. The interfaces were modeled as a very thin layer of ~ 0.04 mm, which was approximately 1/3 thickness of an individual ply. The thickness of the delamination was approximated based on CT scans of cross-ply CFRP specimens by Demerath [50]. The delamination modeled in the current study corresponded to the specifications in Table 5.2. and were characterized as: small delamination, moderate delamination, and large delamination. The undamaged CFRP material was specified with AS4/3501-6 electrical properties where as the damaged elements were given a near zero electrical conductivity. This material was selected for the feasibility study, because based on the results of the electrical characterization in section 4.3, the effective thickness was high enough such that the current would penetrate through the full thickness of the specimen during the top resistance test. Effective thickness was a limiting factor with the IM7/977-2/3 specimens used in the feasibility study for matrix cracking and fiber breakage. For all FE models, the specimen dimensions were 152.4 x 152.4 mm with probes spaced 30 mm apart.

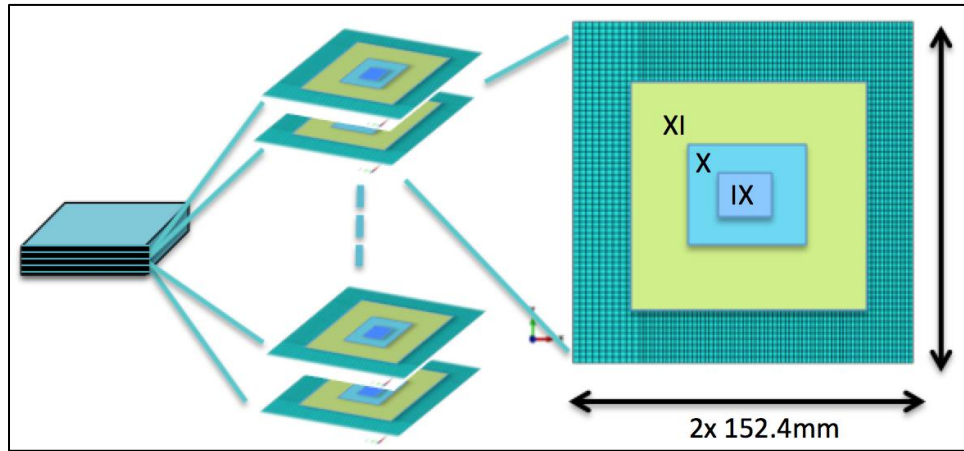


Figure 5. 3. Locations of delamination damage for damage sensing feasibility study.

Table 5. 2. Specification of Delamination Damage for Damage Sensing Feasibility Study

Description of Damage	Zones Included (refer to Figure 5. 3)	Dimensions of Delamination (per interface)
Small Delamination	IX	25mm x 25mm
Moderate Delamination	IX,X	50mm x 50mm
Large Delamination	IX,X,XI	100mm x 100mm

## 5.2 Influence of Prescribed Damage to Various CFRP

### Layups: FE Results

#### 5.2.1 FE Results: Prescribed Fiber Breakage and Matrix Cracking

When analyzing the top resistance results in Table 5. 3. some noteworthy observations are made. First, when comparing the results for specimens with no damage, the difference between the ABAQUS results and previous COMSOL results was less than

2.5% for all simulations. The difference in the results was primarily attributed to mesh refinement. The ABAQUS models had a finer mesh compared to the COMSOL models, which was done to achieve better resolution around the areas where the prescribed damage was applied. In comparison to the experimental results, the ABAQUS models were also in good agreement and there was no significant difference in the error compared to the COMSOL models. Considering this result, the ABAQUS electrical models were validated for undamaged specimens. In order to assess the damage sensing capabilities of the electrical models, prescribed damage was introduced into the models as described in Section 5.1.

A summary of top resistance measurements is plotted in Figure 5. 4. for specimens evaluated in the damage sensing feasibility study. For the 16-U-T specimens, the top and bottom matrix cracks both resulted in top resistance measurements of 222 Ohms compared to 196 Ohms for the undamaged specimen, which corresponded to a 13% increase. For the 32-U-T specimens, on the other hand, the top matrix cracks resulted in a top resistance measurement of 143 Ohms compared to 141 Ohms for the bottom matrix crack. When comparing to the undamaged state, the top matrix crack led to a 17% increase compared to 15% for the bottom matrix crack. When considering the side matrix crack, neither the 16-U-T nor 32-U-T specimens showed a significant increase in top resistance measurement due to this type of damage. The side crack led to only 0.5% and 0.6% increases in resistance for the 16-U-T and 32-U-T specimens, respectively. Based on these initial results it is clear that with this fiber orientation, the top resistance measurement is much more sensitive to top and bottom cracks that span the entire width of the specimen compared to a crack located towards one side of the specimen.

Moreover, the results of the 16 and 32-ply simulations suggest that as the thickness of the laminate increases, the top matrix crack may lead to a larger increase in resistance compared to the bottom matrix crack.

Table 5. 3. Finite Element Results for Electrical Resistance for Fiber Breakage and Matrix Cracking Using 4-probe Method

Specimen Type	Damage Mode	ABAQUS Rtop [Ohm]	Experimental Rtop [Ohm]	COMSOL Rtop [Ohm]
16-U-T	None	1.96E+02	2.00E+02	2.01E+02
	Top Matrix Crack	2.22E+02		
	Bottom Matrix Crack	2.22E+02		
	Side Matrix Crack	1.97E+02		
32-U-T	None	1.23E+02	1.37E+02	1.21E+02
	Top Matrix Crack	1.43E+02		
	Bottom Matrix Crack	1.41E+02		
	Side Matrix Crack	1.23E+02		
16-X-T <sup>1</sup>	None	3.50E-01	3.57E-01	3.40E-01
<sup>1</sup> matrix crack in top transverse direction layer only	Top Matrix Crack	3.50E-01		
	Bottom Matrix Crack	3.50E-01		
	Side Matrix Crack	3.50E-01		
16-U-F <sup>2</sup>	None	3.39E-01	3.34E-01	3.39E-01
<sup>2</sup> same model for 32-U-F and 16-X-F	Center-Top Fiber Breakage	4.67E-01		
	Center-Bottom Fiber Breakage	3.86E-01		
	Center-Thru Fiber Breakage	2.68E+00		
16-X-T <sup>3</sup>	None	3.50E-01	3.57E-01	3.40E-01
<sup>3</sup> fiber breakage in bottom fiber direction layer only	Center-Top Fiber Breakage	4.25E-01		
	Center-Bottom Fiber Breakage	3.96E-01		
	Center-Thru Fiber Breakage	7.90E-01		

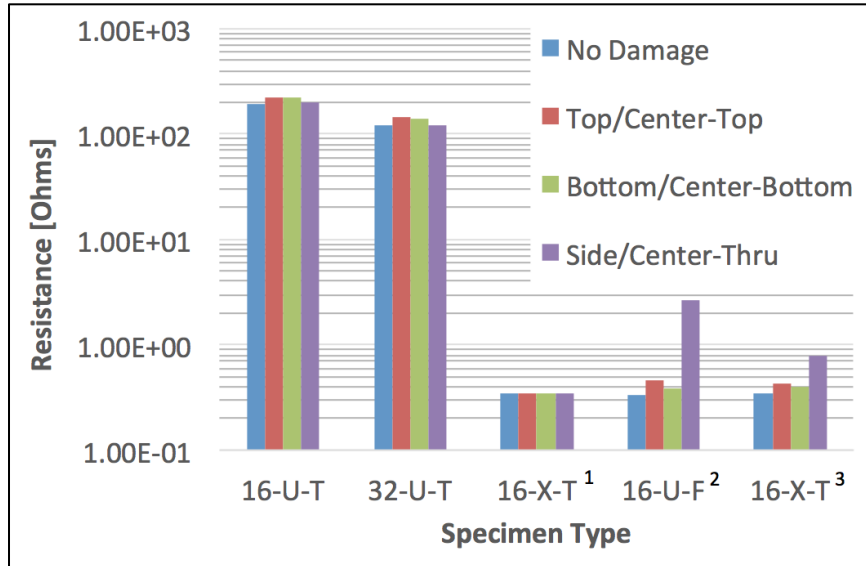


Figure 5. 4. Bar-plot for 4-probe top resistance for finite element simulations. Note: legend description “Top” refers to “Top Matrix Crack” and “Center-Top” refers to “Center-Top Fiber Breakage” in Tables III – IV.

<sup>1</sup> matrix crack in top transverse layer only, <sup>2</sup> same model for 32-U-F and 16-X-F, <sup>3</sup> fiber breakage in bottom fiber direction layer only.

The influence of fiber breakage was investigated in the 16-U-F models, and the results were staggering. Center-top fiber breakage increased the top resistance by 38% compared to the undamaged state. Comparatively, the center-bottom fiber breakage led to only a 14% increase in resistance measurement. For the simulation with center-through fiber breakage, the resistance measurement raised by an astounding 691% compared to the original undamaged simulation. These results not only show the dramatic influence of damage to the carbon fibers, which form the conductive network through the composite material, on electrical resistance but also demonstrate the legitimacy of resistance based damage sensing.

For the cross-ply specimens 16-X-T, the results were mixed. For simulations with a matrix crack in the top transverse direction layer, there was no recordable difference in

the damaged and undamaged states. This result is significant, because it indicates that the top resistance measurement may not be capable of detecting matrix cracks in cross-ply CFRP laminates. Fiber breakage in the second layer, on the other hand, was detectable through the FE simulations. Center-top fiber breakage increased the top resistance by 21% compared to the undamaged state. Similarly, the center-bottom fiber breakage led to a 13% increase in the top resistance measurement. In the simulation with center-through fiber breakage, the resistance measurement raised by 125% compared to the original undamaged simulation. These trends in resistance were similar to the 16-U-F specimens discussed previously, however the overall magnitude of resistance was not as great as in the unidirectional specimens. This conclusion follows the previous COMSOL results in Figure 4. 4. (b) and Figure 4. 5. (b) where the current penetrated through the thickness of the top ply and was concentrated within the second fiber-direction layer. These results indicate that stacking layers in alternating directions could lead to a reduction in the sensitivity to damage of the top resistance measurement. In order to better observe the influence of damage on the electrical response, 3-D color banded contour plots of current density magnitude and voltage potential were illustrated in Figure 5. 5 and Figure 5. 6 for multiple specimen configurations.

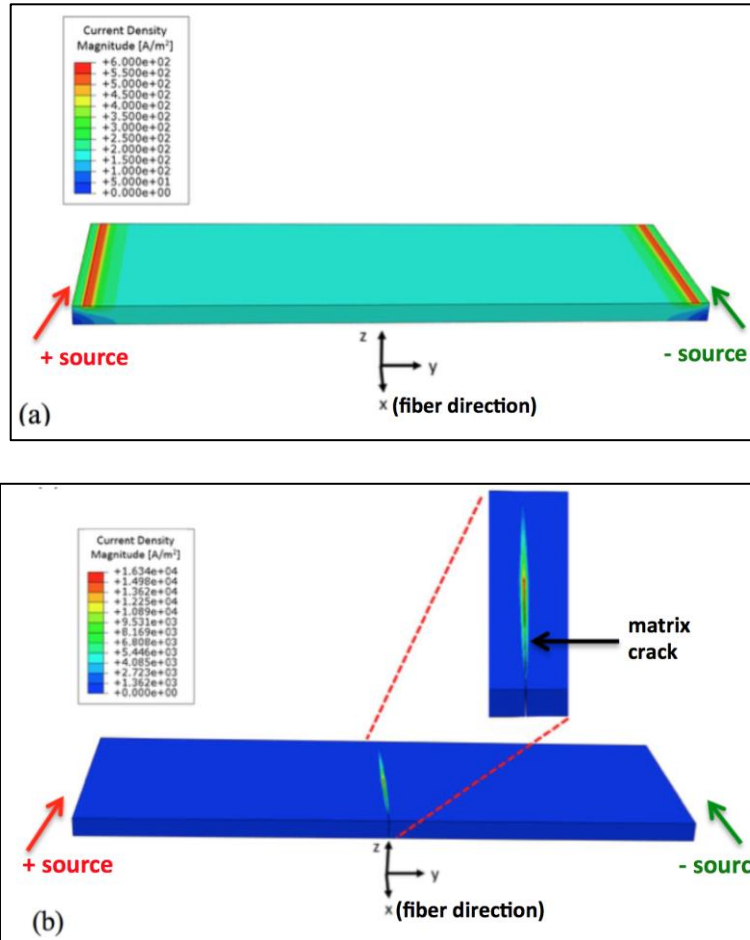


Figure 5. 5. Finite element plots of current density magnitude for 16-U-T specimens with (a) no damage and (b) a side matrix crack.

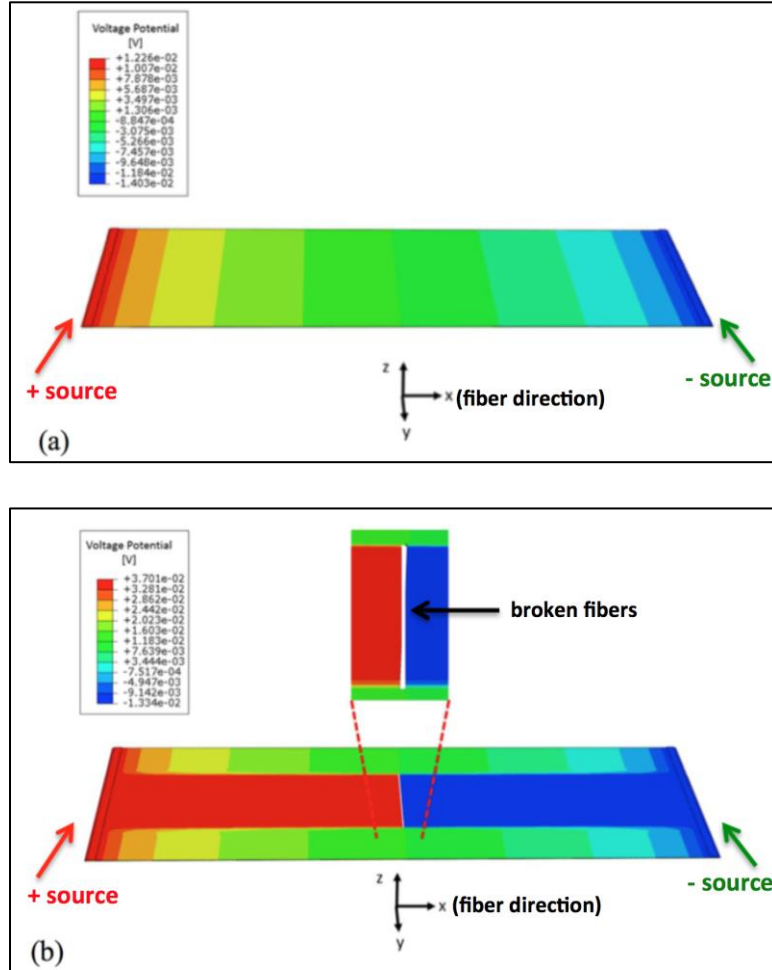


Figure 5. 6. Finite element plots of voltage potential for 16-U-F specimens with (a) no damage and (b) center-thru fiber breakage.

The current density was plotted for the 16-U-T specimen with no damage and with a side matrix crack in Figure 5. 5 (a) and (b), respectively. For the undamaged state, the current distribution was uniform through the bulk of the specimen, however areas of high and low current density were observed towards the outer edges near the electrodes. Moreover, for the undamaged specimen, the current distribution was constant when moving along the x-direction, meaning that the response was essentially 2-D for the undamaged state due to symmetry. When introducing a matrix crack in the side of the



specimen, however, the current density became highly concentrated around the crack tip as the current was forced around the crack. The current density near the crack tip at the center of the CFRP specimen was  $1.634 \times 10^4 \text{ A/m}^2$  compared to approximately  $1.5 \times 10^2 \text{ A/m}^2$  for the undamaged state. Despite this drastic increase in current density at the center, the side crack only led to an increase in resistance of 0.5% over the undamaged state in this specimen, evidenced in Table IV and Figure 5. The explanation for this phenomenon is readily apparent when considering the fiber orientations and resulting directional electrical conductivities of the specimen.

For the 16-U-T specimen with the side matrix crack, the crack occurred in the direction of the fibers (x – direction) and in between the fibers. As the electrical current flowed in the transverse direction (y – direction) between the electrodes and approached the crack, it had to modify its path to flow around the damaged region. The electrical current was forced to flow in the x – direction around the crack so that it could reach the other side. The electrical conductivity in the x – direction was significantly higher compared to the y – direction which meant that as the current modified its path, this was a path of relatively low resistance, which is supported by the miniscule 0.5% increase in resistance observed. Comparatively, for the specimens 16-U-T with the top and bottom matrix cracks, the current was forced to flow around the crack in the through thickness direction (z – direction), which had very low electrical conductivity. In these cases, the path of current flow around the crack had relatively high resistance supported by the increase in resistance measurement of up to 17% for the top matrix crack.

When considering the voltage potential distribution, most simulations had distributions similar to Figure 5. 6 (a) for specimen 16-U-F with no damage. The voltage

distribution was symmetric about the  $y - z$  plane at the center of the specimen and was also constant when moving along the  $y -$  direction. The introduction of center-thru fiber breakage in Figure 5. 6 (b) led to a significantly different response in voltage distribution. The voltage was no longer constant in the  $y -$  direction and there was significantly higher voltage on each side of the damaged area all the way from the center of the specimen out to the electrodes (Note that for these non-symmetric results, the voltage used in resistance calculation was the average voltage along the electrode in the  $y -$  direction). This dramatic change in voltage distribution could again be explained through consideration of the directional electrical conductivities. In this specimen the current flowed primarily in the  $x -$  direction with very high conductivity. The presence of the damage halted the local flow of current in the  $x -$  direction and forced the current flow towards either side of the damage in the  $y$ -direction, which had very low conductivity. The center-thru fiber breakage not only led to this unique potential gradient, but also contributed to the highest increase in top resistance measurement of 691% over the undamaged state.

### 5.2.2 FE Results: Prescribed Delamination

Upon observing the top and oblique resistance results in Table 5. 4. and Figure 5. 7. some noteworthy trends are uncovered. Similar to the previous results for thru fiber breakage, the delamination caused a non-uniform gradient across the specimen in the  $y$ -direction, therefore in order to obtain the resistance measurements in Table 5. 4., the voltage measurements were averaged across the sensing electrodes in the  $y$ -direction. For the 16-Q-T specimen, the delamination damage caused an increase in both top and oblique resistance for all simulations. The top resistance increased by 5%, 13%, and 47%

for small, moderate, and large delaminations when compared to the undamaged simulation. Oblique resistance increased by 4%, 13%, and 82% respectively. As the thickness increased from 16 plies to 32 plies, overall the 32-Q-T specimen were less sensitive to the delamination damage. Top resistance increased by 5%, 6%, and 25% for small, moderate, and large damage compared to the control. Similarly, oblique resistance increased by 1%, 7%, and 45% due to the increasing intensity of damage. Figure 5. 8. shows contour plots of voltage potential for top and oblique test simulations. These voltage potential plots were typical for these simulations in that the voltage was slightly more concentrated near the delaminated regions, which caused a slight non-uniformity in the contour lines across the specimen. Generally, the 16-X-T specimen sensitivity was comparable to the 16-Q-T specimen, however the cross-ply specimen was slightly more sensitive when using top resistance, but slightly less sensitive when using oblique measurement plane.

Table 5. 4. Finite Element Results for Electrical Resistance Due to Delamination Using 4-probe Method

Specimen Type	Damage Mode	ABAQUS $R_{top}$ [Ohm]	ABAQUS $R_{obl}$ [Ohm]
16-Q-T	None	6.56E-03	1.12E-02
	Small Delamination	6.89E-03	1.17E-02
	Moderate Delamination	7.40E-03	1.26E-02
	Large Delamination	9.67E-03	2.03E-02
16-X-T	None	6.65E-03	1.18E-02
	Small Delamination	7.03E-03	1.23E-02
	Moderate Delamination	7.10E-03	1.29E-02
	Large Delamination	1.09E-02	2.03E-02
32-Q-T	None	6.52E-03	2.40E-02
	Small Delamination	6.83E-03	2.42E-02
	Moderate Delamination	6.91E-03	2.57E-02
	Large Delamination	8.15E-03	3.48E-02

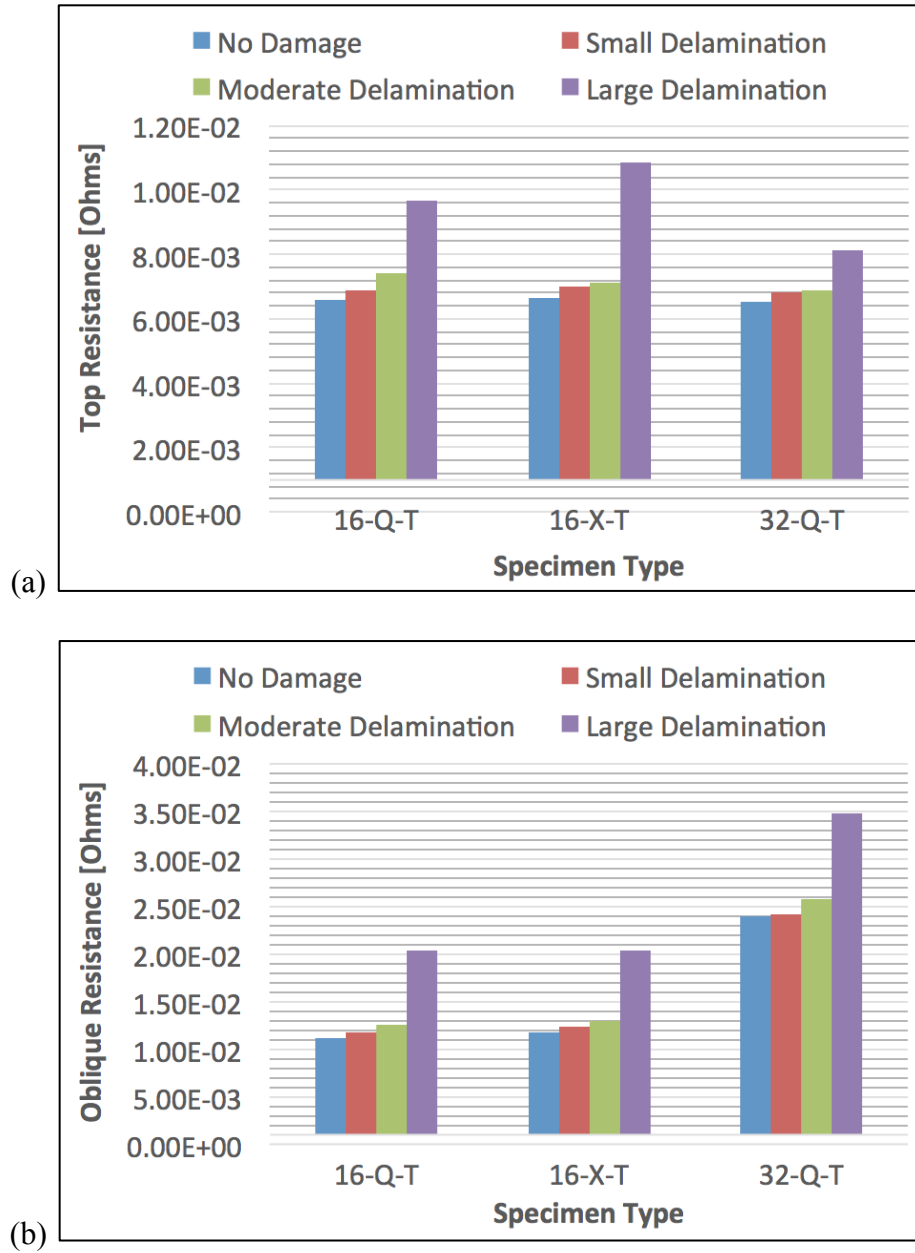
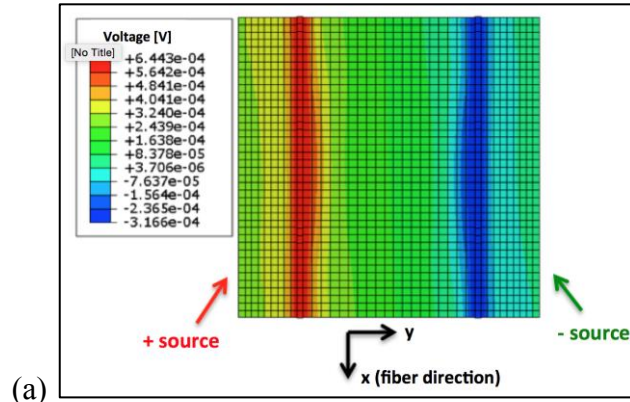
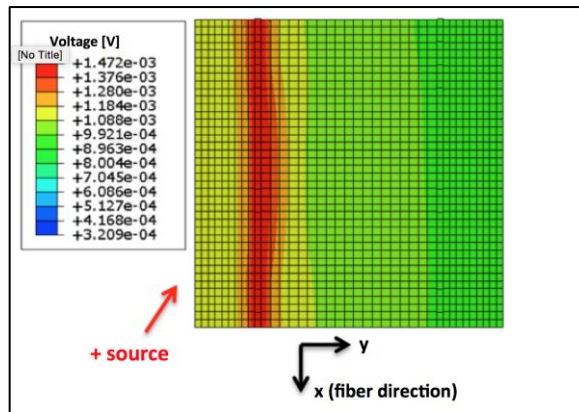


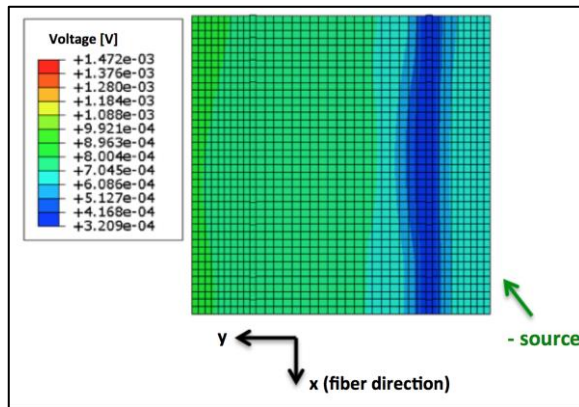
Figure 5. 7. Finite element simulation results of (a) top resistance and (b) oblique resistance for specimens with none, small, moderate, and large delamination.



(a)



(b)



(c)

Figure 5. 8. Finite element simulation results of (a) top resistance on top surface, (b) oblique resistance on top surface, and (c) oblique resistance on bottom surface for 32-Q-T specimen type.

For the square 152.4 x 152.4 mm AS4/3501-6 specimens used in the delamination feasibility study, the current penetrated through the thickness of the specimen, but this

was not the case for the IM7/977 specimens in section 5.2.1. For these other specimens, in the top resistance test, current only penetrated through a thin surface thickness. In order to fully take advantage of the predictive capabilities of the newly developed models, the electrical properties of these IM7/977 specimens were optimized such that linear response could be achieved through the full thickness of the specimen even in tests with current flowing primarily in the fiber direction.

### 5.3 Optimization of Electrical Properties Based on Material

#### Thickness: FE Results

In the current study, the electrical FE models only consider Ohmic current-voltage response within the effective thickness of the CFRP specimen. Therefore, in order for the 4-probe resistance to provide sensitive response to damage throughout the full specimen thickness, the material properties were optimized such that the effective thickness was equal to the physical specimen thickness. In order to distinguish the simulations for the optimized material properties, an additional term was added to the end of the specimen label to indicate the new material. For instance, specimen 16-U-T-Opt refers to a 16-ply unidirectional specimen with current flow transverse to fiber direction with optimal material properties. The optimal material properties in Table 4. 7. were calculated for 16-U and 32-U specimens with varying thickness and a summary of FE results are tabulated in Table 5. 5. Similar to the previous models, the properties for the 16-X-Opt simulations were assumed based on the 16-U-Opt material.

Noteworthy changes in material response were observed when reviewing the influence of damage on electrical response in Table 5. 5. For example, for the specimen 16-U-F-Opt, the center- top fiber breakage resulted in an increase in resistance of 52%

Table 5. 5. Finite Element Results for Electrical Resistance using Optimized Electrical Properties

Specimen Type	Damage Mode	ABAQUS Rtop [Ohm]
16-U-F-Opt	None	1.08E-02
	Center-Top Fiber Breakage	1.65E-02
	Center-Bottom Fiber Breakage	1.28E-02
	Center-Thru Fiber Breakage	5.80E-02
32-U-F-Opt	None	5.85E-03
	Center-Top Fiber Breakage	8.14E-03
	Center-Bottom Fiber Breakage	7.23E-03
	Center-Thru Fiber Breakage	1.96E-02
16-X-T-Opt	None	2.25E-02
16-X-F-Opt	None	2.37E-02

compared to only 38% for the specimen 16-U-F with non-optimal properties. Moreover the center-bottom fiber breakage led to a resistance increase of 19% compared to 14% for the specimen 16-U-F. The center-through fiber breakage resulted in an increase in resistance of 437% compared to 691% for the previous simulation. Although the magnitude of the resistance change declined, the overall change was more than sufficient for sensing the presence of the damage. Similar response was observed in the 32-U-F-Opt simulations where center-top, center-bottom, and center-thru fiber breakage resulted resistance increases of 39%, 24%, and 235%, respectively. These results are very encouraging for two primary reasons. First, the results suggest potential for improving sensitivity of resistance-based damage sensing through targeting optimal material properties for a specific CFRP laminate. Moreover through optimizing the electrical conductivity, Ohmic response, and thus sensitivity to damage, is achieved through the entire thickness of the model. This was not the case with the original material, where the model was only able to sense damage that was present within the small effective thickness, which was less than the thickness of the top layer. In the optimized model,

however, the electrical response was sensitive to fiber breakage throughout the full thickness of the laminate.

Another very interesting phenomenon was observed in the results for the cross-ply models. Due to the optimized properties, the current was expected to penetrate through the full thickness of the laminate, therefore all 16 layers needed to be included in the model. In the 3-D color banded contour plot of current density magnitude in Figure 5. 9., it can be seen that the current clearly penetrates through all 16 layers of the CFRP laminate. Moreover, the current was more highly concentrated in the layers in which the fiber direction corresponded to the x – direction coordinate whereas less electric current was concentrated in the layers with transverse orientation. This illustration shows that the current will not only penetrate through the thickness of the specimen but as the current flows in the longitudinal direction, it will find the least resistive path, which in this case corresponds to the fiber direction. This result could be used to inform the CFRP stacking sequence and/or optimal placement of highly conductive smart layers such as carbon nanotube buckypaper or graphene to achieve a desired response.

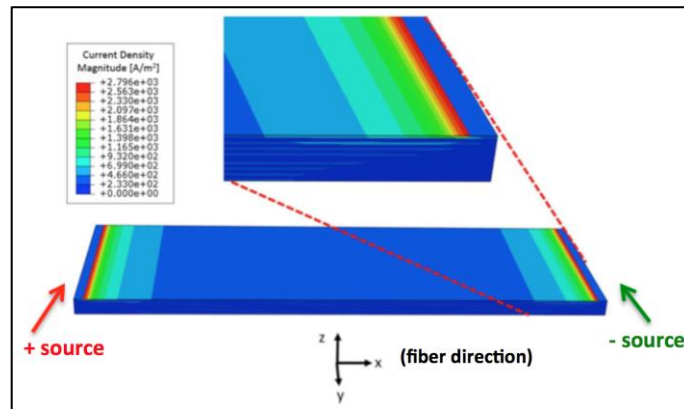


Figure 5. 9. Finite element plot of current density magnitude for 16-U-F-Opt specimen with no damage.



#### 5.4 Damage Sensing Feasibility Study: Summary

Throughout the damage sensing feasibility study of Chapter 5, several general conclusions were made. The top resistance measurement was generally found to be more sensitive to fiber breakage compared to matrix cracking. It was demonstrated, however, that several factors affect the sensitivity of the response to damage including: (i) orientation of the fibers relative to the line of current probes, (ii) location of the damage, and (iii) type of damage. The material properties were then optimized such that Ohmic response was achieved throughout the full thickness of the CFRP specimen. With the use of optimal electrical conductivity, the model became even more sensitive to fiber breakage near the top and bottom surfaces of the specimen.

This feasibility study also suggests that the top resistance plane may actually provide a sensitive response to delamination; if the effective thickness is large enough that the current penetrates through the full thickness of the specimen. The conclusion made by previous literature could have been based on experiments in which the effective thickness was very small and thus delamination was not captured in the response. In addition, this study confirms the findings of previous studies that as the magnitude of the damage increases, oblique electrical resistance increases as well.

## CHAPTER 6: QUASI-STATIC MODELING OF LOW-VELOCITY IMPACT-INDUCED DELAMINATION

The purpose of the quasi-static impact modeling chapter was to develop realistic delamination patterns for the purpose of expanding the electrical resistance-based damage sensing models to more practical applications. In order to achieve this end goal, several intermediate objectives needed to be satisfied beforehand. The objectives of the quasi-static impact modeling included: (i) development of quasi-static FE models for predicting the stress state in CFRP laminates subjected to low-velocity impact (section 6.1), (ii) predict delamination failure based on a two-step theory, (iii) plot the delaminated interfaces in Matlab, (iv) validate the length of the delaminated regions versus published data by Moura et al [3] (section 6.2), (v) perform simulations on cross-ply and quasi-isotropic specimens from the experimental impact characterization section 4.8, and (vi) compare the delamination predictions of 32-ply cross-ply specimens to CT image data from Demerath [50]. Initially, quasi-static FE models were created in ABAQUS to replicate the published results of Moura et al [3] before expanding to new composite laminates.

6.1 Development of Quasi-Static Models for Low-Velocity  
Impact-Induced Delamination of CFRP laminates

6.1.1 Prediction of Delamination Using Quasi-Static Impact

Modeling: Theory

Following the methodology of Moura et al [3], low-velocity impact models were developed in ABAQUS for the purpose of predicting damage in carbon-epoxy composites. In order to validate the models, results were compared to published results of ICI Fib 150/42  $[0_2/+45_2/-45_2/90_2]_2$  specimens [3]. The specimens were thin, 60mm x 60mm square-shaped plates. The specimens were clamped such that a circular section with diameter of 50mm was exposed. The Moura paper did not detail the thickness of the laminate, so the thickness was assumed to be 2.3 mm, which is typical for similar 16-ply CFRP laminates. The geometry was modeled using the 8-node S8R shell element, as shown in Figure 6. 1.

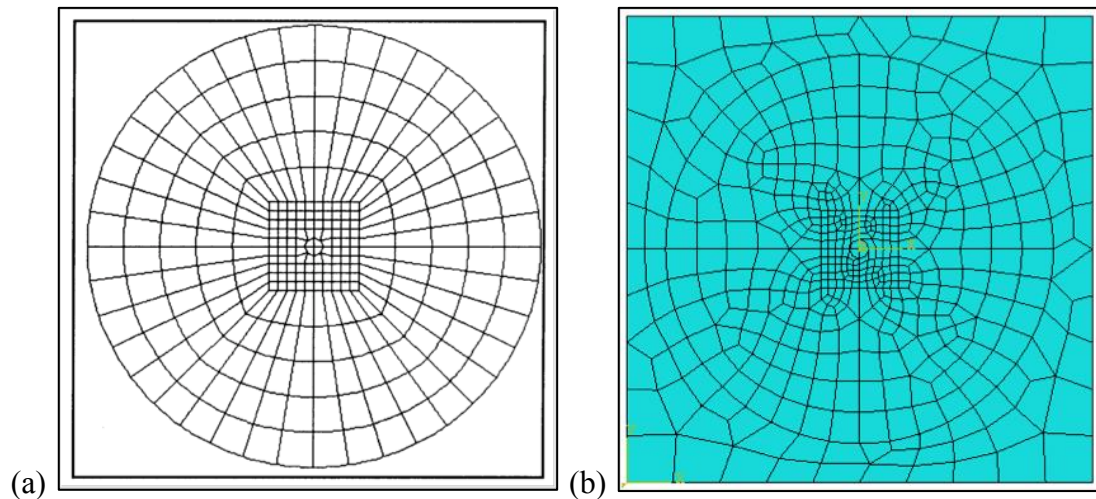


Figure 6. 1. Mesh for quasi-static impact model by (a) Moura et. al [3] and (b) current study.

With the S8R element, shear stress continuity is maintained between adjacent plies. In order to reduce the effects of shear stiffening, the element formulation employs a reduced-integration technique. For the purpose of predicting matrix cracks and delamination, a quasi-static loading approach was utilized (i.e. damage is predicted using only the peak impact load and not rate-dependent). The load was distributed over the center 4 elements using a static-general load step. The surface of the 50mm circular area was clamped to restrict displacement in the z-direction. In addition, the plate was constrained so that the plate was not allowed to rotate about the z-axis. The static loading and boundary conditions are displayed in Figure 6. 2.

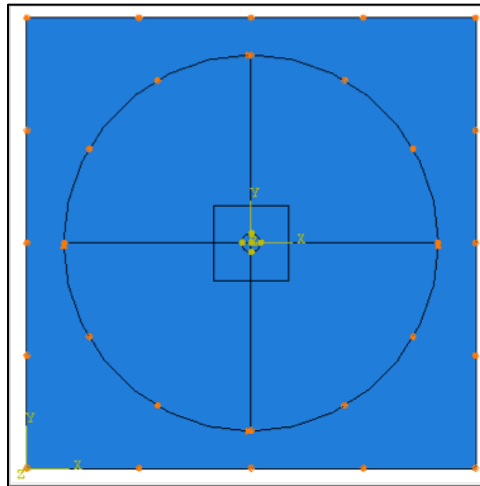


Figure 6. 2. Boundary conditions and loads for quasi-static impact model.

A two-step failure criterion was employed for analyzing failure on a ply-by-ply basis. Moura et al [3] developed the failure criteria by using a combination of the methods from Tsai-Wu, Hashin, Choi, and Becker [65–68] as well as information gathered from empirical study. Based on the results of Choi [68], delamination occurs at

the interface between plies with different fiber orientations and is caused by matrix cracking within the adjacent plies. The first step in the failure analysis was to predict the presence of matrix cracks within the plies using the following failure criterion:

$$\left(\frac{\sigma_2}{Y_{t,c}}\right)^2 + \left(\frac{\tau_{23}}{S_i}\right)^2 = 1 \quad (6.1)$$

where  $\sigma_2$  is the second principle stress,  $\tau_{23}$  shear stress in 2-3 plane,  $Y_{t,c}$  is the material strength in the 2-direction (tension or compression depending on the sign of  $\sigma_2$ ), and  $S_i$  is the material shear strength. If matrix cracking was predicted within a ply, then the second step was to perform delamination analysis on the adjacent ply. For interior plies, the delamination analysis was performed at the interface between the two differently oriented plies using stresses on the side of the lower ply. For the lowest ply (furthest from the impacted surface), the delamination was performed using stresses at the interface on the side of the upper adjacent ply. The delamination was predicted using the following expression:

$$\left(\frac{|\sigma_1^*|}{X_{t,c}}\right) + \left(\frac{\sigma_1^*}{X_{t,c}}\right)^2 + \left(\frac{|\sigma_2^*|}{Y_{t,c}}\right) + \left(\frac{\sigma_2^*}{Y_{t,c}}\right)^2 + \left(\frac{2|\sigma_1^*\sigma_2^*|}{X_{t,c}Y_{t,c}}\right) + \left(\frac{|\tau_{13}|_n}{S_i}\right) + \left(\frac{\tau_{13n}}{S_i}\right)^2 = 1 \quad (6.2)$$

where  $\sigma_1^*$  and  $\sigma_2^*$  are principle stresses,  $\tau_{13}$  is transverse shear stress in 1-3 plane,  $X_{t,c}$  is the material strength in tension/compression in the 1-direction. The difference between the expression (6.2) and the delamination equation of Moura et al [3] was that in expression (6.2), the  $\sigma_1^*$  was compared to the material strength in fiber direction ( $X_{t,c}$ ), following the Hashin criteria [66].

## 6.1.2 Prediction of Delamination Using Quasi-Static Impact

### Modeling: Development of FE Models

The methods of 6.1.1. were applied to develop additional quasi-static impact damage models for low-velocity impact specimens in Table 6. 1. Low velocity impact experiments had been previously performed on 16 - and 32 – ply CFRP specimens with unidirectional, symmetric cross-ply, and quasi-isotropic layup arrangements. The 16-U, 32-U, 16-X, 32-X, 16-Q, and 32-Q specimens were cut to dimensions of 152.4 x 152.4 mm and clamped within a test fixture with a square 127.0 x 127.0 mm opening. Figure 6. 3. shows a side by side comparison of the physical test fixture and the FE boundary conditions for the low-velocity impact specimens. The CFRP specimens were meshed using the S8R shell elements, as shown in Figure 6. 4.

Table 6. 1. Quasi-Static Impact Modeling Parameters (Note: Impact Energy And Velocity Are For Reference Only And Not Used In Quasi-Static Models)

Specimen ID	Material	Striker Type	Peak Load [N]	Impact Energy [J]	Impact Velocity [m/s]
Moura	ICI Fib 150/42	12.7mm round	2958	N/A	N/A
16-X	IM7/977-2	12.7mm flat	9831	38.40	2.43
32-Q-Low	AS4/3501-6	12.7mm round	8190	19.90	2.54
32-Q-Int	AS4/3501-6	12.7mm round	9020	23.02	2.73
32-Q-High	AS4/3501-6	12.7mm round	9620	27.16	2.97
16-Q-Low	AS4/3501-6	12.7mm round	3270	7.19	1.53
16-Q-Int	AS4/3501-6	12.7mm round	3320	8.67	1.68
16-Q-High	AS4/3501-6	12.7mm round	3280	10.23	1.82
32-X-Low	IM7/977-3	12.7mm round	7786	18.93	1.72
32-X-Int	IM7/977-3	12.7mm round	9253	28.29	2.10
32-X-High	IM7/977-3	12.7mm flat	11748	28.42	2.10

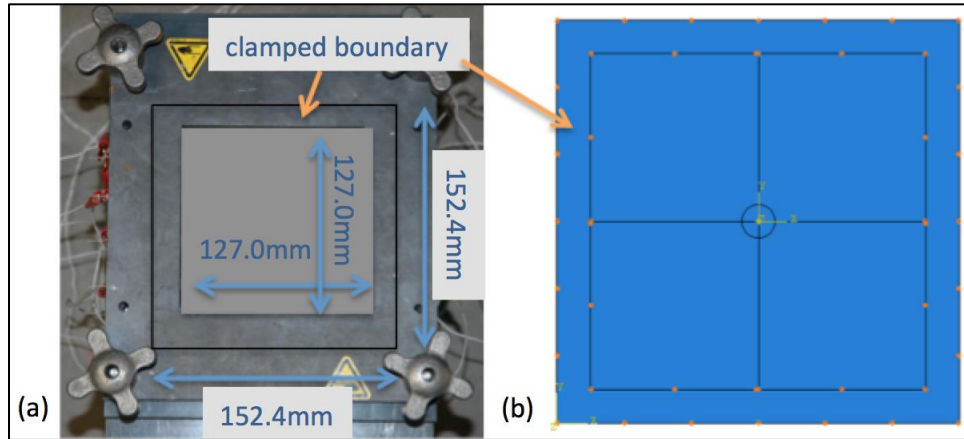


Figure 6. 3. (a) Low-velocity impact test fixture and (b) FE boundary conditions and loads for quasi-static impact models.

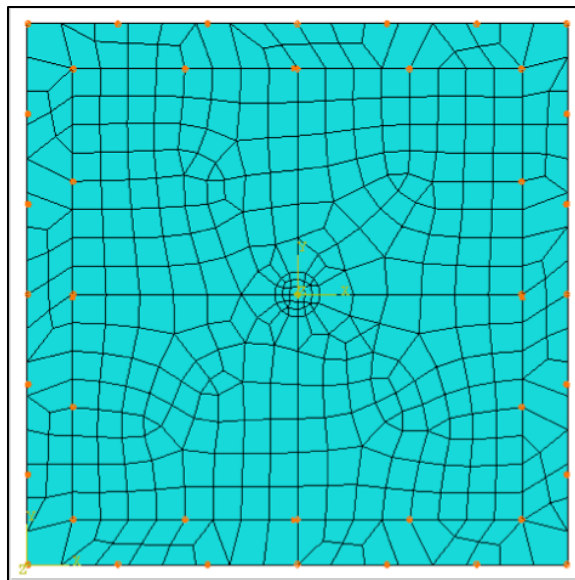


Figure 6. 4. Mesh for quasi-static impact models.

The peak impact load was applied to each model systematically depending on the type of impact striker used in the experiment. For specimens 32-X, 16-Q, and 32-Q, low-velocity impact tests were performed using a steel 12.7mm radius hemispherical-tipped

striker. For specimens 16-U, 32-U, and 16-X on the other hand, low-velocity impact testing was conducted using a plastic Delrin® 12.7mm radius flat-ended striker tip. The type of striker tip used has a significant influence on the impact response, due to differences in the concentration of impact load and transfer of impact energy (vibrations, impact absorption, etc.). For example, for the steel hemispherical-tipped striker, the load becomes highly concentrated at the tip of the striker. Conversely, with the plastic flat-ended striker, as the CFRP specimen deflects, the load actually becomes concentrated around the perimeter of the striker, as shown in Figure 6. 5. (a). At the center of the striker, the specimen and striker actually lose contact. In order to properly model the striker-specimen contact, contact theory was employed. Based on Hertzian contact theory [69], the contact radius for the hemispherical-tipped striker was determined by the equation:

$$a = \left( \frac{3Fr \left( \frac{1 - \nu_1^2}{E_1} + \frac{1 - \nu_2^2}{E_2} \right)}{4} \right)^{\frac{1}{3}} \quad (6.3)$$

where  $a$  is radius of contact (m),  $F$  is contact force (N),  $r$  is radius of contacting sphere (m),  $\nu$  is Poission's ratio of bodies 1 and 2, and  $E$  is elastic modulus (Pa) of bodies 1 and 2. For the steel hemispherical-tipped striker in contact with a CFRP laminate, the contact radius was approximately 6.83E-3 m (given:  $F = 7786$  N,  $r = 0.00635$ ,  $E_1 = 2.068E11$  Pa,  $E_2 = 2.161E11$  Pa,  $\nu_1 = 0.295$ ,  $\nu_2 = 0.318$ ). This contact radius corresponded to application of a static impact load applied at the center 5 nodes in the FE model, as shown in Figure 6. 5. (b). Impact simulations were performed for impact loading conditions given in Table 6. 1., and nodal stress results were exported at each interface in order to evaluate damage using equations (6. 1) - (6. 2).



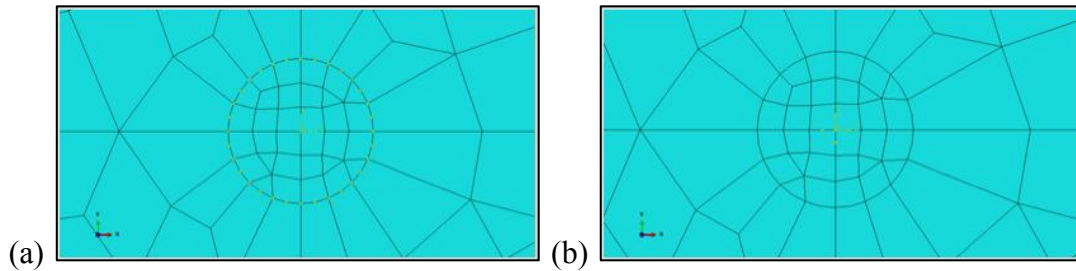


Figure 6. 5. Location of static impact load for 12.7 mm radius (a) Delrin ® flat-ended and (b) steel hemispherical striker.

The next step in the modeling process was to compile the necessary mechanical properties for the FE analysis. For the S8R shell element with orthotropic material properties, ABAQUS requires the following parameters: density ( $\text{kg/m}^3$ ), elastic modulus ( $E_{11}$  and  $E_{22}$  in Pa), Poisson's ratio ( $\nu_{12}$ ), and shear modulus ( $G_{12}$ ,  $G_{13}$ , and  $G_{23}$  in Pa). Generally, only constituent material properties (fiber/matrix) are published in material datasheets, thus in order to determine the appropriate composite properties, basic theory was employed. Knowing the proportions of fibers and matrix in a given composite, the mechanical properties can be approximated using the properties of the individual constituents and a set of special relations, generally referred to as the “rule of mixtures.” The fiber and matrix constituent properties were gathered from material datasheets [53–56,64] in Table 6. 2. The resulting composite material properties were then calculated using the following equations (6. 4) - (6. 11).

Table 6. 2. Quasi-Static Impact Modeling Parameters (Note: Impact Energy And Velocity Are For Reference Only And Not Used In Quasi-Static Models)

<b>Constituent Properties</b>			
<b>Material Property</b>	<b>IM7/977-2</b>	<b>IM7/977-3</b>	<b>AS4/3501-6</b>
Fiber % / Matrix%	78%/22%	78%/22%	61.5%/38.5%
$\rho_f / \rho_m$ [kg/m <sup>3</sup> ]	1780/1310	1780/1310	1790/1265
$E_f / E_m$ [Pa]	2.76E+11/3.52E+09	2.76E+11/3.52E+09	2.31E+11/4.24E+09
$\nu_f / \nu_m$	0.3/0.384	0.3/0.384	0.3/0.384
<b>Composite Properties</b>			
<b>Material Property</b>	<b>IM7/977-2</b>	<b>IM7/977-3</b>	<b>AS4/3501-6</b>
$\rho$ [kg/m <sup>3</sup> ]	1676.6	1676.6	1587.9
E11 [Pa]	2.161E+11	2.161E+11	1.437E+11
E22 [Pa]	1.530E+10	1.530E+10	1.070E+10
$\nu_{12}$	0.318	0.318	0.333
G12 [Pa]	5.540E+09	5.540E+09	3.872E+09
G13 [Pa]	5.540E+09	5.540E+09	3.872E+09
G23 [Pa]	5.220E+09	5.220E+09	3.700E+09
Xt [Pa]	2.723E+09	2.723E+09	2.205E+09
Xc [Pa]	1.689E+09	1.689E+09	1.530E+09
Yt [Pa]	1.11E+08	1.11E+08	8.10E+07
Yc [Pa]	1.11E+08	1.11E+08	8.10E+07
Si [Pa]	1.28E+08	1.28E+08	1.28E+08

$$E_{11} = E_f \nu_f + E_m \nu_m \quad (6.4)$$

$$E_{22} = E_{33} = \frac{E_f E_m}{\nu_m E_f + \nu_f E_m} \quad (6.5)$$

$$\nu_{12} = \nu_{13} = \nu_f \nu_f + \nu_m \nu_m \quad (6.6)$$

$$G_{12} = G_{13} = \frac{G_f G_m}{\nu_m G_f + \nu_f G_m} \quad (6.7)$$

$$\xi \approx 1 + 40 v_f^{10} \quad (6.8)$$

$$\eta \approx \frac{\frac{v_m}{v_f} - 1}{\frac{v_m}{v_f} + \xi} \quad (6.9)$$

$$v_{23} = \frac{v_m(1 + \xi \eta v_f)}{1 - \eta v_f} \quad (6.10)$$

$$G_{23} = \frac{E_{22}}{2(1 + v_{23})} \quad (6.11)$$

where E is stiffness modulus (Pa),  $v$  is volume fraction of fibers/matrix,  $\nu$  is Poission's ratio, G is shear modulus (Pa), and  $\xi$  and  $\eta$  are dimensionless parameters used for determination of  $v_{23}$  [70]. The material strengths  $X_t$ ,  $X_c$ ,  $Y_t$ ,  $Y_c$ , and  $S_i$  were taken directly from typical composite laminate values from the material datasheets [53–56,64]. In order to validate the models, damage analysis was first performed for an impact load of 2958 N for ICI Fib 150/42 [ $0_2/+45_2/-45_2/90_2$ ] specimens and compared to the published results of Moura et al [3].

## 6.2 Quasi-Static Models for Low-Velocity Impact-Induced Delamination of CFRP laminates: Results

### 6.2.1 Results: Validation of FE Models Versus Literature

For the ICI Fib 150/42  $[0_2/+45_2/-45_2/90_2]$  specimens in the Moura paper [3], delamination was plotted at all 6 interfaces between plies with varying fiber orientations. These 6 interfaces were labeled 1 – 6 with 1 being the interface closest to the impacted surface and 6 being the interface furthest from the impacted surface. When comparing the results, there are two primary differences in the Moura models and the models of the current thesis. First, in the Moura models, residual thermal stresses due to the manufacturing process were considered. The details of the thermal stress computations (i.e. coefficients of thermal expansion) were not provided in the paper, so it was not possible to reproduce the effects of the thermal stresses in the current models. Since thermal expansion is much greater in the 2-direction compared to the 1-direction (fiber-direction), it was expected that the width of the predicted delaminations in the 2-direction may not match between the two models, but the overall length of the delaminations in the 1-direction should be similar. Moreover, the Moura paper did not give information on the thickness of the specimens, so the thickness used in the current model was assumed from similar specimens and is unlikely to be the same thickness as the thickness used in the Moura models. In order to compare the delamination predictions between the current models and the Moura paper, the delamination predictions were plotted side by side for the Moura paper and current study in Figure 6. 6. Following the experimental work of Moura, delamination occurred at interfaces 2 – 6, but not at interface 1.

Since the current study did not account for thermal stresses, overall area could not be used to compare the delamination predictions. Instead, the length of the major axis (in direction of lower adjacent layer fiber direction) was used to compare the Moura models to the models of the current study, as listed in Table 6. 3. When comparing the length of the delaminations, the predictions for the Moura study and current study matched well at all interfaces, with a maximum variation of 7% at the 2<sup>nd</sup> interface. Overall, the error was considered to be within reason, bearing in mind that the current models did not consider thermal stresses, nor was the thickness of the Moura models known.

Table 6. 3. Comparison of Delamination Major Axis Length in the Direct of Carbon Fibers for Validation of Quasi-Static FE Models

<b>Interface #</b>	<b>Delamination Major Axis Length [mm]</b>	
	<b>Moura et al. FE Prediction</b>	<b>Current Thesis FE Prediction</b>
1	N/A	N/A
2	15.6	16.7
3	12.9	12.2
4	14.4	14.1
5	21.7	21.3
6	24.6	24.8

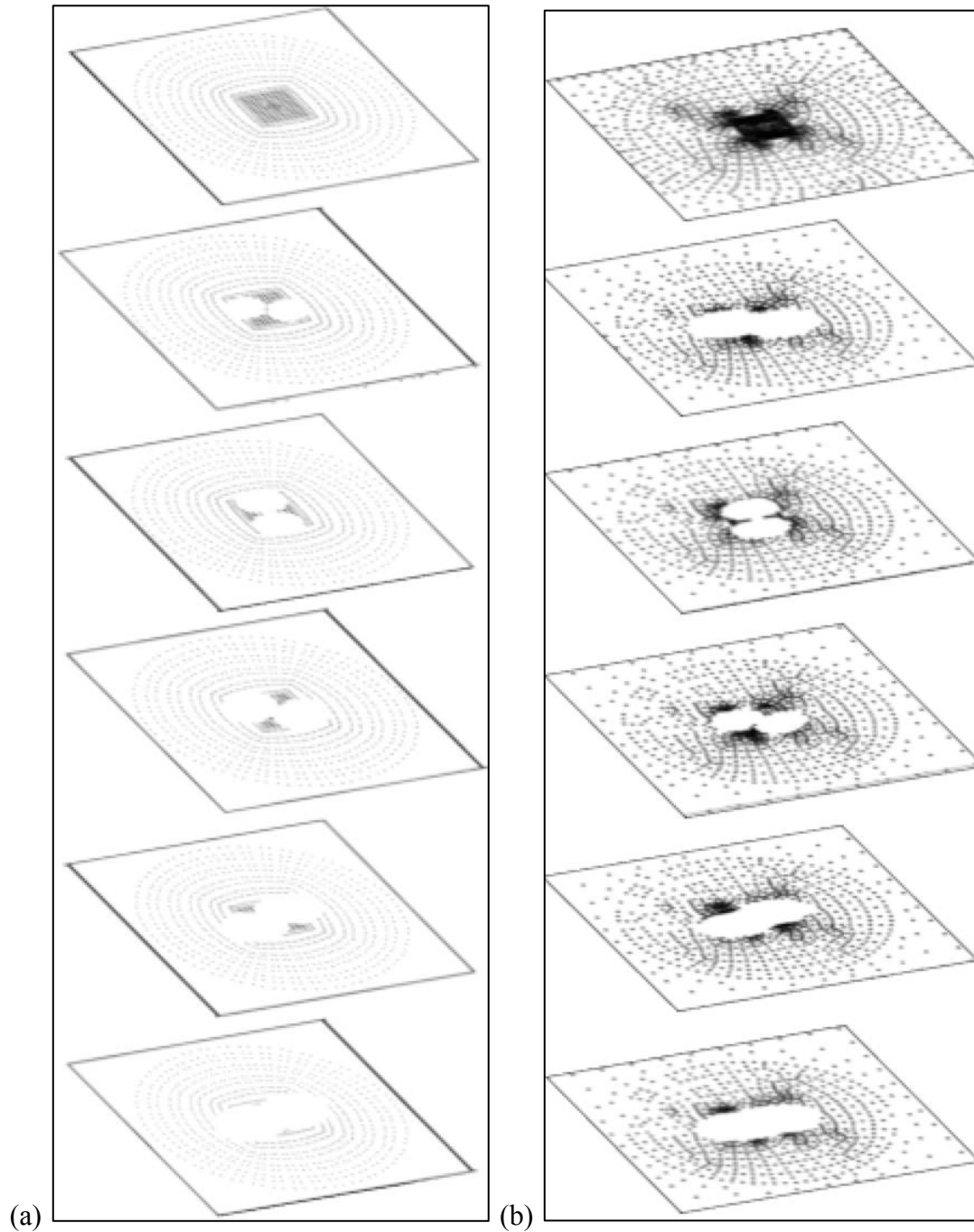


Figure 6. 6. Delamination Plots for interfaces in  $[0_2/+45_2/-45_2/90_2]_s$  laminate by (a) DeMoura [3] and (b) current thesis. Delamination at each ply is oriented with fiber direction of lower adjacent ply (top to bottom: 45,-45,90,-45,45,0).

### 6.2.2 Results: Prediction of Delamination for 16-X, 32-X, 16-Q, and 32-Q Specimens

Nine quasi-static impact models were created for 16-X, 32-X, 16-Q, and 32-Q specimens under various impact loading scenarios. The delamination predictions were plotted in Matlab for all interfaces, and the results are shown in Figure 6. 7. (a) – (i) for the interface furthest from the impacted surface. At first glance, the prediction of delaminated area was much greater for specimen 16-X compared to the other specimens. For this specimen, not only was there an elliptical delamination near the center of the specimen, but the delamination extended in a cross-shape pattern. This pattern is similar to CT image results for cross-ply specimens from Demerath [50]. The cross-shaped delaminations terminate near the clamped edges, which suggests that this pattern may be an artifact of constriction due to clamping the specimen in the test fixture. For specimens 16-Q-Low, 16-Q-Int, and 16-Q-High, the impact energy was increased progressively, however there was no definitive trend in neither peak impact load nor delamination prediction. This is due to the fact that the quasi-static impact models considered only peak impact load and not impact energy. For instance, both impact energy and peak load increased progressively for the 32-Q-Low, 32-Q-Int, and 32-Q-High specimens. When observing the corresponding delamination plots in in Figure 6. 7. (e) – (g), the size of the delamination increased progressively as well. Similar results were observed for specimens 32-X-Low and 32-X-Int in Figure 6. 7. (h) – (i).

In order to further analyze the 32-X specimens and validate the FE predictions, the delamination plots were compared to CT image results from the thesis of Demerath

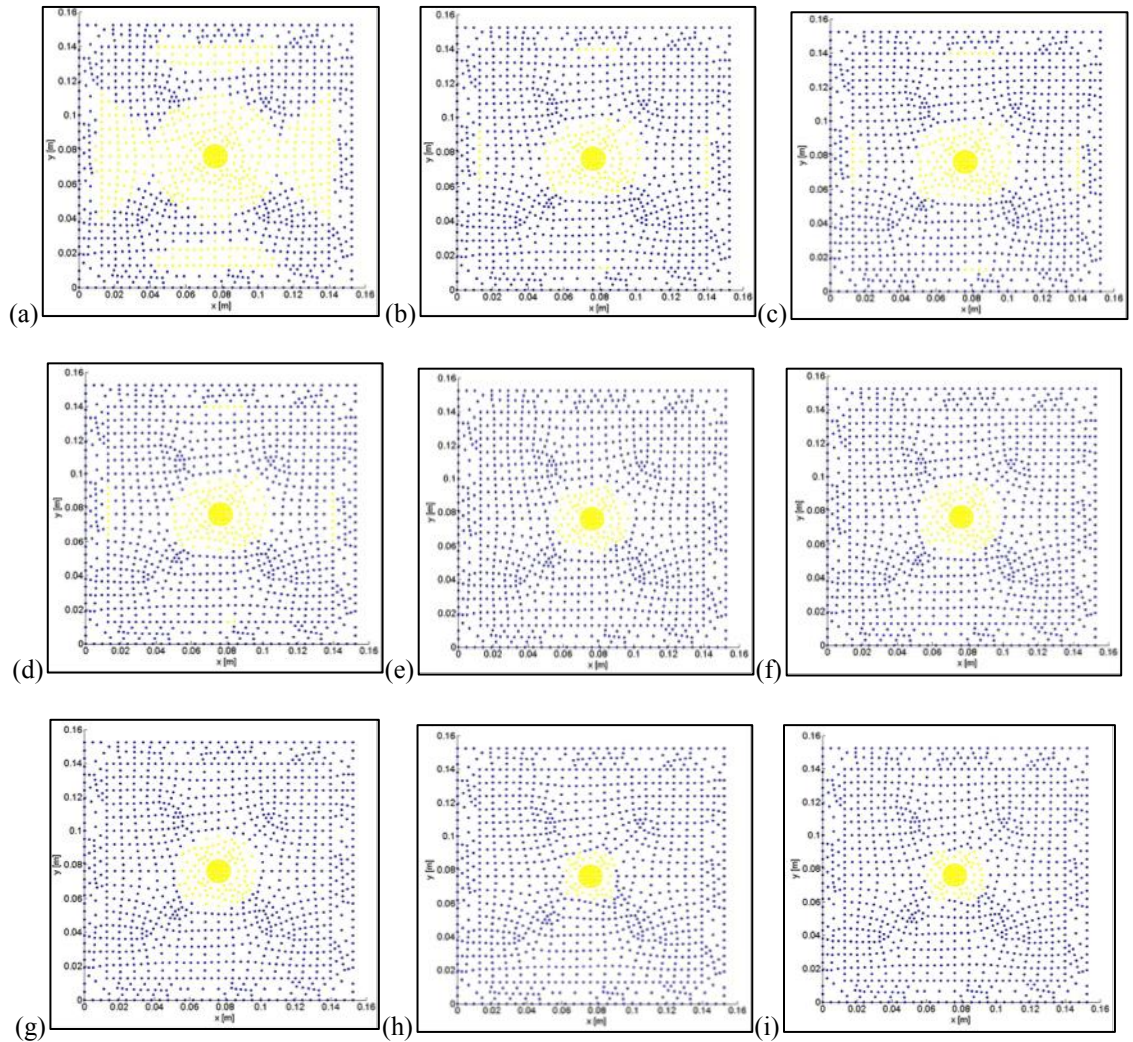


Figure 6. 7. Delamination plots at interface furthest from impact striker for (a) 16-X, (b) 16-Q-Low, (c) 16-Q-Int, (d) 16-Q-High, (e) 32-Q-Low, (f) 32-Q-Int, (g) 32-Q-High, (h) 32-X-Low, (i) 32-X-Int. Fiber direction of the lower-adjacent plies coincide with x-direction.

[50]. One noticeable difference between the FE predictions and CT image results was that for the FE predictions, the maximum length of the delaminated area was at the final interface 30, where as for the experimental CT specimens, the maximum delaminated interface was at interface 27 for specimen 32-X-Low and interface 26 for 32-X-Int. This



discrepancy was expected, however, because the quasi-static FE models did not take progressive failure into account, therefore the delamination was based only on static stress values alone. Based on beam theory, stresses are maximum at either the top or bottom surface, which supports the prediction of maximum delamination at the lowest interface 30. In order to further validate the models, the maximum length of the delamination major axis was compared between the FE models and CT scans in Table 6. 4. The CT scan and FE prediction differed by only 0.1mm, or 0.4%, for 32-X-Low at interface 27. For 32-X-Int at interface 26, the difference was only 2.2mm, or 6.2%. This deviation was considered acceptable due to the assumptions of the quasi-static method and the relatively large amount of noise/shadowing present in the CT scans. Side by side comparisons of delaminated predictions and CT image results are shown in Figure 6. 8 - Figure 6. 9.

Table 6. 4. Delamination Major Axis Length Comparison

Specimen ID	Interface #	Delamination Major Axis Length [mm]	
		Demerath CT Scan	Current Thesis FE Prediction
32-X-Low	27	27.6	27.7
32-X-Int	26	33.4	35.6

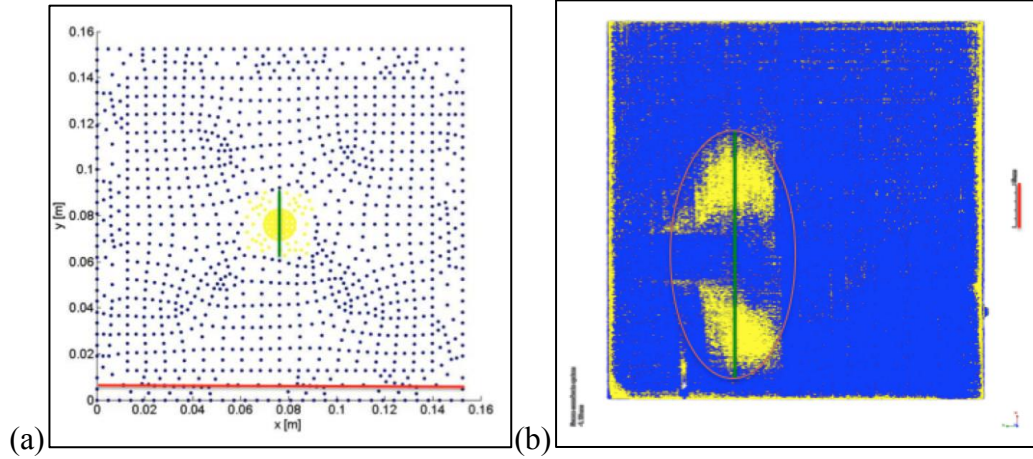


Figure 6. 8. Comparison of (a) FE delamination prediction and (b) CT image [50] at interface 27 for 32-X-Low specimen. (Note: FE plot in part (a) is full 152.4mm x 152.4mm specimen, whereas the CT image in part (b) is cropped to show detail in only a 45 mm x 45 mm section).

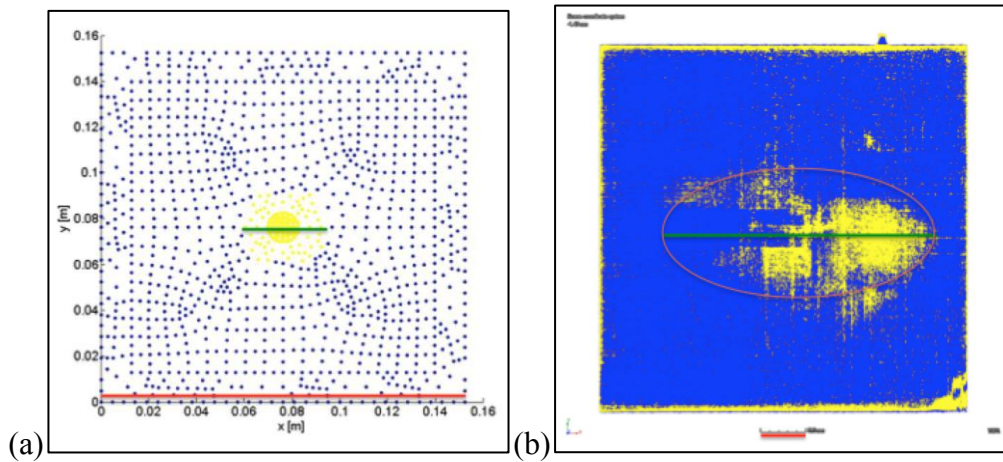


Figure 6. 9. Comparison of (a) FE delamination prediction and (b) CT image [50] at interface 26 for 32-X-Int specimen. (Note: FE plot in part (a) is full 152.4mm x 152.4mm specimen, whereas the CT image in part (b) is cropped to show detail in only a 45 mm x 45 mm section).

### 6.3 Quasi-Static Impact Modeling: Summary

In this chapter, quasi-static FE models were developed for predicting low-velocity impact-induced delamination in CFRP composite laminates. The FE models were built in ABAQUS using the S8R shell element, and the peak impact load was applied in a static load step. The delamination predictions were completed in a two-step process. First, matrix rupture in the inside layers was evaluated, and second, delamination analysis was performed at the corresponding interfaces. The FE models were compared to the literature and then applied to the experimental impact characterization specimens of section 4.8. The results demonstrated that the delamination was positively correlated with the peak impact load, and the delamination at each interface was oriented with the fiber direction of the lower-adjacent ply. Moreover, the FE predictions for select 32-ply cross-ply specimens were compared to CT image results available in the literature, and the length of maximum delamination compared very well between the FE predictions and experimental specimens. In order to round out the work of the current thesis, the simulation-based delamination patterns of the current chapter were then integrated into the electrical FE models for the purpose of electrical resistance-based damage sensing.

## CHAPTER 7: INFLUENCE OF SIMULATION-BASED DELAMINATION AND VOIDS ON ELECTRICAL RESISTANCE

In the previous chapter, delamination patterns were predicted for cross-ply and quasi-isotropic CFRP specimens using ABAQUS FE models. In addition, CT scans were performed on unidirectional specimens in order to characterize the content of voids due to manufacturing. The current chapter aimed to integrate these realistic damage and defect patterns into the electrical resistance-based damage sensing models. The objectives of this chapter included the following: (i) model simulation-based delamination predictions into electrical FE models in ABAQUS (section 7.1.1), (ii) observe the influence of the delamination damage on electrical resistance (section 7.1.2), (iii) compare the influence on electrical resistance for simulation-based impact damage versus experimental data from McAndrew [17,18], (iv) generate 3-D CT images of specimens with varying void contents (section 7.2.1), (v) transcribe the CT image voids into 3-D FE models (section 7.2.2), and (vi) observe the influence of void content on resistance transverse to fibers and through-thickness (section 7.2.3). The delamination predictions of the previous chapter were plotted onto grids using Matlab, which made the process of transcribing the damage onto the FE mesh methodical.

## 7.1 Correlation Between Simulation-Based Delamination and Resistance

### 7.1.1 Integration of Simulation-Based Delamination into FE Models: Methods

The development of the realistic damage sensing models followed the general 4-step procedure, shown in Figure 7. 1. First, from results of the quasi-static impact models, delamination was analyzed using the DeMoura [3] failure criteria. Second, at every interface between plies with different fiber orientations, delamination plots were created in Matlab. An example of an interface delamination plot is shown in Figure 7. 2. (a). Third, the delaminated areas in the Matlab plots were then discretized onto the mesh in the ABAQUS electrical FE Models. Figure 7. 2. (b) displays an example of a meshed interface for specimen 32-X-Low with the delaminated elements highlighted. A comparison of the delaminated interfaces from (a) a CT scan, (b) Matlab prediction, and (c) the ABAQUS electrical FE model are displayed in Figure 7. 3. Forth, once the delamination was integrated into the ABAQUAS FE models, top and oblique resistance simulations were performed for each damaged specimen.

In the damage sensing feasibility study, the delamination damage was considered severe enough that no current was allowed to flow across the delaminated surface. In the current study, however, the low-velocity impact was not considered especially severe and was performed at such energy that only barely visible impact damage was sustained. For such a scenario, it is reasonable to assume there may be some fiber to fiber contact occurring across the delaminated interface, which would allow current to flow across the

interface, but at a rate less than in an undamaged specimen. In this case, rather than reducing electrical conductivity to zero, the through-thickness conductivity of the damaged elements was reduced appropriately. This method follows the previous work of Pyrzanoski et al [26]. For the delaminated elements in the current study, the electrical conductivity in the through-thickness direction was reduced by a factor of two in order to represent of the reduction of contact between the adjacent plies.

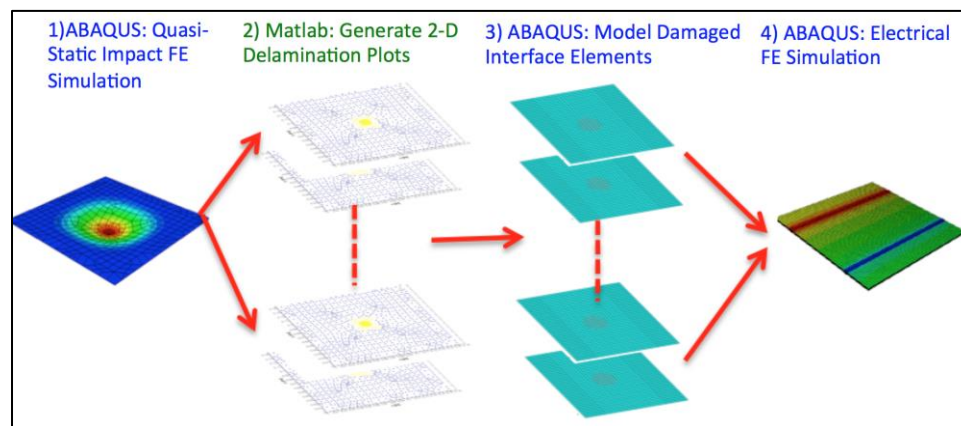


Figure 7. 1. 4-step procedure for incorporating simulation-based impact damage into electrical FE models.

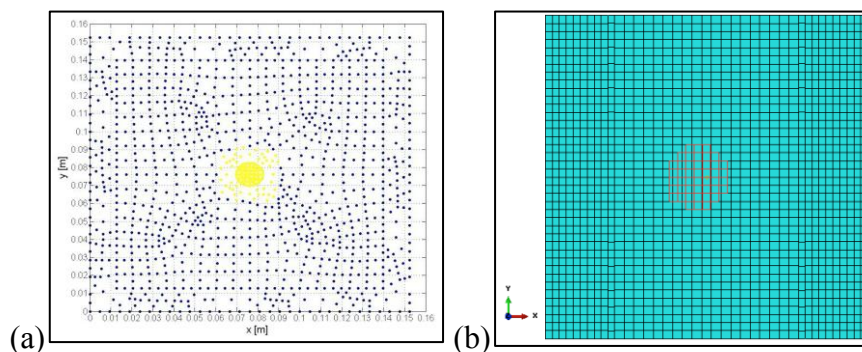


Figure 7. 2. (a) Matlab plot with delaminated area colored yellow and (b) ABAQUS Electrical FE Model with delaminated elements outlined in red for interface 1 for specimen 32-X-Low. Fiber direction of lower adjacent ply corresponds with x-axis.

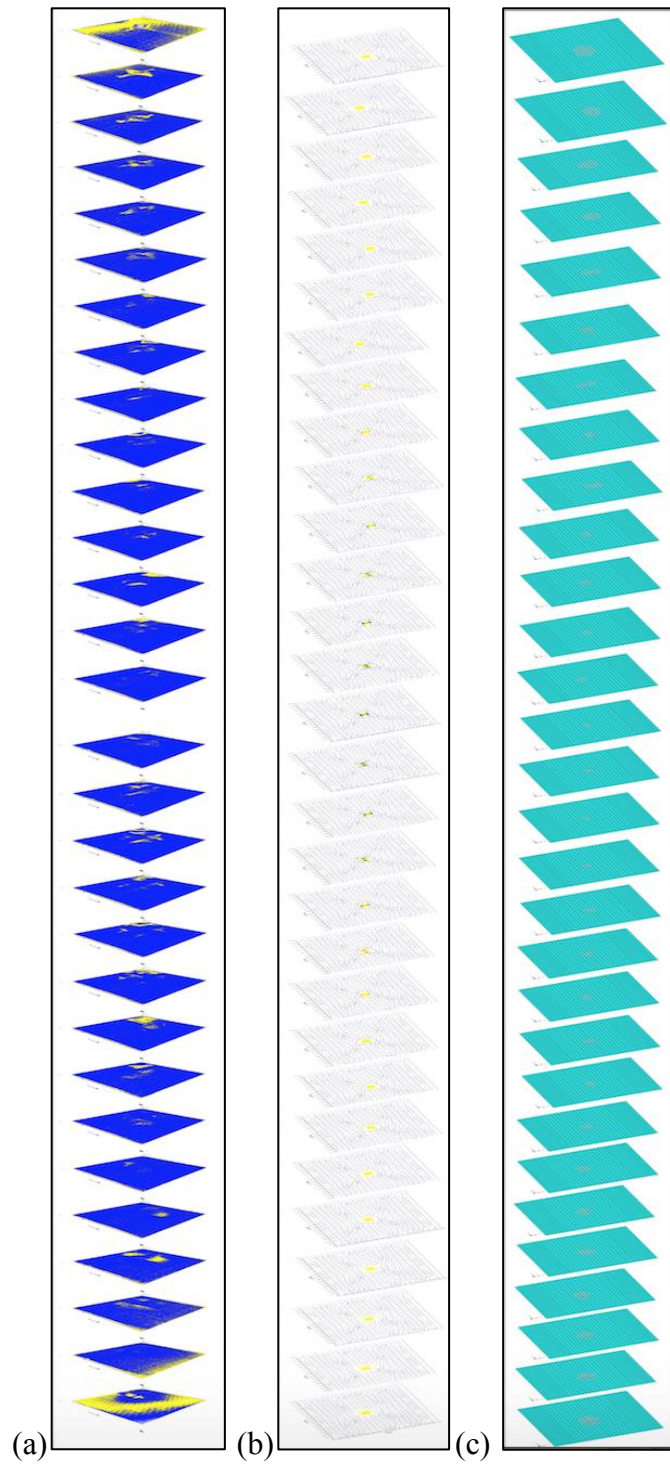


Figure 7. 3. Image stack of 30 interfaces for specimen 32-X-Low from (a) CT Scan, (b) Matlab damage prediction, and (c) ABAQUS electrical FE model.

### 7.1.2 Integration of Simulation-Based Delamination into FE Models: Results

The first step in validating the simulation-based damage sensing models was to compare the FE predictions to experimental results from McAndrew [17,18]. Experimental and FE simulation results for top and oblique resistance were recorded in Table 7. 1. for 16- and 32-ply quasi-isotropic AS4/3501-6 specimens. For the 16-Q specimen, the impact damage caused an increase in top resistance of 0.403% in the experiment, compared to 0.260% in the ABAQUS simulation. The oblique resistance increased by 0.654% and 0.735% for the experiment and simulation, respectively. Moreover, the magnitude of the resistance change was identical at 8.2E-5 Ohms for both the experiment and simulation. For the 32-Q specimen, the top resistance increased by 0.163% and 0.196% for the experiment and simulation, respectively. For oblique resistance, the impact caused a rise in resistance of 0.672% and 0.480%, respectively. Overall, the experimental and simulation predictions correlated very well for both 16-Q and 32-Q specimens, which motivated the investigation of the influence of impact damage on additional cross-ply specimens.

Additional models were developed based on the impact experiments conducted on 32-X and 16-X specimens, and the results are tabulated in Table 7. 2. The 32-X simulations were conducted for three impact energies in order to determine the influence of increasing impact energy (peak impact load) on the electrical resistance. For the lowest impact energy, the top and oblique resistance increased by 0.157% and 0.242%, respectively. At an intermediate energy, top and oblique resistance increased by 0.258%



Table 7. 1. Experimental and FE Simulation Results for Top and Oblique Resistance for 16-Q and 32-Q Specimens

Specimen Type	Impact Description	Experimental Rtop [Ohm]	ABAQUS Rtop [Ohm]	Experimental Robl [Ohm]	ABAQUS Robl [Ohm]
16-Q	None	9.263E-03	6.542E-03	1.254E-02	1.116E-02
	Int Energy	9.300E-03	6.559E-03	1.263E-02	1.124E-02
	<b>Change</b>	<b>3.730E-05</b>	<b>1.700E-05</b>	<b>8.200E-05</b>	<b>8.200E-05</b>
	<b>% Change</b>	<b>0.403%</b>	<b>0.260%</b>	<b>0.654%</b>	<b>0.735%</b>
32-Q	None	8.723E-03	6.489E-03	1.630E-02	2.357E-02
	Int Energy	8.737E-03	6.502E-03	1.641E-02	2.369E-02
	<b>Change</b>	<b>1.420E-05</b>	<b>1.270E-05</b>	<b>1.096E-04</b>	<b>1.132E-04</b>
	<b>% Change</b>	<b>0.163%</b>	<b>0.196%</b>	<b>0.672%</b>	<b>0.480%</b>

and 0.433%, respectively. At the highest impact energy top and oblique resistance increased by 0.558% and 0.711%, respectively. These results indicate that as impact energy (peak load) increased, the resistance continued to escalate due to an increase in the delamination damage. Peak impact load for the low, intermediate, and high-energy tests were 7786 N, 9253 N, and 11748 N, respectively. From the low to high-energy tests, the peak impact load increased by a factor of 1.5. The changes in top and oblique resistance due to the impact, however, increased by a factor of approximately 3 when comparing the low and high-energy simulations. This result suggests that there is a non-linear correlation between peak impact load and electrical resistance. This finding follows the results from the damage sensing feasibility study, where it was shown that as the delamination damage grows very large, the resistance increases dramatically. For the 16-X specimen, top resistance increased by 7.238% compared to 30.369% for the oblique resistance. It is noteworthy that for the 16-X specimen, the predicted delamination was very severe, which supports the influence on resistance. For the 32-X, 32-Q, and 16-Q specimens, the predicted delamination was much less severe, which is why the electrical resistance changed by less than 1% for these simulations. Figure 7. 4. (a) – (b) shows the

Table 7. 2. FE Simulation Results for Top and Oblique Resistance for 32-X and 16-X Specimens

Specimen Type	Impact Description	ABAQUS Rtop [Ohm]	ABAQUS Robl [Ohm]
32-X	None	2.948E-02	6.297E-01
	Low Energy	2.953E-02	6.312E-01
	<b>Change</b>	<b>4.620E-05</b>	<b>1.521E-03</b>
	<b>% Change</b>	<b>0.157%</b>	<b>0.242%</b>
	Int Energy	2.956E-02	6.324E-01
	<b>Change</b>	<b>7.610E-05</b>	<b>2.726E-03</b>
	<b>% Change</b>	<b>0.258%</b>	<b>0.433%</b>
	High Energy	2.96E-02	6.34E-01
	<b>Change</b>	<b>1.646E-04</b>	<b>4.475E-03</b>
<b>% Change</b>	<b>0.558%</b>	<b>0.711%</b>	
16-X	None	2.957E-02	2.923E-01
	After Impact	3.171E-02	3.811E-01
	<b>Change</b>	<b>2.140E-03</b>	<b>8.877E-02</b>
	<b>% Change</b>	<b>7.238%</b>	<b>30.369%</b>

stark contrast between the intensity of the delamination in specimen 16-X compared to the high energy impact in specimen 32-X.

For the 32-X specimen in Figure 7. 4. (a), the delamination was relatively small and barely extended to the edges of the innermost electrodes. For the 16-X specimen, on the other hand, the delamination was quite severe and reached beyond both the sensing and source electrodes. This explains the minimal rise in resistance for the damaged 32-X specimen compared to the drastic spike in resistance for the damaged 16-X specimen. This result was reminiscent of the damage sensing feasibility study in section 5.2.2., where the large delamination extended beyond the electrode spacing and resulted in a much larger influence on resistance compared to the small delamination. This supports a conclusion that in order to provide sensitive response to delamination damage, the electrodes must be spaced relatively close compared to the size of the delamination damage itself.

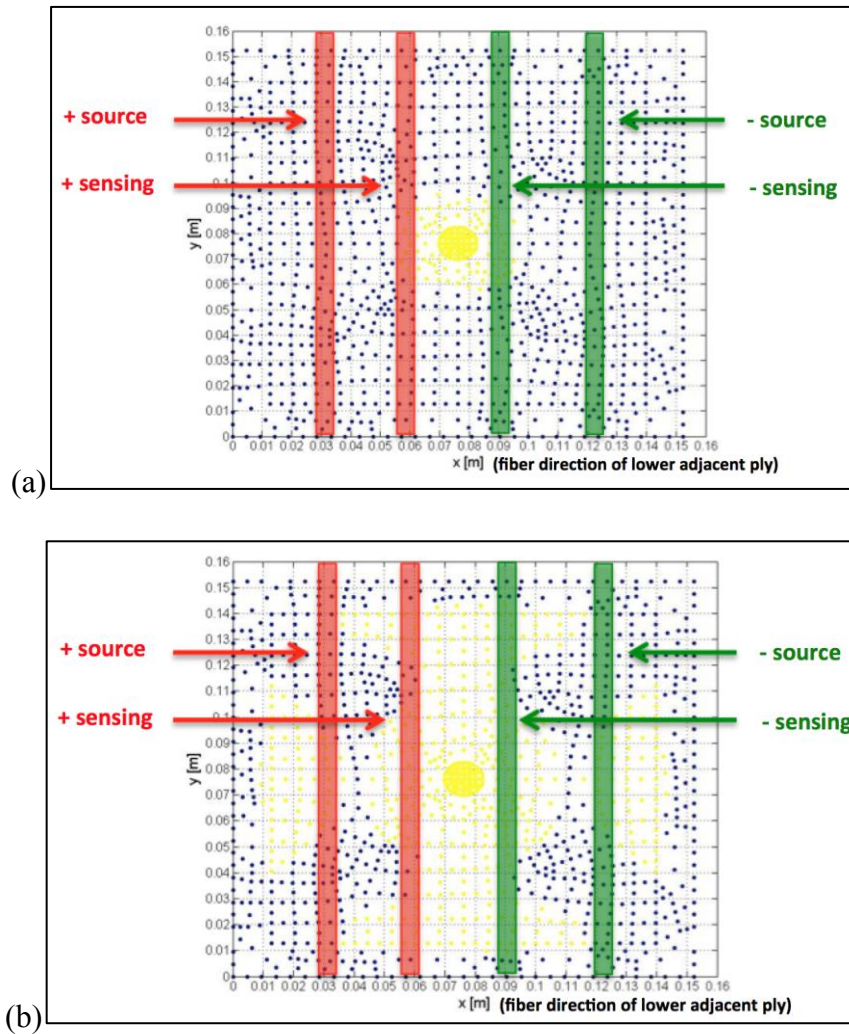


Figure 7. 4. Delamination plots of interface 1 with electrode locations shown for (a) specimen 32-X-High and (b) specimen 16-X. Fiber direction of lower adjacent ply corresponds with x-axis.

## 7.2 Correlation Between Voids and Resistance using CT Images

### 7.2.1 Calculation of Void Content Using CT Images

Several factors influenced the decision to perform CT scans on the specimens 16-U-0BP, 16-U-4BP, and 16-U-7BP, including: (i) the difference in resistance between the 4BP and 7BP specimens was greater than expected for the line-type 4-probe specimens and (ii) the specimens were produced individually by hand so there was uncertainty in the quality of the microstructure. The specimens 16-U-0BP-13, 16-U-4BP-13, and 16-U-7BP-13 selected for CT imaging were manufactured in the same batch. CT scans were completed following the methods outlined in Section 3.5. The images were imported into myVGL viewer software, and the initial gray values were set such that the composite would be colored gray and any voids (air bubbles) would be colored black. Images of the specimens are shown in Figure 7. 5. (a) – (d). In order to better observe the voids through the thickness of the specimen, the gray values were set such that the composite was colored blue and the voids were colored yellow and black.

The voids found in in Figure 7. 5. (d) and Figure 7. 6. were of ellipsoidal shape and ran along the length of the fibers in the carbon fiber layers. Moreover, the voids were more highly concentrated around the locations of the BP layers. These findings are comparable to trends in woven carbon fiber laminates found in the literature. For woven CF laminates, voids tend to orient with the fiber direction and are more likely to concentrate in layers with off-axis fiber directions. These off axis fiber-direction layers slow down resin flow during manufacturing, which increases the likelihood of void formation [71]. In the case of the BP layers in the current thesis, the CNT's were

randomly oriented, which would have a similar influence on resin flow. The presence of voids was particularly concerning, because it is well known that voids can lead to a dramatic reduction on the impact strength of CFRP composites. The influence of voids on the electrical response has not been well documented, thus it was an objective of the current study to quantify and model the voids in an electrical model.

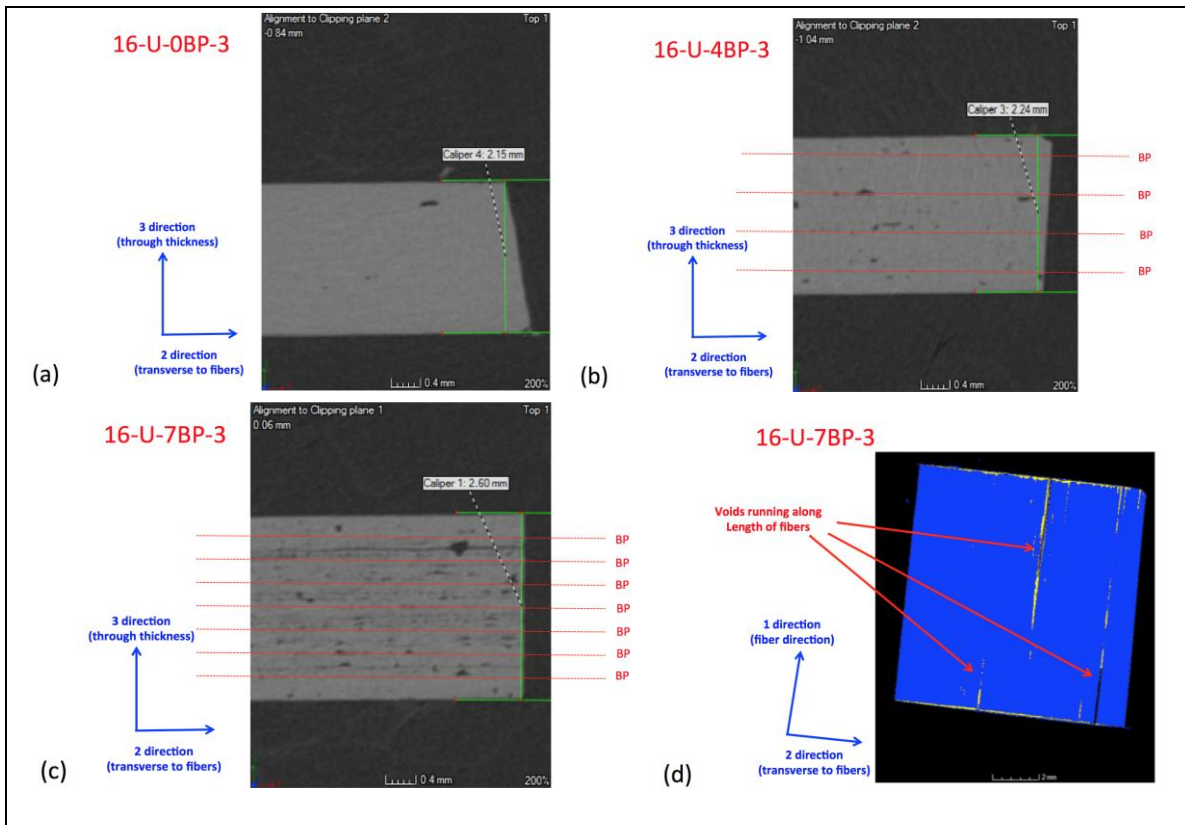


Figure 7. 5. CT images of specimens with (a) 0, (b) 4, (c) 7 layers of BP with voids colored black, and (d) elliptical voids (yellow/black) running the length of the fibers.

In order to quantify the volume percentage of voids in each specimen, the image slices in Figure 7. 6. were analyzed utilizing the image color summarizer developed by Krzywinski [72]. The Matlab program developed by Demerath [50] was considered,

however, the ease of use and universal availability of the program from Krzywinski was more attractive. In order to compare the two programs, the specimen 3 from the thesis of Demerath [50] was used for evaluation. The Krzywinski program calculated 0.377% damage compared to 0.359% for the Demerath program. Using the image color summarizer, images were each discretized into 200 x 200 pixels and the percentage of each color was computed for each image. The slices were taken at equal intervals through the thickness, so the results in Table 7. 3. are equivalent to the average void percentage over the entire image stack. The specimen with 0BP had the lowest void content at 0.45%, followed by the specimen with 4BP at 0.99 %, and the highest void content was in the specimen with 7 layers of BP at 2.86%. A reasonable explanation for this result is that the BP layers had lower porosity compared to the CF layers, thus slowing down the seepage of air bubbles during manufacturing. This conclusion is supported by Figure 7. 5. (d), which shows the collection of air bubbles near the BP layers.

Table 7. 3. Color summary and void content of specimens with 0, 4, and 7 layers of BP

Slice #	16-U-0BP			16-U-4BP			16-U-7BP		
	% blue	% black	% yellow	% blue	% black	% yellow	% blue	% black	% yellow
1	99.34%	0.36%	0.30%	99.44%	0.20%	0.36%	99.26%	0.47%	0.27%
2	99.42%	0.58%	0.00%	98.70%	0.60%	0.70%	99.56%	0.30%	0.14%
3	99.43%	0.53%	0.04%	99.63%	0.24%	0.13%	96.96%	1.87%	1.17%
4	99.87%	0.00%	0.13%	99.06%	0.57%	0.37%	98.63%	0.69%	0.68%
5	99.00%	0.84%	0.16%	99.13%	0.48%	0.39%	98.68%	0.75%	0.57%
6	99.69%	0.31%	0.00%	98.10%	1.59%	0.31%	97.81%	1.29%	0.90%
7	99.33%	0.51%	0.16%	98.70%	0.66%	0.64%	97.18%	1.76%	1.06%
8	99.64%	0.24%	0.12%	99.28%	0.41%	0.31%	96.45%	2.07%	1.48%
9	99.89%	0.00%	0.11%	97.73%	1.32%	0.95%	99.47%	0.32%	0.21%
10	99.86%	0.00%	0.14%	98.76%	0.80%	0.44%	96.28%	2.24%	1.48%
11	99.71%	0.00%	0.29%	99.18%	0.52%	0.30%	98.19%	0.76%	1.05%
12	98.85%	0.79%	0.36%	99.19%	0.57%	0.24%	95.38%	3.04%	1.58%
13	99.63%	0.18%	0.19%	99.56%	0.20%	0.24%	99.34%	0.42%	0.24%
14	99.69%	0.20%	0.11%	99.50%	0.20%	0.30%	83.41%	8.75%	7.84%
15	99.70%	0.16%	0.14%	99.44%	0.40%	0.16%	99.09%	0.52%	0.39%
16	99.69%	0.18%	0.13%	98.81%	0.83%	0.36%	98.62%	1.22%	0.16%
<b>average</b>	99.55%	0.31%	0.15%	99.01%	0.60%	0.39%	97.14%	1.65%	1.20%
	<b>Total Voids</b>		<b>0.45%</b>	<b>Total Voids</b>		<b>0.99%</b>	<b>Total Voids</b>		<b>2.86%</b>

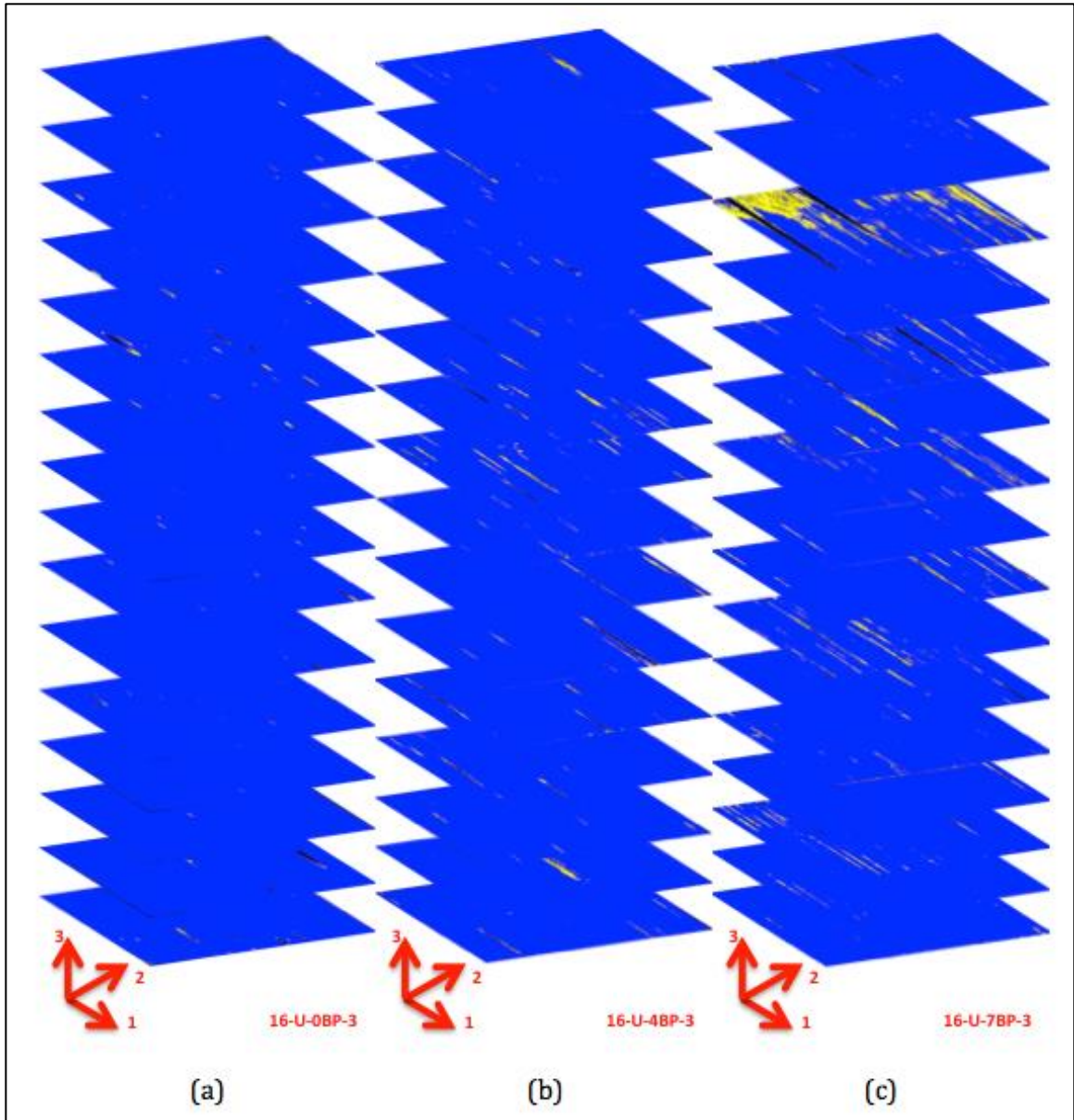


Figure 7. 6 CT image stacks of specimens with (a) 0, (b) 4, (c) 7 layers of BP. Voids are colored black and yellow. Fiber direction corresponds to 1-direction.



## 7.2.2 Integration of CT Image-Based Voids into FE

### Models: Methods

In order to assess the influence of manufacturing defects (i.e. voids) on electrical resistance, CT scans were performed on 16-U-0BP, 16-U-4BP, and 16-U-7BP specimens. Similar to the simulation based damage models of 7.1.1, the CT image-based void models were developed using a 4-step process, as shown in Figure 7. 7. The first step was to perform CT scans on 10mm x 10mm specimens and set the gray-values such that the undamaged volume was colored blue and voids were colored yellow. Second, the 3-D CT Scans were deconstructed into 2-D image slices. Sixteen image slices were extracted from each of the CT scans, which corresponded to one image slice per carbon fiber ply. In the third step, the 2-D image slices were transposed into 2-D sketches. In the fourth step, the 2-D sketches were extruded to produced 3-D voids.

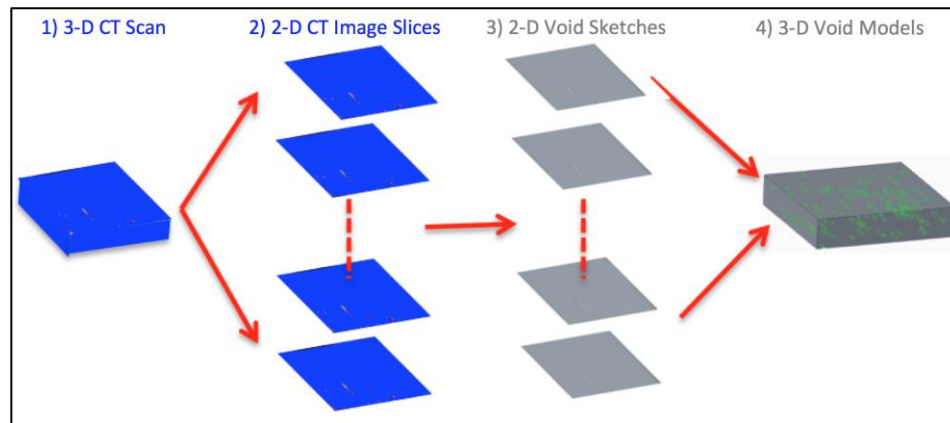


Figure 7. 7. 4-step procedure for incorporating CT image-based impact damage into electrical FE models.

The 3-D microstructure of the CT scans was much more complex than the 2-D delamination predictions of 7.1.1, therefore it was not practical to model the voids using the limited modeling capabilities built into ABAQUS. Instead, Creo Parametric ® was utilized for modeling the 3-D microstructure. The first step in the modeling process was to extrude a solid block with the dimensions 10 mm x 10 mm x 2.13mm, which represented the exact dimensions of the scanned specimen 16-U-0BP. The next step was to create 16 datum planes through the specimen, which corresponded to the locations of the 16 image slices extracted from the CT scan, as shown in Figure 7. 8. The following steps displayed in Figure 7. 8 - Figure 7. 12 represent the modeling work for the uppermost image slice of the 16-U-0BP specimen. The process was then repeated 16 times (one for each image slice from the CT scan).

In order to transcribe the CT microstructure into the Creo model, a copy of the 2-D CT image slice was overlaid on the 3-D model using the appearance gallery feature in Creo, as shown in Figure 7. 9. Next, a 2-D sketch was created on the datum plane corresponding to the location of the current CT image slice. The voids were outlined with long needle-like rectangular areas, as displayed in Figure 7. 11. The actual voids were more elliptical in shape, but rectangles were used instead to simplify the subsequent mesh creation in ABAQUS. The 2-D sketch was then extruded to remove the material corresponding to the voided volume (see Figure 7. 12.). The resulting model then consisted of a 3-D solid, representing the bulk composite material and a 3-D array of voids, reminiscent of Swiss cheese. A 2-D section view and 3-D rendering of the complete 16-U-0BP specimen is shown in Figure 7. 12. (a) – (b), respectively. The 3-D

Creo “.prt” models were then exported into solid “.stp” files so that they could be imported into ABAQUS.

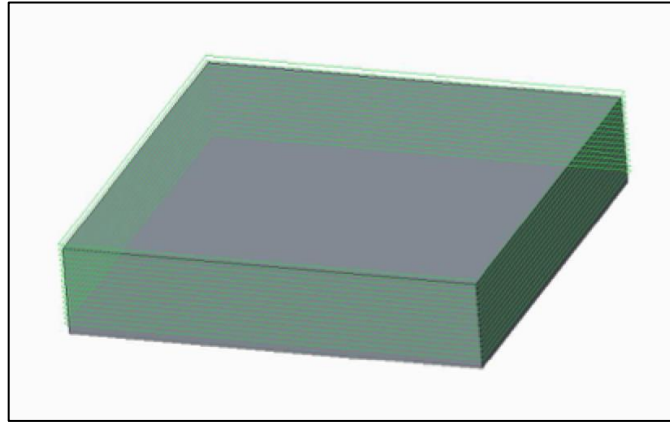


Figure 7. 8. 3-D model of CT image specimen 16-U-0BP with 16 datum planes shown in green.

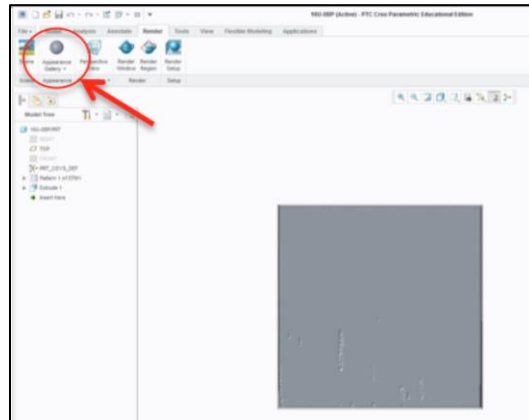


Figure 7. 9. Example of CT image slice overlaid onto the 3-D model using the appearance gallery feature in Creo.

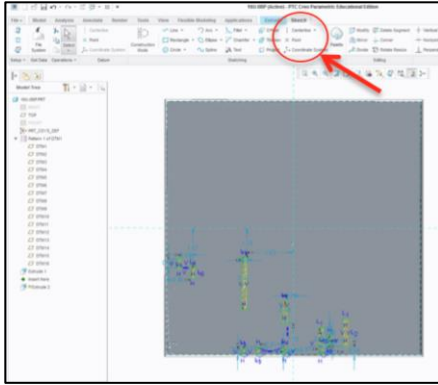


Figure 7. 10. 2-D sketch of rectangular needle-like voids running in the direction of the carbon fibers.

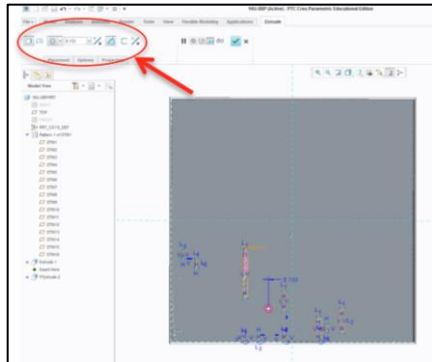


Figure 7. 11. 3-D removal of void material using the extrude function in Creo.

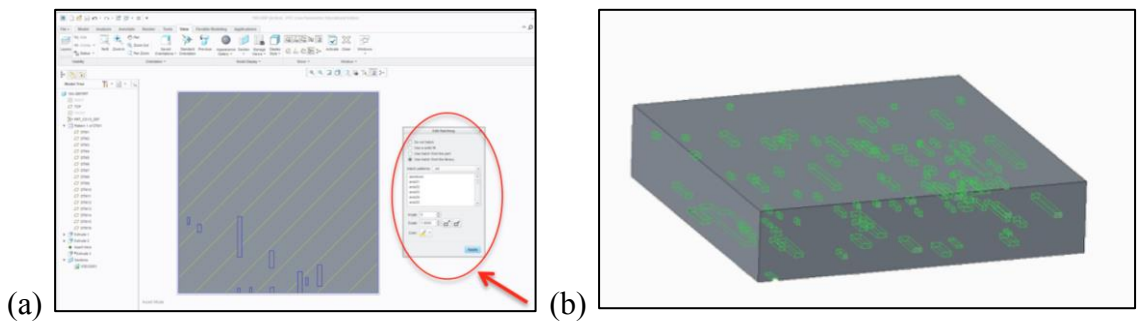


Figure 7. 12. (a) Section view of voids from one image slice and (b) a rendering of a complete 3-D model with voids outlined in green.

Once the “.stp” models were imported into ABAQUS, the geometry was meshed using 4-node DC3D4E linear coupled thermal-electric tetrahedron element. The tetrahedron element was used rather than the quadrilateral element due to the complex geometry of the voids. The geometry was meshed using the free-meshing technique to allow for mesh concentration around the voids. As seen in Figure 7. 13. (a) - (c), as the void content increased, the density of the mesh increased exponentially.

In the electrical models, the composite material was homogenized, meaning that there was no distinction between the fibers and matrix. The material was then assumed to have orthotropic material properties, which is a valid assumption at the macroscale. When considering the effects of voids, however, the influence occurs at an intermediate scale, which is much larger than the diameter of an individual fiber but less than the thickness of the laminate. Therefore in order to verify the validity of the aforementioned assumption of orthotropic properties, the influence of the voids need to be considered. In the transverse and through-thickness directions, voids reduce the number of fiber-to-fiber contact points, which decrease electrical conductivity in these principle directions. In the fiber direction, however, the electrical conductivity is not dependent on these isolated contact points, which means that voids should not influence conductivity in fiber direction. In a realistic composite (see Figure 7. 14. (a)), fibers are not perfectly straight,

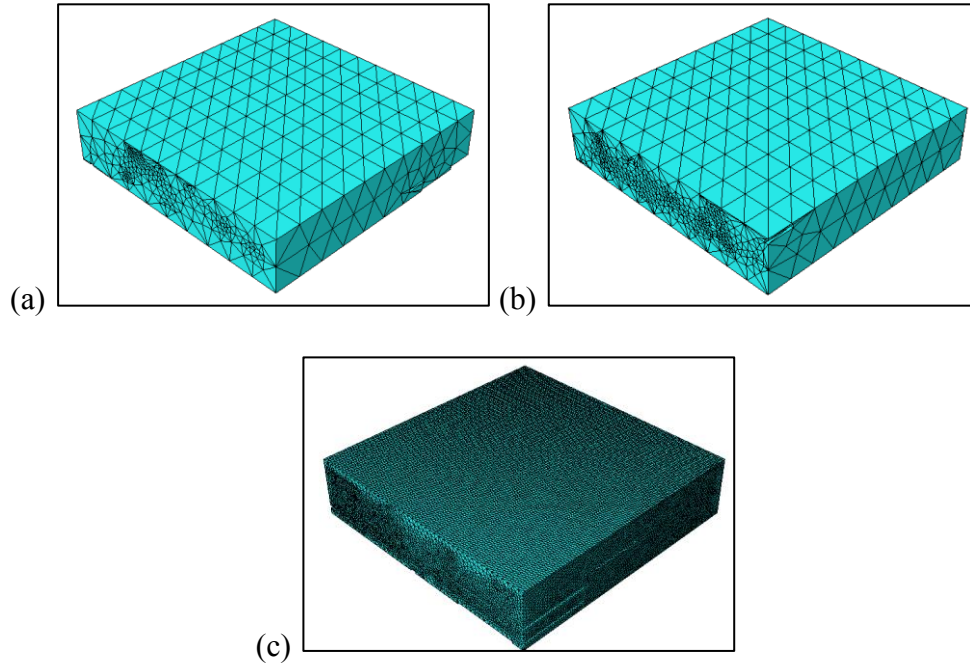


Figure 7. 13. ABAQUS mesh for void models of specimens (a) 16-U-0BP, (b) 16-U-4BP, and (c) 16-U-7BP.

and will conform around voids without breaking. In a homogenized orthotropic material, on the other hand (see Figure 7. 14. (b)), the material model assumes that the fibers are perfectly straight. When a void is introduced, the resulting influence on the model is equivalent to a broken fiber, which is unrealistic. Therefore, in this study, the resistance was not measured in the fiber direction. The electrical properties used in the simulations were the properties for 16-U-0BP specimens recovered using the line-type 4-probe method, as discussed in the electrical characterization section. The material properties and specimen thickness remained constant for all simulations so that the only change between simulations was the void content.

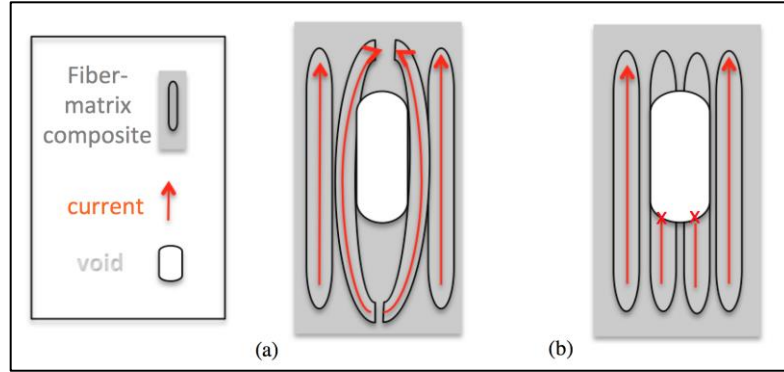


Figure 7. 14. (a) Fiber bending/waviness around voids in a realistic composite versus (b) interpretation of voids in fiber-direction for a homogenized orthotropic material.

In order to analyze the influence of the voids on electrical resistance, 2-probe electrical simulations were performed on the specimens in two principle directions: (i) transverse to fiber direction and (ii) in the through-thickness direction, as shown in Figure 7. 15. Copper electrodes were placed on opposite surfaces of the specimen, and 2-probe resistance was recorded. The electrodes covered the entire surface of the specimen to essentially eliminate variation normal to the direction of measurement. In order to provide a control group for comparison purposes, identical simulations were repeated on solid specimens with no voids.

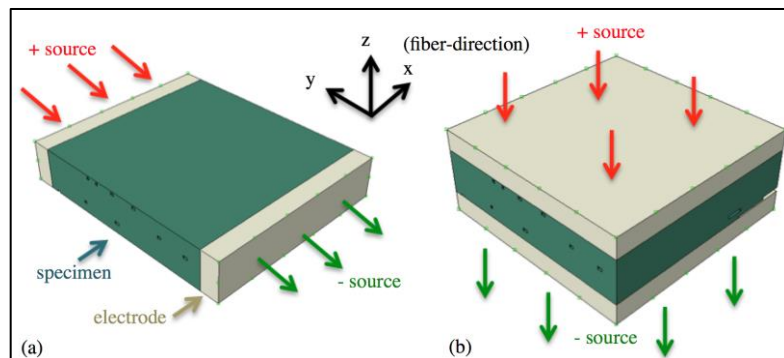


Figure 7. 15. Locations of electrodes and current source for resistance measurement (a) transverse to fiber direction and (b) through-thickness.

### 7.2.3 Integration of CT Image-Based Voids into FE

#### Models: Results

Upon first observation of the data in Table 7. 4, it is clear that there is no definitive correlation between the direction of measurement and influence of voids on resistance. From the results of the void content study, the volumetric void contents of the 16-U-0BP, 16-U-4BP, and 16-U-7BP specimens were 0.45%, 0.99%, and 2.86%, respectively. For the same specimens, however, the voids caused resistance to increase by an average of 0.97%, 2.87%, and 12.1%, respectively. This result suggests that there is a non-linear correlation between void content and electrical resistance. This conclusion is similar to the observations discussed previously for the damage sensing results in 7.1.2. An explanation for this non-linear correlation can be visualized when considering the distribution of voids relative to the measurement direction.

In Figure 7. 16. (a) – (c) and Figure 7. 17 (a) – (c), side and top planar views are displayed, which show the distribution of voids in each of the specimens with 0.45%, 0.99%, and 2.86% void content. As shown in Figure 7. 16. (a) and Figure 7. 17 (a), for the specimen with 0.45% voids, there exists a relatively clear path for the current to travel through. In this specimen, there are several sections where the current can flow straight

Table 7. 4. FE Simulation Results for Resistance in Fiber-, Transverse-, and Through Thickness-Directions for Specimens With and Without Voids

Electrical Properties	Direction of Measurement	0.00% Voids R [Ohm]	0.45% Voids R [Ohm]	% diff from 0	0.99% Voids R [Ohm]	% diff from 0	2.86% Voids R [Ohm]	% diff from 0
16-U-0BP	Transverse	3.109E+02	3.138E+02	0.93%	3.197E+02	2.84%	3.434E+02	10.43%
	Thickness	3.952E+01	3.989E+01	0.93%	4.062E+01	2.79%	4.371E+01	10.60%



through from electrode to electrode without encountering any voids. As the void content increases to 0.99% and 2.86%, however, these clear paths quickly disappear, and as the current encounters the voids, the current is constricted and forced to flow around the void in a path of relatively high resistance. This “clear path” explanation supports the non-linear relationship between volumetric void content and electrical resistance. Also this explanation would suggest that a definite statistical trend between void content and electrical resistance would not exist. Instead, the relationship between voids and electrical resistance would depend on but not limited to considerations such as: (i) size/shape of voids, (ii) orientation relative to fibers, and (iii) distribution of voids in 3-D space.

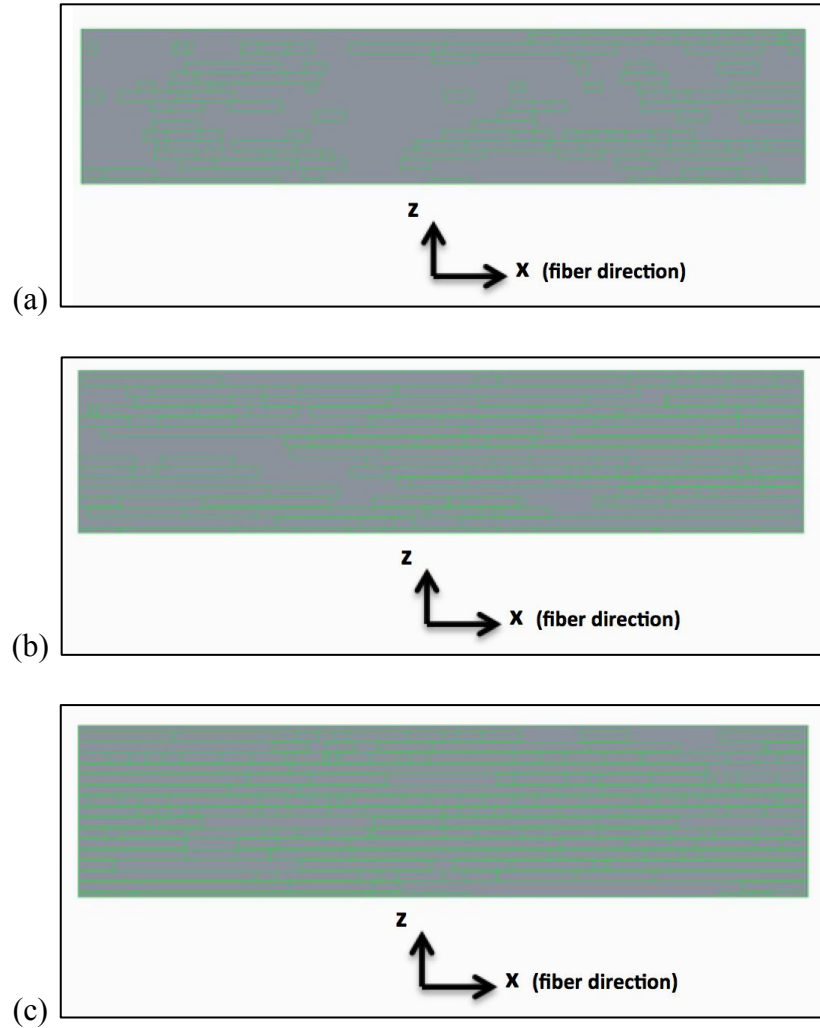


Figure 7. 16. Side view showing distribution of voids for transverse resistance measurement for (a) 16-U-0BP, (b) 16-U-4BP, and (c) 16-U-7BP. Voids are outlined in green.

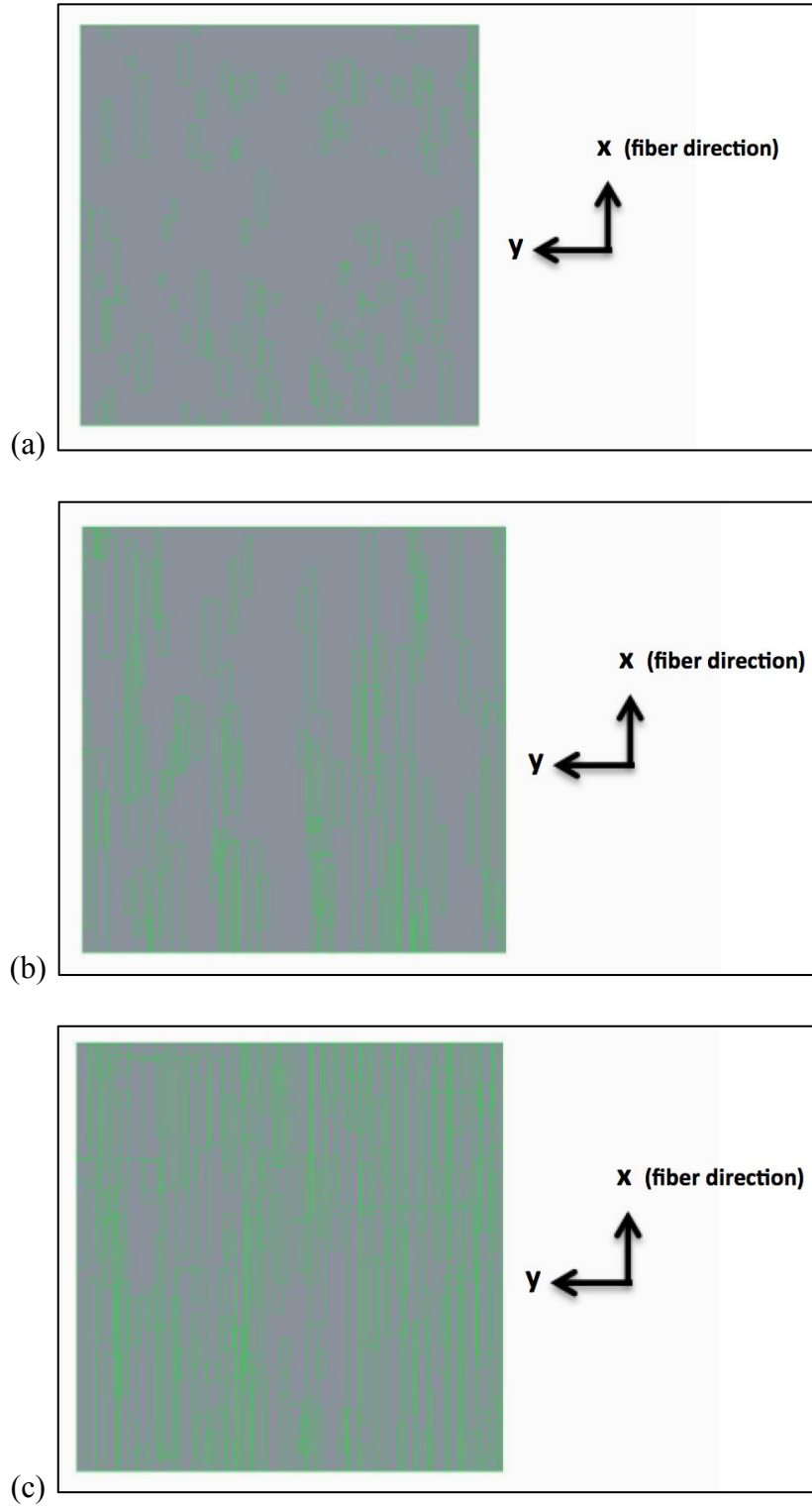


Figure 7. 17. Top view showing distribution of voids for through-thickness resistance measurement for (a) 16-U-0BP, (b) 16-U-4BP, and (c) 16-U-7BP. Voids are outlined in green.

### 7.3 Influence of Delamination and Voids on Electrical Resistance: Summary

In this chapter, the simulation-based delamination predictions were integrated into 4-probe electrical FE models for the purpose of electrical resistance-based damage sensing. Based on the results, it was concluded that both top and oblique resistance planes were sensitive to presence of delamination, however the oblique measurement plane was slightly more sensitive. In addition, the delamination damage caused only a modest increase in resistance of less than 1% for 16-Q, 32-Q, and 32-X specimens. This trend followed the results of the experimental work of McAndrew [17,18]. In all of these specimens, the size of the delamination damage was relatively moderate compared to the spacing of the electrodes. For the 16-X specimen, however, the impact-induced delamination was much more severe and extended well beyond the electrodes. For this specimen, the delamination damage caused an increase in top and oblique electrical resistance of 7% and 30%, respectively. This result indicated that for electrical resistance-based damage sensing applications, the spacing of electrodes relative to the size of the delamination is critical in order to achieve the best sensitivity to damage.

In addition, CT scan data was integrated into 2-probe electrical FE models for studying the influence of voids on electrical resistance transverse to fiber direction and through thickness. The results demonstrated that there was a non-linear correlation between volumetric void content and electrical resistance. A “clear path” explanation was proposed, which suggested that for very small void content, there was a relatively clear path for current to flow directly from electrode to electrode without encountering many voids. As the void content increased, the clear path began to disappear and current was forced to flow around voids in a path of relatively high resistance. The current thesis has

established a comprehensive foundation for electrical resistance based damage analysis using macro-scale FE modeling and provides a framework for future research and development.

## CHAPTER 8: CONCLUSIONS, RECOMMENDATIONS, AND FUTURE WORK

### 8.1 Conclusions

In the current thesis, experimental methods and computational models have been developed for electrical and low-velocity-impact characterization of carbon fiber reinforced polymer matrix composites (CFRP). In particular, electrical and impact responses were studied for applications in low velocity impact damage sensing of CFRP composites.

A new robust method was developed for recovering the directionally dependent electrical resistivities using an experimental line-type 4-probe resistance method. Next, the concept of effective conducting thickness was leveraged in the development of a novel point-type 4-probe method for applications with electrically anisotropic materials. 4-probe electrical FE models were developed in COMSOL using the electrical resistivities obtained from the experimental tests, and the effective thickness was found to be of critical importance in achieving accurate simulation results. The electrical models were validated versus the experimental resistance measurements and also demonstrated predictive capabilities when applied to CFRP specimens with varying thickness and layup.

The influence of prescribed localized damage on the 4-probe resistance was studied using FE models developed in ABAQUS. First, quasi-static FE models for delamination prediction were developed based on the experimental peak impact load for various CFRP specimens. These simulation-based delamination predictions were then integrated into the

electrical resistance-based damage sensing FE models in order to observe the influence of realistic damage patterns on electrical response in the CFRP specimens of various thickness and layup.

In the 16-ply and 32-ply quasi-isotropic and 32-ply cross-ply specimens, the size of the delamination damage was relatively moderate compared to the spacing of the electrodes, and the delamination caused less than 1% increase in electrical resistance. For the 16-ply cross-ply specimen, however, the impact-induced delamination was significantly larger and extended beyond the electrode locations, resulting in an increase in resistance of 30% for the oblique measurement plane. This result suggests that for damage sensing applications, the spacing of electrodes relative to the size of the delamination is critical in order to achieve the best sensitivity to damage.

The effect of manufacturing defects (i.e. voids) on the electrical response of the CFRP composites has been studied experimentally using computed tomography and computationally using the developed FE models. CT image data was used to model 3-D void distributions, and the electrical response of such specimens were compared to models with no voids. For minimal void content of 0.45%, there was a relatively clear path for current to flow directly from electrode to electrode without encountering many voids. As the void content increased to 0.99% and 2.86%, the clear path began to rapidly disappear and current was forced to flow around voids in a path of relatively high resistance.

The implementation of realistic, simulation-based impact damage rounded out the current thesis work and the methods presented herein provide a complete framework for

predictive resistance-based damage models for CFRP specimens subjected to low-velocity impact.

## 8.2 Recommendations and Lessons Learned

Given the broad scope of the work in the current thesis and the multitude of new methods introduced, there are several lessons learned through this process that may benefit those attempting to replicate this work. These recommendations and lessons learned have been separated into three categories: (i) experimental work, (ii) recovery of electrical properties, and (iii) FE modeling.

### 8.2.1 Recommendations and Lessons Learned:

#### Experimental Work

During the electrical characterization work, surface preparation of the specimens was critical in order to achieve reasonable and consistent measurements, even for specimens from the same batch. As the superficial layer of epoxy is removed from the surface of the composite to expose the conductive carbon fibers, the epoxy dust can cause the sandpaper to lose its abrasive grit. In order to ensure consistent surface finish, the sandpaper must be changed regularly and at a consistent interval from specimen to specimen. This recommendation applies to both the line-type and point type methods. Specific to the point-type method, consistent alignment and holding force were important to achieve precise measurements. Given the large variation from measurement to measurement, the probe device could be improved to include automatic alignment and controlled holding force. For the line-type method, once surface was prepped, accurate



placement of the electrodes was absolutely critical. In order for the electrical properties to be recovered from the experimental data, the top sensing electrodes must be secured directly above the bottom sensing electrodes.

### 8.2.2 Recommendations and Lessons Learned: Recovery of Electrical Properties

When recovering the orthotropic electrical properties of a unidirectional CFRP laminate, even a slight change in the ratio of the top voltage measurement to bottom voltage measurement can have a dramatic influence on the properties recovered in the principal directions. Therefore, if the top and bottom sensing electrodes are not accurately aligned, the properties recovered will not represent the physical composite. In addition, for the electrical properties to be recovered using the methods herein, the electrical resistivities must be similar in magnitude for at least two principal directions. This ensures that the effective conducting thickness will be large enough such that the current penetrates through the full specimen thickness and that the bottom voltage measurement is valid. If the specimen cannot be aligned to ensure that current penetrates through the thickness, then these methods will not work and some of the electrical properties need to be assumed. When electrical properties are assumed and not recovered, then the solution is no longer unique (i.e. multiple combinations of orthotropic electrical resistivities can give the same voltage measurement) and any FE predictions cannot be validated with certainty against the experimental data.

### 8.2.3 Recommendations and Lessons Learned: FE

#### Modeling

During the development of the electrical FE models, the implications of the effective conducting thickness were instrumental in achieving accurate FE predictions. If in a top resistance test, the geometry beyond the effective conducting thickness were included in a linear current-voltage model, the FE predictions would be misleading and inaccurate. When modeling laminates with plies alternating at various fiber angles, effective thickness is considered on a ply-by-ply basis from the top-down. In such laminates, the current would find the path of least resistance, which means that current may penetrate through the thickness to flow primarily in plies with favorable fiber orientations. This finding may have important physical implications in applications such as electrical/shock protection. If highly conductive layers are needed to disperse electrical energy, it may not be necessary to place such layers directly on the exterior surface. For instance, the conductive plies may be able to be placed somewhere within the thickness for protection or structural advantages. In addition to the electrical FE models, lessons were also learned during the development of quasi-static impact and damage sensing models.

During the development of the quasi-static impact models, the shape and contact area of the impact striker had a moderate influence on the size and shape of the predicted delamination. The overall accuracy of the delamination prediction was limited due to the use of a quasi-static loading approach. For the quasi-static models, only the peak impact load was used for delamination prediction, which is not directly related to impact energy or velocity. It is well known that changing impact energy and/or velocity can have a

meaningful influence on the impact-induced damage. Such effects may not be captured through the peak impact load alone. In addition, the quasi-static approach does not account for progressive failure such as fiber breaking and reloading nor the effect of matrix crack propagation. When implementing the simulation-based delamination patterns into the electrical resistance-based damage sensing models, the models required an assumption on influence of the damage on through-thickness conductivity. Future work should focus on developing methods to eliminate the need for such assumptions as well as validating the newly developed methods through mathematical formulation.

The methods and FE models developed in the current thesis were conducted at a scale such that the material was assumed to be homogenized with no distinction between the fibers and surrounding epoxy matrix. This approach makes the modeling and methods accessible to a broader audience, but careful consideration is required to verify that the assumptions are valid and that the resulting data is meaningful. For instance when modeling voids in sections 7.2.2. and Figure 7. 14., it was determined that it would not be appropriate to measure FE resistance in the fiber direction, because a homogenized orthotropic material model does not consider natural waviness of fibers and would interpret the presence of voids as similar to a broken fiber.

### 8.3 Future Work

In continuation of the aforementioned work, future work will focus on validating the new methods through additional theoretical, computational, and experimental work. For the line-type 4-probe method, additional experimental work should focus on validating the concept of the effective conducting thickness. For instance, work could

focus on testing the top resistance of CFRP specimens with progressively increasing thickness to determine the point at which the current no longer penetrates through the thickness. Similarly for the point-type 4-probe method, future work should involve further development of a mathematical model for voltage distribution throughout the specimen. In addition, the experimental methods and handheld probe could benefit from additional refinement to reduce measurement-to-measurement variability. This method could benefit from a more advanced semi-automated device with locating features and calibrated clamping force for more consistent measurements. When considering the computational modeling, the impact damage models would be markedly improved through the use of dynamic progressive failure models. In addition, for the electrical resistance-based damage sensing models, the next generation could include the effects of fiber-matrix interactions at the micro-scale. In this approach, a multi-scale model would need to be developed wherein a representative volume element (RVE) would contain distinct carbon fibers and epoxy matrix materials.

APPENDIX A: ELECTRICAL

$$\begin{aligned}
 F^{-1} = & \frac{1}{a} \left[ (y_b - y_a) + \sum_{m=1}^{\infty} \frac{2}{\xi \sinh(b\xi)} \left[ \left\{ \cos(\xi x_b) \cosh \left( \xi \left( y_b + \frac{b}{2} \right) \right) - \right. \right. \right. \\
 & \left. \left. \left. \cos(\xi x_c) \cosh \left( \xi \left( y_c + \frac{b}{2} \right) \right) \right\} \times \cos(\xi x_a) \cosh \left( \xi \left( y_a - \frac{b}{2} \right) \right) - \right. \\
 & \left. \left\{ \cos(\xi x_b) \cosh \left( \xi \left( y_b - \frac{b}{2} \right) \right) - \cos(\xi x_c) \cosh \left( \xi \left( y_c - \frac{b}{2} \right) \right) \right\} \times \right. \\
 & \left. \left. \left. \cos(\xi x_d) \cosh \left( \xi \left( y_d + \frac{b}{2} \right) \right) \right] + \sum_{n=1}^{\infty} \frac{2}{\eta \sinh(b\eta)} \left[ \left\{ \cosh \left( \eta \left( y_b + \right. \right. \right. \right. \\
 & \left. \left. \left. \frac{b}{2} \right) \right) - \cosh \left( \eta \left( y_c + \frac{b}{2} \right) \right) \right\} \times \cosh \left( \eta \left( y_a - \frac{b}{2} \right) \right) - \left\{ \cosh \left( \eta \left( y_b - \right. \right. \right. \right. \\
 & \left. \left. \left. \frac{b}{2} \right) \right) - \cosh \left( \eta \left( y_c - \frac{b}{2} \right) \right) \right\} \times \cosh \left( \xi \left( y_d + \frac{b}{2} \right) \right) \right] + \\
 & \sum_{m=1}^{\infty} \sum_{n=1}^{\infty} \frac{4}{\zeta \sinh(b\zeta)} \left[ \left\{ \cos(\xi x_b) \cosh \left( \zeta \left( y_b + \frac{b}{2} \right) \right) - \right. \right. \\
 & \left. \left. \cos(\xi x_c) \cosh \left( \zeta \left( y_c + \frac{b}{2} \right) \right) \right\} \times \cos(\xi x_a) \cosh \left( \zeta \left( y_a - \frac{b}{2} \right) \right) - \right. \\
 & \left. \left\{ \cos(\xi x_b) \cosh \left( \zeta \left( y_b - \frac{b}{2} \right) \right) - \cos(\xi x_c) \cosh \left( \zeta \left( y_c - \frac{b}{2} \right) \right) \right\} \times \right. \\
 & \left. \left. \left. \cos(\xi x_d) \cosh \left( \zeta \left( y_d + \frac{b}{2} \right) \right) \right] \right] \tag{A. 1}
 \end{aligned}$$

where:  $(x_a, y_a), (x_b, y_b), (x_c, y_c), (x_d, y_d)$  are coordinates of current probes A, B, C, and D in (cm).

a, b, and t are width, length, and thickness of specimen

$$\xi = \frac{m\pi}{a}, (m \text{ is integer})$$

$$\eta = \frac{n\pi}{t}, (n \text{ is integer})$$

$$\zeta = (\xi^2 + \eta^2)^{0.5}$$

The calculation of the summation terms are ended at a time when the term reaches  $10^{-15}$  or under. [61]

Table A. 1. 2-Probe High-Intensity Current Pulse Electrical Results

	<b>Analog Voltage [V]</b>	<b>Max Current [A]</b>	<b>Resistance [Ohms]</b>	<b>Current Error [A]</b>	<b>Resistance Error [Ohms]</b>
<b>32-U-7</b>	--	50.0	0.027	3.7	0.00199
	50	271.6	0.020	5.0	0.00037
	100	548.2	0.021	4.8	0.00018
	150	830.1	0.016	6.2	0.00012
	200	1107.7	0.018	5.4	0.00009
	250	1393.7	0.018	5.5	0.00007
<b>32-U-8</b>	--	50.0	0.035	2.8	0.00199
	50	330.0	0.021	4.8	0.00030
	100	670.0	0.016	6.2	0.00015
	150	1012.0	0.015	6.5	0.00010
	200	1365.0	0.017	5.8	0.00007
	250	1708.0	0.017	5.9	0.00006
<b>32-U-9</b>	--	50.0	0.039	2.6	0.00199
	50	320.3	0.022	4.5	0.00031
	100	664.3	0.027	3.7	0.00015
	150	1009.6	0.019	5.4	0.00010
	200	1352.9	0.018	5.5	0.00007
	250	1694.9	0.015	6.6	0.00006
	<b>Analog Voltage [V]</b>	<b>Max Current [A]</b>	<b>Resistance [Ohms]</b>	<b>Current Error [A]</b>	<b>Resistance Error [Ohms]</b>
<b>16-U-7</b>	--	50	0.056	1.8	0.00199
	20	128.8	0.059	1.7	0.00077
	50	278.0	0.047	2.1	0.00036
	100	617.2	0.035	2.9	0.00016
	150	734.5	0.111	0.9	0.00014
<b>16-U-8</b>	--	50.0	0.043	2.3	0.00199
	20	111.6	0.045	2.2	0.00089
	50	310.2	0.035	2.8	0.00032
	100	637.4	0.028	3.6	0.00016
	120	783.3	0.027	3.7	0.00013
	150	972.5	0.027	3.7	0.00010
	170	1108.9	0.025	4.0	0.00009
<b>16-U-9</b>	--	50.0	0.058	1.7	0.00199
	50	280.4	0.039	2.6	0.00035
	100	625.8	0.034	2.9	0.00016
	150	949.5	0.036	2.8	0.00010

Table A. 1. Continued

	<b>Analog Voltage [V]</b>	<b>Max Current [A]</b>	<b>Resistance [Ohms]</b>	<b>Current Error [A]</b>	<b>Resistance Error [Ohms]</b>
<b>16-X-7</b>	--	50.0	0.072	1.4	0.00199
	20	105.0	0.070	1.4	0.00095
	50	280.9	0.054	1.8	0.00035
	70	403.5	0.051	2.0	0.00025
	100	595.3	0.047	2.1	0.00017
	120	726.6	0.043	2.3	0.00014
	150	889.1	0.041	2.4	0.00011
	170	1031.3	0.039	2.6	0.00010
	200	1213.8	0.039	2.6	0.00008
<b>16-X-8</b>	--	50.0	0.076	1.3	0.00199
	20	104.0	0.099	1.0	0.00096
	50	249.9	0.085	1.2	0.00040
	70	369.2	0.073	1.4	0.00027
	100	545.8	0.080	1.2	0.00018
<b>16-X-9</b>	--	50.0	0.042	2.4	0.00199
	20	117.1	0.103	1.0	0.00085
	50	266.2	0.076	1.3	0.00037
	70	374.1	0.070	1.4	0.00027
	100	537.1	0.072	1.4	0.00019
	<b>Analog Voltage [V]</b>	<b>Max Current [A]</b>	<b>Resistance [Ohms]</b>	<b>Current Error [A]</b>	<b>Resistance Error [Ohms]</b>
<b>32-X-7</b>	--	50	0.045	2.2	0.00199
	20	108.2	0.047	2.1	0.00092
	50	305.8	0.034	2.9	0.00033
	100	647.3	0.024	4.1	0.00015
	182	1194.3	0.029	3.4	0.00008
<b>32-X-8</b>	--	50	0.050	2.0	0.00199
	50	309.0	0.033	3.0	0.00032
	100	642.9	0.027	3.7	0.00015
	154	999.1	0.026	3.8	0.00010
	168	1091.0	0.027	3.7	0.00009
<b>32-X-9</b>	--	50.0	0.042	2.4	0.00199
	50	297.4	0.032	3.1	0.00033
	100	641.7	0.028	3.6	0.00016
	152	980	0.024	4.1	0.00010
	167	1084.6	0.026	3.8	0.00009
	183	1212.3	0.023	4.3	0.00008
	199	1303.8	0.022	4.5	0.00008
	214	1412.1	0.022	4.5	0.00007
	229	1495.3	0.021	4.7	0.00007

Table A. 1. Continued

	244	1592.6	0.023	4.3	0.00006
	<b>Analog Voltage [V]</b>	<b>Max Current [A]</b>	<b>Resistance [Ohms]</b>	<b>Current Error [A]</b>	<b>Resistance Error [Ohms]</b>
<b>16-U-0BP-7</b>	--	50	0.052	1.9	0.00199
	50	296.7	0.043	2.3	0.00034
	80	508.4	0.036	2.8	0.00020
	100	609	0.027	3.7	0.00016
	120	747	0.026	3.8	0.00013
	140	868.6	0.026	3.8	0.00011
<b>16-U-0BP-8</b>	--	50	0.045	2.2	0.00199
	50	310.4	0.031	3.2	0.00032
	80	502.8	0.028	3.5	0.00020
	100	630.9	0.023	4.4	0.00016
	120	764.6	0.021	4.7	0.00013
<b>16-U-0BP-9</b>	--	50	0.049	2.0	0.00199
	50	307.5	0.035	2.8	0.00032
	80	429.7	0.029	3.4	0.00023
	100	606.1	0.030	3.4	0.00016
	120	743.2	0.025	3.9	0.00013
	140	876.6	0.023	4.3	0.00011
	<b>Analog Voltage [V]</b>	<b>Max Current [A]</b>	<b>Resistance [Ohms]</b>	<b>Current Error [A]</b>	<b>Resistance Error [Ohms]</b>
<b>16-U-4BP-7</b>	--	50	0.033	3.0	0.00199
	50	287.1	0.038	2.6	0.00035
	80	495.7	0.031	3.2	0.00020
	100	642.7	0.025	4.0	0.00015
	120	764.7	0.022	4.5	0.00013
	140	888.8	0.020	5.0	0.00011
	160	1037.9	0.019	5.2	0.00010
<b>16-U-4BP-8</b>	--	50.0	0.034	2.9	0.00199
	50	259.6	0.048	2.1	0.00038
	80	483.5	0.032	3.1	0.00021
	100	635.0	0.023	4.3	0.00016
	120	771.8	0.023	4.3	0.00013
	140	905.3	0.020	4.9	0.00011
	160	1034.9	0.019	5.4	0.00010
<b>16-U-4BP-9</b>	--	50.0	0.034	2.9	0.00199
	50	322.6	0.028	3.6	0.00031
	80	524.1	0.023	4.3	0.00019
	100	639.3	0.020	5.1	0.00016
	120	785.0	0.019	5.2	0.00013
	140	917.2	0.018	5.6	0.00011



Table A. 1. Continued

	160	1051.5	0.018	5.4	0.00009
	180	1162.4	0.015	6.7	0.00009
	<b>Analog Voltage [V]</b>	<b>Max Current [A]</b>	<b>Resistance [Ohms]</b>	<b>Current Error [A]</b>	<b>Resistance Error [Ohms]</b>
<b>16-U-7BP-7</b>	--	50	0.038	2.6	0.00199
	50	237.2	0.041	2.4	0.00042
	80	411.1	0.031	3.2	0.00024
	100	513.8	0.028	3.6	0.00019
	120	621.7	0.026	3.8	0.00016
	140	723.4	0.022	4.5	0.00014
	160	845.9	0.021	4.7	0.00012
<b>16-U-7BP-8</b>	--	50	0.033	3.0	0.00199
	50	286.9	0.038	2.6	0.00035
	80	521.9	0.027	3.7	0.00019
	100	641.8	0.020	4.9	0.00016
	120	784.4	0.019	5.2	0.00013
	140	901.5	0.019	5.3	0.00011
	160	1029.6	0.017	5.7	0.00010
<b>16-U-7BP-9</b>	--	50.0	0.021	4.7	0.00199
	50	309.5	0.026	3.8	0.00032
	80	496.5	0.024	4.1	0.00020
	100	642.1	0.021	4.8	0.00015
	120	774.0	0.020	5.1	0.00013
	140	907.3	0.018	5.5	0.00011
	160	1034.5	0.018	5.6	0.00010

APPENDIX B: DELAMINATION PLOTS

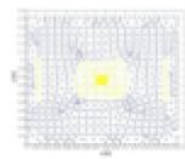
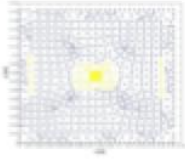
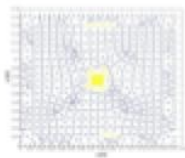
Int #	Lower Ply [°]	Interface	Int #	Lower Ply [°]	
1	90		8	0	
2	0		9	90	
3	90		10	0	
4	0		11	90	
5	90		12	0	
6	0		13	90	
7	90		14	0	

Figure B. 1. Plot of simulation-based delamination predictions for  $[0/90]_{4S}$  specimen 16-X for all 14 interfaces between plies with different fiber orientations. (Peak Impact Load = 9831 N, Striker type = 12.7mm flat). Interfaces numbered 1-14 from closest to impacted surface down. Yellow areas are predicted delamination.

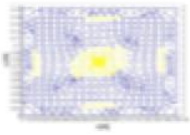
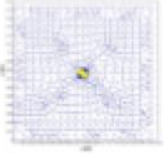
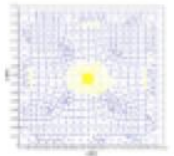
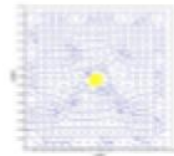
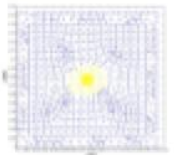
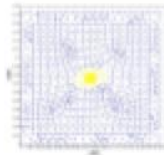
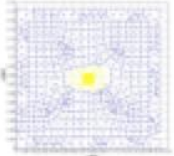
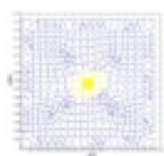
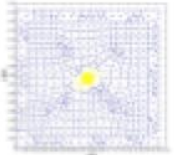
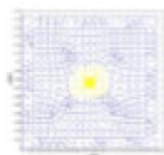
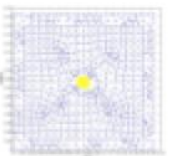
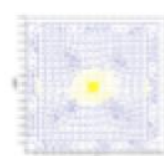
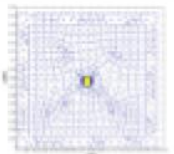
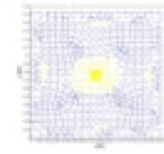
Int #	Lower Ply [°]	Interface	Int #	Lower Ply [°]	
1	45		8	-45	
2	-45		9	45	
3	90		10	0	
4	0		11	90	
5	45		12	-45	
6	-45		13	45	
7	90		14	0	

Figure B. 2. Plot of simulation-based delamination predictions for  $[0/45/-45/90]_{2S}$  specimen 16-Q-Int for all 14 interfaces between plies with different fiber orientations. (Peak Impact Load = 3320 N, Striker type = 12.7mm round). Interfaces numbered 1-14 from closest to impacted surface down. Yellow areas are predicted delamination.

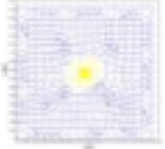
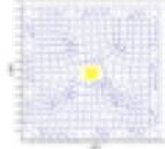
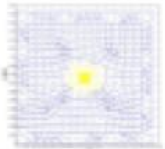
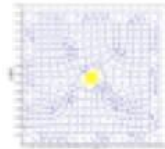
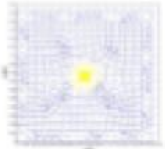
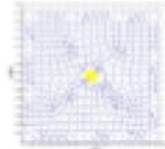

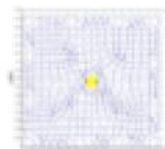

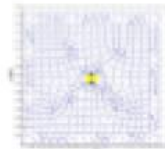
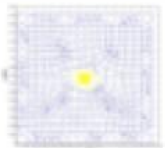
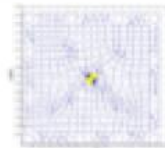
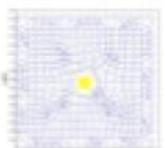
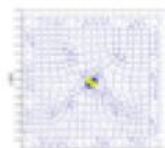
Int #	Lower Ply [°]	Interface	Int #	Lower Ply [°]	
1	45		8	0	
2	-45		9	45	
3	90		10	-45	
4	0		11	90	
5	45		12	0	
6	-45		13	45	
7	90		14	-45	

Figure B. 3. Plot of simulation-based delamination predictions for  $[0/45/-45/90]_{4S}$  specimen 32-Q-Int for all interfaces between plies with different fiber orientations. (Peak Impact Load = 9020 N, Striker type = 12.7mm round). Interfaces numbered 1-30 from closest to impacted surface down. Yellow areas are predicted delamination.

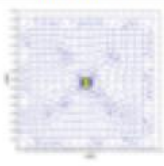
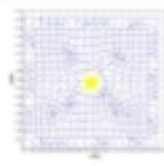
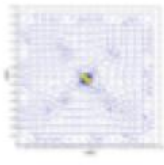
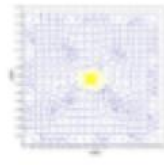
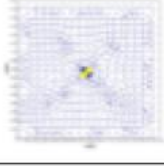
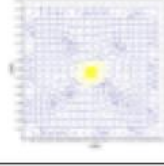
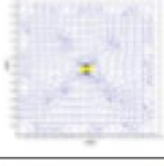
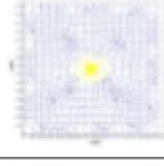
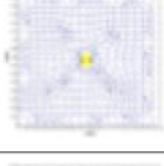
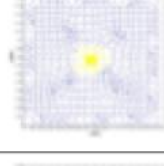
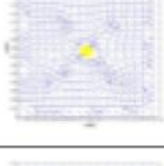
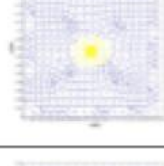
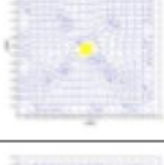
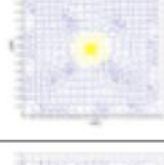

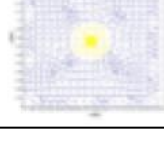
Int #	Lower Ply [°]	Interface	Int #	Lower Ply [°]	
15	90		23	90	
16	-45		24	-45	
17	45		25	45	
18	0		26	0	
19	90		27	90	
20	-45		28	-45	
21	45		29	45	
22	0		30	0	

Figure B. 3. (Continued)

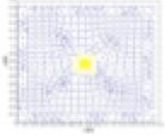
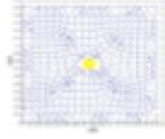
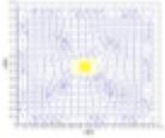
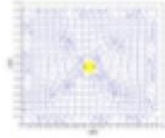
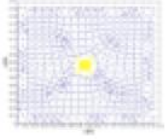
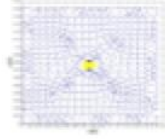
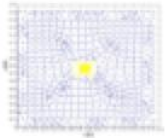
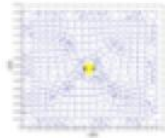
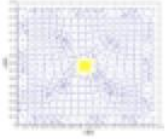
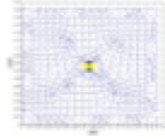
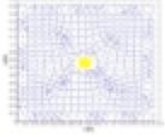
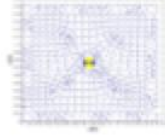
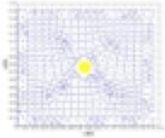
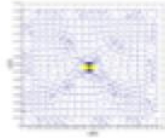
Int #	Lower Ply [°]	Interface	Int #	Lower Ply [°]	
1	90		8	0	
2	0		9	90	
3	90		10	0	
4	0		11	90	
5	90		12	0	
6	0		13	90	
7	90		14	0	

Figure B. 4. Plot of simulation-based delamination predictions for  $[0/90]_{8S}$  specimen 32-X-Low for all interfaces between plies with different fiber orientations. (Peak Impact Load = 7786 N, Striker type = 12.7mm round). Interfaces numbered 1-30 from closest to impacted surface down. Yellow areas are predicted delamination.

Int #	Lower Ply [°]	Interface	Int #	Lower Ply [°]	
15	90		23	90	
16	0		24	0	
17	90		25	90	
18	0		26	0	
19	90		27	90	
20	0		28	0	
21	90		29	90	
22	0		30	0	

Figure B. 4. (Continued)

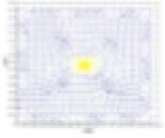
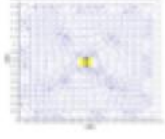

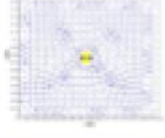
Int #	Lower Ply [°]	Interface	Int #	Lower Ply [°]	
1	90		8	0	
2	0		9	90	
3	90		10	0	
4	0		11	90	
5	90		12	0	
6	0		13	90	
7	90		14	0	

Figure B. 5. Plot of simulation-based delamination predictions for  $[0/90]_{8S}$  specimen 32-X-Int for all interfaces between plies with different fiber orientations. (Peak Impact Load = 9253 N, Striker type = 12.7mm round). Interfaces numbered 1-30 from closest to impacted surface down. Yellow areas are predicted delamination.



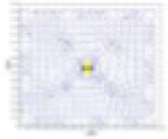
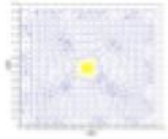
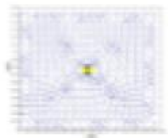
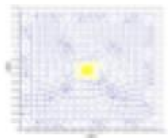
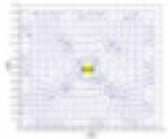
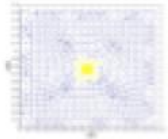
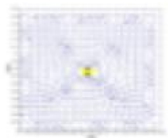
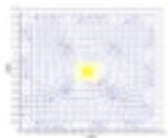
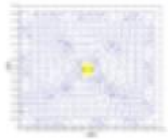
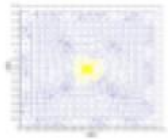
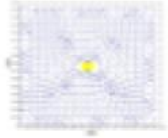
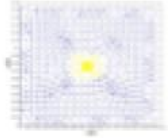
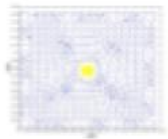
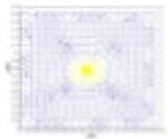

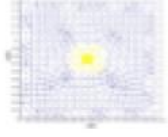
Int #	Lower Ply [°]	Interface	Int #	Lower Ply [°]	
15	90		23	90	
16	0		24	0	
17	90		25	90	
18	0		26	0	
19	90		27	90	
20	0		28	0	
21	90		29	90	
22	0		30	0	

Figure B. 5. (Continued)

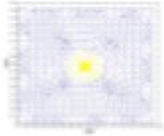
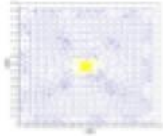
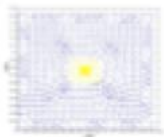
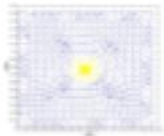
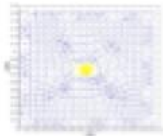
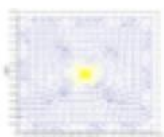
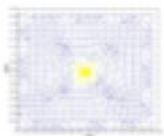
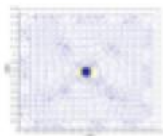
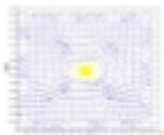
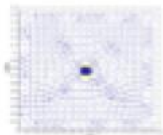
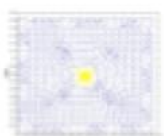
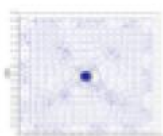
Int #	Lower Ply [°]	Interface	Int #	Lower Ply [°]	
1	90		8	0	
2	0		9	90	
3	90		10	0	
4	0		11	90	
5	90		12	0	
6	0		13	90	
7	90		14	0	

Figure B. 6. Plot of simulation-based delamination predictions for  $[0/90]_{8S}$  specimen 32-X-High for all interfaces between plies with different fiber orientations. (Peak Impact Load = 11748 N, Striker type = 12.7mm flat). Interfaces numbered 1-30 from closest to impacted surface down. Yellow areas are predicted delamination.

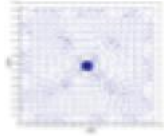
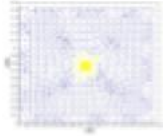
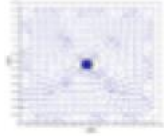
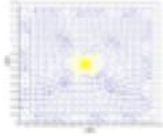
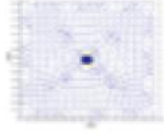
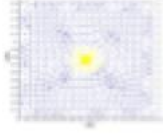
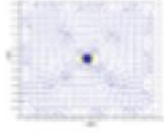
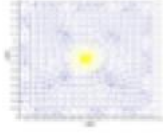
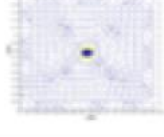
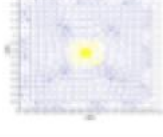
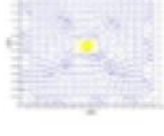
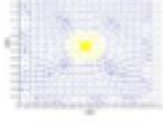
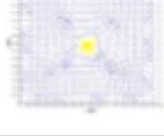
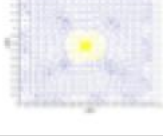
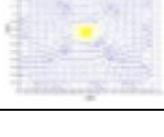
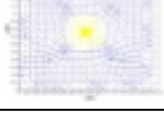
Int #	Lower Ply [°]	Interface	Int #	Lower Ply [°]	
15	90		23	90	
16	0		24	0	
17	90		25	90	
18	0		26	0	
19	90		27	90	
20	0		28	0	
21	90		29	90	
22	0		30	0	

Figure B. 6. (Continued)

## REFERENCES

- [1] Kramer S, Mosher D. Here's how much money it actually costs to launch stuff into space. *Bus Insid* 2016.
- [2] Raihan R. Dielectric Properties of Composite Materials during Damage Accumulation and Fracture. Univeristy of South Carolina, 2014.
- [3] de Moura MFSF De, Marques AT. Prediction of low velocity impact damage in carbon - epoxy laminates. *Compos Part A* 2002;33:361–8.
- [4] Bernard ML, Lagace PA. Impact Resistance of Composite Sandwich Plates. *J Reinf Plast Compos* 1989;8:432–45.
- [5] Li Y, Zhang W, Yang Z, Zhang J, Tao S. Low-velocity impact damage characterization of carbon fiber reinforced polymer ( CFRP ) using infrared thermography. *Infrared Phys Technol* 2016;76:91–102. doi:10.1016/j.infrared.2016.01.019.
- [6] Caminero MA, Rodríguez GP, Muñoz V. Effect of stacking sequence on Charpy impact and flexural damage behavior of composite laminates. *Compos Struct* 2016;136:345–57. doi:10.1016/j.compstruct.2015.10.019.
- [7] Morioka K, Tomita Y. Effect of lay-up sequences on mechanical properties and fracture behavior of CFRP laminate composites. *Mater Charact* 2000;45:125–36.
- [8] Caminero MA, Lopez-pedrosa M, Pinna C, Soutis C. Damage monitoring and analysis of composite laminates with an open hole and adhesively bonded repairs using digital image correlation. *Compos Part B* 2013;53:76–91. doi:10.1016/j.compositesb.2013.04.050.
- [9] Sultan MTH, Worden K, Pierce SG, Hickey D, Staszewski WJ, Dulieu-barton JM, et al. On impact damage detection and quantification for CFRP laminates using structural response data only. *Mech Syst Signal Process* 2011;25:3135–52. doi:10.1016/j.ymsp.2011.05.014.
- [10] Liu PF, Liao BB, Jia LY, Peng XQ. Finite element analysis of dynamic progressive failure of carbon fiber composite laminates under low velocity impact. *Compos Struct* 2016;149:408–22. doi:10.1016/j.compstruct.2016.04.012.
- [11] Farooq U, Myler P. Thin-Walled Structures Finite element simulation of damage and failure predictions of relatively thick carbon fi bre-reinforced laminated composite panels subjected to fl at and round noses low velocity drop-weight impact. *Thin Walled Struct* 2016;104:82–105. doi:10.1016/j.tws.2016.03.011.
- [12] Park JB, Hwang TK, Kim HG, Doh YD. Experimental and numerical study of the electrical anisotropy in unidirectional carbon-fiber-reinforced polymer composites. *Smart Mater Struct* 2007;16:57–66.
- [13] Shen L, Li J, Liaw BM, Delale F, Chung JH. Modeling and analysis of the electrical resistance measurement of carbon fiber polymer – matrix composites. *Compos Sci Technol* 2007;67:2513–20.
- [14] Barakati A, Zhupanska OI. Mechanical response of electrically conductive laminated composite plates in the presence of an electromagnetic field. *Compos Struct* 2014;113:298–307.
- [15] Angelidis N, Khemiri N, Irving P. Experimental and finite element study of the electrical potential technique for damage detection in CFRP laminates. *Smart Mater Struct* 2005;14:147–54.

- [16] Busch R, Ries G, Werthner H, Kreiselmeyer G, Saemann-Ischenko G. New Aspects of the Mixed State from Six-Terminal Measurements on Bi<sub>2</sub>Sr<sub>2</sub>CaCu<sub>2</sub>O<sub>x</sub> Single Crystals. *Phys Rev Lett* 1992;69:522–5.
- [17] McAndrew J, Zhupanska OI. Experimental Assessment of Single and Cumulative Impact Damage in Carbon Fiber Polymer Matrix Composites Using Electrical Resistance Measurements. *J Multifunct Compos* 2014;2:79–91.
- [18] McAndrew J. Impact damage assessment in CFRP composites using 1D electrical resistance technique 2010:52242.
- [19] Wang D, Wang S, Chung DDL, Chung JH. Sensitivity of the two-dimensional electric potential / resistance method for damage monitoring in carbon fiber polymer-matrix composite. *J Mater Sci* 2006:4839–46.
- [20] Todoroki A, Tanaka Y, Shimamura Y. Multi-probe electric potential change method for delamination monitoring of graphite / epoxy composite plates using normalized response surfaces. *Compos Sci Technol* 2004;64:749–58.
- [21] Wang D, Chung DDL. Comparative evaluation of the electrical configurations for the two-dimensional electric potential method of damage monitoring in carbon fiber polymer – matrix composite. *Smart Mater Struct* 2006;15:1332–44.
- [22] Chung DDL. Damage detection using self-sensing concepts. *Proc IMechE* 2007;221:509–20.
- [23] Wang S, Chung DDL, Chung JH. Impact damage of carbon fiber polymer – matrix composites , studied by electrical resistance measurement. *Compos Part A* 2005;36:1707–15.
- [24] Wang S, Chung DDL. Self-sensing of damage in carbon fiber polymer-matrix composite by measurement of the electrical resistance or potential away from the damaged region. *J Mater Sci* 2005;40:6463–72.
- [25] Ceysson O, Salvia M, Vincent L. Damage Mechanisms Characterisation of Carbon Fibre / Epoxy Composite Laminates by both Electrical Resistance Measurements and Acoustic Emission Analysis. *Scr Mater* 1996;34:1273–80.
- [26] Pyrzanowski P, Olzak M. Numerical modelling of resistance changes in symmetric CFRP composite under the influence of structure damage. *Compos Sci Technol* 2013;88:99–105. doi:10.1016/j.compscitech.2013.08.023.
- [27] Gallo GJ, Thostenson ET. Electrical characterization and modeling of carbon nanotube and carbon fiber self-sensing composites for enhanced sensing of microcracks. *Mater Today Commun* 2015;3:17–26.
- [28] Gallo GJ, Thostenson ET. Spatial damage detection in electrically anisotropic fiber-reinforced composites using carbon nanotube networks. *Compos Struct* 2016;141:14–23.
- [29] Li C, Chou T. Modeling of damage sensing in fiber composites using carbon nanotube networks. *Compos Sci Technol* 2008;68:3373–9. doi:10.1016/j.compscitech.2008.09.025.
- [30] Na W, Byun J, Lee M, Yu W. In-situ damage sensing of woven composites using carbon nanotube conductive networks. *Compos Part A* 2015;77:229–36.

- [31] Wichmann B, Wichmann MHG, Malte HG, Sumfleth J, Gojny FH. Glass-fibre-reinforced composites with enhanced mechanical and electrical properties - Benefits and limitations of a nanoparticle modified matrix. *Eng Fract Mech 4th Conf Fract Polym Compos Adhes* 2013;73:2346–59. doi:10.1016/j.engfracmech.2006.05.015.
- [32] Capezzuto F, Ciampa F, Carotenuto G, Meo M, Milella E, Nicolais F. A smart multifunctional polymer nanocomposites layer for the estimation of low-velocity impact damage in composite structures. *Compos Struct* 2010;92:1913–9. doi:10.1016/j.compstruct.2010.01.003.
- [33] Reifsnider KL, Chiu WKS, Brinkman KS, Du Y, Nakajo A, Rabbi F, et al. Multiphysics Design and Development of Heterogeneous Functional Materials for Renewable Energy Devices : The HeteroFoam Story 2013;160:470–81. doi:10.1149/2.012306jes.
- [34] Reifsnider KL, Cacuci DG, Baker J, Adkins JM, Rabbi F. Validated predictive computational methods for surface charge in heterogeneous functional materials : HeteroFoam™. ??? 2015:1–9. doi:10.1186/s40759-014-0001-y.
- [35] Raihan R, Adkins J, Baker J, Rabbi F, Reifsnider K. Relationship of dielectric property change to composite material state degradation. *Compos Sci Technol* 2014;105:160–5. doi:10.1016/j.compscitech.2014.09.017.
- [36] Jagtap P, Kumar P. Evaluating shock absorption behavior of small-sized systems under programmable electric field. *Rev Sci Instrum* 2014;85:113903. doi:10.1063/1.4900842.
- [37] Miles R. Response of Materials Subjected to Magnetic Fields. 2011.
- [38] Bennett J, Gora T, Kemmey PJ, Kolkert WJ. *Electromagnetic Braking* 1985;M:1250–3.
- [39] Telitchev IY, Sierakowski RL, Zhupanska OI. Low-Velocity Impact Testing of Electrified Composites: Part I—Application of Electric Current. *Exp Tech* 2008;32:35–8.
- [40] Sierakowski RL, Telitchev IY, Zhupanska OI. On the impact response of electrified carbon fiber polymer matrix composites: Effects of electric current intensity and duration. *Compos Sci Technol* 2008;68:639–49. doi:10.1016/j.compscitech.2007.09.019.
- [41] Zantout AE, Zhupanska OI. On the electrical resistance of carbon fiber polymer matrix composites. *Compos Part A* 2010;41:1719–27.
- [42] Telitchev IY, Sierakowski RL, Zhupanska OI. Low-Velocity Impact Testing of Electrified Composites: Part II—Experimental Setup and Preliminary Results. *Exp Tech* 2008;32:53–7. doi:10.1111/j.1747-1567.2007.00244.x.
- [43] Deierling PE, Zhupanska OI. Experimental study of high electric current effects in carbon/epoxy composites. *Compos Sci Technol* 2011;71:1659–64. doi:10.1016/j.compscitech.2011.07.017.
- [44] Barakati A. Dynamic interactions of electromagnetic and mechanical fields in electrically conductive anisotropic composites. 2012.
- [45] Hart RJ. CHARACTERIZATION OF CARBON FIBER POLYMER MATRIX COMPOSITES SUBJECTED TO SIMULTANEOUS APPLICATION OF ELECTRIC CURRENT PULSE AND LOW VELOCITY IMPACT. Univ Iowa, Thesis 2011:160. doi:10.1017/CBO9781107415324.004.

- [46] Hart RJ, Zhupanska OI. Development of the experimental procedure to examine the response of carbon fiber-reinforced polymer composites subjected to a high-intensity pulsed electric field and low-velocity impact. *Rev Sci Instrum* 2016;15109.
- [47] Braunovic M, Konchits V, Konstantinovich N. *Electrical Contacts: Fundamentals, Applications and Technology*. 2007.
- [48] Ashrafi B, Diez-Pascual AM, Johnson L, Genest M, Hind S, Martinez-Rubi Y, et al. Processing and properties of PEEK/glass fiber laminates: Effect of addition of single-walled carbon nanotubes. *Compos Part A Appl Sci Manuf* 2012;43:1267–79. doi:10.1016/j.compositesa.2012.02.022.
- [49] Chang C-Y, Phillips EM, Liang R, Tozer SW, Wang B, Zhang C, et al. Alignment and properties of carbon nanotube buckypaper/liquid crystalline polymer composites. *J Appl Polym Sci* 2012:1360–8. doi:10.1002/app.38209.
- [50] Demerath BM. LOW VELOCITY IMPACT DAMAGE ASSESSMENT IN IM7/977-3 CROSS-PLY COMPOSITES USING 3D COMPUTED TOMOGRAPHY. 2015.
- [51] Haboub A, Bale H a., Nasiatka JR, Cox BN, Marshall DB, Ritchie RO, et al. Tensile testing of materials at high temperatures above 1700 °C with in situ synchrotron X-ray micro-tomography. *Rev Sci Instrum* 2014;85:83702. doi:10.1063/1.4892437.
- [52] Song C. Low velocity impact testing and computed tomography damage evaluation of layered textile composite. 2014.
- [53] Hexcel. HexTow ® IM7 2015.
- [54] Hexcel. HexTow ® AS4. Mater Datasheet 2015:2.
- [55] CYTEC. CYCOM ® 977- 3 EPOXY Y RESIN SY S TEM CYCOM ® 977-3 Epoxy Resin System 2015.
- [56] Cytec. Cycom 977-2 Epoxy Resin System -Technical Data Sheet. Cytec - Eng Mater 2012:1–4. [http://www.cemselectorguide.com/pdf/CYCOM\\_977-2\\_031912.pdf](http://www.cemselectorguide.com/pdf/CYCOM_977-2_031912.pdf).
- [57] FAA. Ch 7: Advanced Composite Materials. *AMT Aircr. Man.*, 2016, p. 1–58.
- [58] Hill CB. Investigation of electrical and impact properties of carbon fiber reinforced polymer matrix composites with carbon nanotube buckypaper layers 2012.
- [59] Deierling PE. Electrical and thermal behavior of Im7 / 977-3 Carbon fiber polymer matrix composites subjected to time-varying and steady electric currents 2010.
- [60] Lu Y, Bowler JR, Bowler N. Edge effects in four point direct current potential drop measurement. *AIP Conf Proc* 2009;28:271–8. doi:10.1063/1.3114215.
- [61] Japanese Standards Association. Testing method for resistivity of conductive plastics with a four-point probe array. *JIS K 7194* 1994.
- [62] Bridge Technology. Four Point Probe Theory. <Http://four-Point-Probes.com/four-Point-Probe-Theory/> 2016.
- [63] Chung D. Fibrous composite interfaces studied by electrical resistance measurement. *Adv Eng Mater* 2000;2:788–96.
- [64] Hexcel. 3501-6 Epoxy Matrix. Mater Datasheet 1998:36–9.
- [65] Tsai SW, Wu EM. A General Theory of Strength for Anisotropic Materials. *J Compos Mater* 1971;5:58–80.

- [66] Hashin Z. Failure Criteria for Unidirectional FibreComposites. *J Appl Mech* 1980;47:329–34.
- [67] Becker W. Mathematical simulation of external and internal damage due to low velocity impact. *Trans Eng Sci* 1994;4:2–8.
- [68] Choi HY, Chang F-K. A Model for Predicting Damage in Graphite/Epoxy Laminated Composites Resulting from Low-Velocity Point Impact. *J Compos Mater* 1992;26:2134–69.
- [69] Johnson K. *Contact Mechanics*. 1985.
- [70] Jones RM. *Mechanics of Composite Materials*. 1998.
- [71] Sisodia SM, Garcea SC, George AR, Fullwood DT, Spearing SM, Gamstedt EK. High-resolution computed tomography in resin infused woven carbon fibre composites with voids. *Compos Sci Technol* 2016;131:12–21.
- [72] Krzywinski M. Image Color Summarizer. [Http://mkweb.bcgsc.ca/color-Summarizer/](http://mkweb.bcgsc.ca/color-Summarizer/)? 2006. [http://mkweb.bcgsc.ca/color\\_summarizer/](http://mkweb.bcgsc.ca/color_summarizer/)